[30] J. Munkres. Algorithms for the assignment and transportation problems. *Journal of the Society for Industrial and Applied Mathematics*, 5(1):32–38, 1957.

[31] K. Ohmi and H. Y. Li. Particle-tracking velocimetry with new algorithm. *Measurement Science and Technology*, 11(6):603–616, 2000.

[32] K. Okamoto, Y. A. Hassan, and W. D. Schmidl. New tracking algorithm for particle image velocimetry. *Experiments in Fluids*, 19:342–347, 1995.

[33] N. T. Ouellette, H. T. Xu, and E. Bodenschatz. A quantitative study of three-dimensional Lagrangian particle tracking algorithms. *Experiments in Fluids*, 40(2):301–313, 2006.

[34] A. K. Prasad. Stereoscopic particle image velocimetry. *Experiments in Fluids*, 29:103–116, 2000.

[35] A. Rangarajan, H. Chui, and F. L. Bookstein. The softassign Procrustes matching algorithm. *Information Processing in Medical Imaging*, 1230:29–42, 1997.

[36] F. Scarano. Iterative image deformation methods in PIV. *Measurement Science and Technology*, 13(1):R1–R19, 2002.

[37] F. Scarano, L. David, M. Bsibsi, and D. Calluaud. S-PIV comparative assessment: image dewarping plus misalignment correction and pinhole plus geometric back projection. *Experiments in Fluids*, 39(2):257–266, 2005.

[38] L. G. Shapiro and G. C. Stockman. *Computer Vision*. Prentice Hall, 2001.

[39] A. Stitou and M. L. Riethmuller. Extension of PIV to super resolution using PTV. *Measurement Science and Technology*, 12(9):1398–1403, 2001.

[40] M. Svedlow, C. D. McGillem, and P. E. Anuta. Experimental examination of similarity measures and preprocessing methods used for image registration. In *Symposium on Machine Processing of Remotely Sensed Data*, pages 9–17, 1976.

[41] K. Takehara, R. J. Adrian, G. T. Etoh, and K. T. Christensen. A Kalman tracker for super-resolution PIV. *Experiments in Fluids*, 29:S34–S41, 2000.

[42] J. R. Taylor. *An Introduction to Error Analysis: The Study of Uncertainties in Physical Measurements*. University Science Books, 2nd edition, 1997.

[43] P. T. Tokumaru and P. E. Dimotakis. Image correlation velocimetry. *Experiments in Fluids*, 19(1):1–15, 1995.

[44] R. Y. Tsai. A versatile camera calibration technique for high-accuracy 3D machine vision metrology using off-the-shelf TV cameras and lenses. *IEEE Journal of Robotics and Automation*, RA-3(4):323–344, 1987.

[45] G. Wahba. *Spline Models for Observational Data*. SIAM, 1990.

[46] J. Westerweel. Efficient detection of spurious vectors in particle image velocimetry data. *Experiments in Fluids*, 16:236–247, 1994.

[47] J. Westerweel and F. Scarano. Universal outlier detection for PIV data. *Experiments in Fluids*, 39(6):1096–1100, 2005.

[48] B. Wieneke. Stereo-PIV using self-calibration on particle images. *Experiments in Fluids*, 39(2):267–280, 2005.

[49] B. Wieneke. Volume self-calibration for 3D particle image velocimetry. *Experiments in Fluids*, 45(4):549–556, 2008.

[50] C. Willert. Stereoscopic digital particle image velocimetry for application in wind tunnel flows. *Measurement Science and Technology*, 8:1465–1479, 1997.

[51] C. E. Willert. Assessment of camera models for use in planar velocimetry calibration. *Experiments in Fluids*, 41(1):135–143, 2006.

[52] C. E. Willert and M. Gharib. Digital particle image velocimetry. *Experiments in Fluids*, 10:181–193, 1991.

CHAPTER IV

Mass origin and transport in thermal plumes

4.1 Introduction

The evolution of Earth's mantle and the distribution of masses within in it are still poorly constrained. Since the formation of Earth from the solar nebula some 4.5 Gyr ago [2], the principal planetary chemical reservoirs, of which the mantle is the largest, have been continually undergoing change. Some evolutionary aspects such as continental erosion, subduction of oceanic plates, or the ongoing outgassing of the mantle involve mass transfer between existing terrestrial reservoirs that together can be envisioned as forming somewhat of a closed system. However, Earth's history has undoubtedly been punctuated by extra-terrestrial exchanges where mass has been gained [25, 49] and continues to be lost [47]. The end result for mantle geodynamics is a complex geochemical picture that is superposed and dependent upon the equally intricate fluid dynamics of mantle convection.

Systematic comparisons of isotopic ratios for noble gasses and other elements (primarily Nd, Pb, and Sr) suggest that at least five distinct geochemical reservoirs are needed to explain the available observations from ocean-island basalts (OIB) and mid-ocean ridge basalts (MORB) with some of these reservoirs remaining isolated from substantial intermixing for 1-3 Gyr [80, 33, 35]. Preservation of these different compositional domains has at times been used to argue for layered mantle convection.

In this regime, the upper mantle above the 660 km phase change is allocated to production and recycling of oceanic crust, while the lower mantle evolves separately, is enriched in primitive isotopes (*e.g.*, ^{3}He), and serves as the primary source for OIB. Geophysical considerations, however, suggest such a simplistic view may be unrepresentative of actual mantle dynamics.

Seismic tomography models clearly demonstrate structures associated with downwelling oceanic slabs penetrating the 660 km phase change [70, 26, 75], although some possibly weaker slabs may be deflected [75, 23]. Similarly, low seismic velocity anomalies beneath some ocean island hotspots have been detected indicating that lower mantle plumes may indeed be the source for these hotspots [51, 50]. In both cases, seismic tomography appears to be capturing evidence for mass transport between the upper and lower mantle.

Similarly, mantle convection numerical models incorporating phase changes and representative estimates of mantle properties also support large scale mass transport between the upper and lower mantle [79, 72, 9]. Some models do suggest that weaker downwelling slabs will temporarily accumulate at the 660 km interface until sufficient negative buoyancy has accumulated [65, 66], but mass exchange is not eliminated in these models. Furthermore, such predictions seem to be in line with the seismic tomography observations mentioned earlier of presumably weak slabs deflecting at the 660 km phase change [75, 23].

If full mantle convection does indeed occur, then the notion of the entire lower mantle being an isolated, pristine reservoir becomes untenable. Instead the geochemical observations must be accommodated by some other distribution of heterogeneities that satisfies two constraints. First, the arrangement must permit certain reservoirs to evolve in isolation long enough to produce the characteristic isotopic signatures of some OIB. However, the heterogeneities must also be situated to permit sampling by the mantle flows which ultimately produce OIB.

Several alternative proposals for the location and morphology of mantle heterogeneities have recently been developed, and each is typically structured around: a reservoir for the production of MORB, a preserved pristine component, and domains derived from the recycling of oceanic and continental crust and possibly continental lithosphere. Tackley [64] provides a review of some of the more popular schemes. The unifying assumption is that some OIB are generated from plumes originating in one or more of the reservoirs. As the plume traverses the mantle, it then proceeds to interact with additional reservoirs to produce the surface isotopic signature of a particular hotspot.

Provided deep origin mantle plumes are responsible for some hotspots, important constraints on the size and location of potential mantle reservoirs can be obtained from surface geochemical observations coupled with additional details regarding plume mass transport. But if we are to fully leverage the fluid dynamics of mantle plumes as a predictive means of constraining the nature of mantle heterogeneities, it is not sufficient to simply know that a region of the mantle is part of the plume. We also must have a detailed understanding of the precise means by which various mantle domains interact with the plume and eventually become part of it. As previously noted, heterogeneities must be located sufficiently close to the plume to be sampled by it. Consequently, the efficiency by which a plume samples its surroundings limits how far away isotopic reservoirs can be positioned relative to the plume. Given that some regions within a plume will undergo stronger stretching than others, additional constraints on heterogeneity may be inferred. Namely, the various pockets of mantle material must be positioned such that the kinematics of the plume flow do not erase their distinct signatures by stretching and subsequent chemical diffusion. The spatial arrangement of surface observables, like the bilateral asymmetry found at Hawaii [1], may also provide clues regarding the location of mantle heterogeneities. A growing body of work from the Earth sciences community has been devoted to capitalizing on

these very concepts, and we will introduce relevant studies in the ensuing discussion.

In the remainder of the text, we augment our current understanding of mass transport in thermal plumes through an analysis of experimental observations of axisymmetric, laminar starting plumes in a fluid with temperature-dependent viscosity. Earth-like conditions are expected to produce plumes with complexities that far surpass those of axisymmetric laminar plumes [12, 19, 41, 42, 44, 56]. Nevertheless, these comparatively simple flows capture many of essential mechanisms by which a laminar buoyant plume operates, and there are still few published experimental datasets available for axisymmetric plumes generated with a localized heat source in fluids having temperature-dependent viscosity [11, 13, 73]. A brief overview of our experimental technique and outline of the remaining discussion are presented in Section 4.2.

4.2 Data sources and outline of discussion

In the following analysis of thermal plume mass transport, we will utilize data from both experiments and numerical models. The availability of a high-fidelity numerical model has permitted a more thorough understanding of the structures that govern plume mass transport than would have been possible via our experimental data alone. Noise is an unavoidable aspect of experimental datasets, and it is not always immediately clear when behavior inferred from experimental data represents a real characteristic of the flow or is simply a spurious manifestation of noise. Of course numerical models are certainly not immune to data quality issues, but provided the underlying computational technique is stable and the physical scenario simulated is devoid of discontinuities in flow variables [68], a numerical model can produce incredibly smooth data. By simultaneously conducting an analysis using numerically and experimentally generated data, great insight regarding which flow regions or phenomena are sensitive to experimental noise can be ascertained.

A full description of our experimental setup can be found in Chapter II. Briefly,

laminar plumes are generated in an acrylic, cubic tank having an inner dimension of 26.5 cm per side (ref. Figure 4.1). The tank containing the working fluid is sealed and surrounded by a water bath to provide a well-controlled initial temperature of $25.2 \pm 0.1\,^{\circ}\mathrm{C}$. The heat source is a 2 cm diameter heater located in the center of the tank bottom and flush with the surface. Plumes are created under two operating regimes with the heater operating at either constant power or constant temperature. In the constant power cases, the heater power is fixed, and its temperature is found to increase slowly over time as dictated by the flow dynamics. Actual power delivered to the fluid in the constant power cases, monitored with a thin-film heat flux gauge (Omega HFS-3) cemented to the heater, is always less than the total heater power because of parasitic losses to the tank structure. For the constant temperature cases, the heater power is digitally controlled and allowed to fluctuate such that the heater temperature ramps up to the desired steady state surface temperature in 90 s or less.[1] Once the constant temperature set point is reached, the heater surface temperature is maintained to $\pm 0.1\,^{\circ}\mathrm{C}$.

In all experiments, Liquidose 436 corn syrup is utilized. The syrup is seeded with two types of neutrally buoyant passive tracers – a white powdered pigment and thermochromic liquid crystals that preferentially scatter light of a particular wavelength based on the temperature of the liquid crystals. The encapsulated liquid crystals utilized, Hallcrest NSL33R25C15W100, are active in the visible spectrum for temperatures spanning $25 \lesssim T \lesssim 27\,^{\circ}\mathrm{C}$. Properties of the syrup are provided in Table 4.1, and a summary of experimental operating conditions can be found in Table 4.2.

Following heater activation, the 3D flow is imaged at discrete time intervals using the stereoscopic PIV (SPIV) system described in Chapter II. The raw SPIV images captured during each experiment are then processed to extract the time-dependent velocity field and fluid temperature on a uniform $(\Delta x, \Delta y, \Delta z) = (2.8, 2.8, 5)$ mm

[1]The heat flux gauge was also utilized in these experiments, however the high heat flux during the initial temperature ramp up caused the flux sensor to fail.

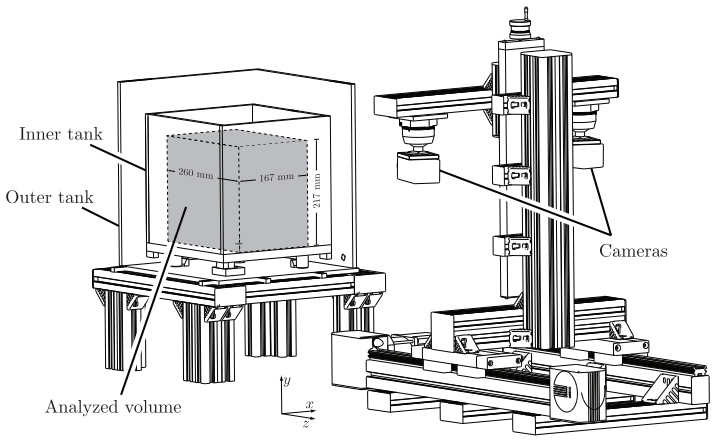

Figure 4.1: Experimental setup. The cubic inner tank (inner dimension of 26.5 mm per side) contains the corn syrup, and the outer tank provides the water bath. The heater is located in the center of the inner tank bottom. The volume of fluid analyzed via SPIV is shown in gray.

Property	Value or formulation	Units
Density at 25 °C (ρ)	1441	kg m^{-3}
Thermal expansion coefficient (α)	3.1×10^{-4}	K^{-1}
Dynamic viscosity (μ)	$\mu = 1080e^{-0.156T+6.25\times10^{-4}T^2}$	Pa s
Specific heat capacity (c_p)	2280	J kg^{-1} °C^{-1}
Thermal conductivity (k)	0.34	W m^{-1} °C^{-1}

Table 4.1: Corn syrup fluid properties. The thermal expansion coefficient and temperature dependence of viscosity were measured in the laboratory. Specific heat capacity and thermal conductivity values were provided by the manufacturer (LSI Specialty Products).

	Heater		
Case	Power [W]	Flux power [W]	Temperature [°C]
N1	0.62	0.44	-
N2	0.96	0.72	-
N3	-	-	50
N4	-	-	60
N5	-	-	70
N6	-	-	80

Table 4.2: Heater operating conditions. Flux power values represent the steady state power delivered directly to the syrup as measured with a heat flux gauge affixed to the heater. These values are lower than the total heater power due to parasitic heat losses to the acrylic tank.

grid for a $167 \times 217 \times 260$ mm section of the flow domain as illustrated in Figure 4.1. At least 48 hours are allowed between runs for the syrup to re-equilibrate with the bath temperature.

In terms of numerical models, we have utilized two: one simulating case N6 in Table 4.2 and the other simulating an injection experiment similar to that of Griffiths and Campbell [30]. Both models are constructed in the finite element code Fluidity [5][2] using adaptive mesh refinement, no slip boundaries, and simplified thermal boundary conditions to approximate the complicated tank geometry of the laboratory. In particular, the lower tank surface is modeled with an adiabatic boundary condition, and all other sides of the fluid domain are modeled as isothermal, 25.2 °C surfaces. The fluid dimensions for both simulations are the same as for the laboratory, a cube of 26.5 cm per side.

The heat source in the numerical model of case N6 is driven using a temperature versus time trace obtained from the N6 experiment and fluid properties provided in Table 4.1. As will be shown below, the model matches the experimentally observed characteristics of case N6 quite well, however it is not a perfect replication of the laboratory data. The discrepancies not associated with experimental uncertainty in

[2]The numerical computations were courtesy of Rhodri Davies, Department of Earth Science and Engineering, Imperial College London.

the velocity or temperature data are primarily a consequence of two factors. First, the slightly different thermal boundary conditions used in the model have an impact on heat transfer to and from the syrup around the heater. Furthermore, the viscosity of our syrup was found to vary by $\sim 10\%$ between batches and during experiments. This particular model will be used extensively in the ensuing discussion, and results obtained from it will often be included along side those extracted from the laboratory experiments. However, in no case do we use the numerical model data point when constructing scalings (*e.g.*, Eq. 4.28) as a function of the parameter space explored by the experiments of Table 4.2.

The second numerical model simulates the injection of 80 °C syrup through a 2 cm diameter inlet centered in the tank bottom. The hot syrup is injected at 0.3 cm^3/s into ambient syrup initially at a temperature of 25.2 °C. The syrup properties utilized are those provided in Table 4.1. Boundary conditions are the same as those discussed previously with two modifications concerning the tank top. First, the outer 1 cm of the tank top permits outflow to compensate for the volume of injected syrup. Note that except for the outflow zone, the tank top is modeled as a no-slip boundary. The second boundary condition modification allows the temperature of the tank top to vary during the course of the plume's evolution.

The remainder of the text is structured to investigate two aspects of plume mass transport. First, in Section 4.3, we employ Lagrangian coherent structures (LCS) and elements of dynamical systems theory to robustly locate and characterize the critical features that organize mass transport within the starting plume. Unfortunately, computing finite-time Lyapunov exponents to extract LCS is a computationally expensive procedure. Hence it is quite advantageous to leverage the output of the underlying methods as much as possible. To this end, we develop a simple metric in Section 4.4 based on principal stretch factors to describe the geometric dimensionality individual fluid elements will assume as a consequence of the flow. Finally, some concluding

Symbol	Description	Units
α	Thermal expansion coefficient	$^{\circ}\mathrm{C}^{-1}$
κ	Thermal diffusivity	$\mathrm{m}^2\,\mathrm{s}^{-1}$
μ	Dynamic viscosity	Pa s
ν	Kinematic viscosity	$\mathrm{m}^2\mathrm{s}^{-1}$
ρ	Density	$\mathrm{kg\,m}^{-3}$
c_p	Specific heat capacity	$\mathrm{J\,kg}^{-1}\,\mathrm{K}^{-1}$
d	Depth of fluid layer	m
$\boldsymbol{F}$	Flow map	m
g	Gravitational acceleration	$\mathrm{m\,s}^{-2}$
k	Thermal conductivity	$\mathrm{W\,m}^{-1}\,\mathrm{K}^{-1}$
$\boldsymbol{M}$	Right Cauchy-Green deformation tensor	-
Q	Heater power	W
t	Elapsed time from heater activation	s
τ	Integration time	s
T	Temperature	$^{\circ}$C
$\Delta T = T_h - T_c$	Maximum temperature contrast	$^{\circ}$C
$Pr = \nu/\kappa$	Prandtl number	-
$Ra = \alpha g Q d^2/\kappa^2 \mu_c c_p$	Rayleigh number	-

Subscripts	
c	Ambient
h	Heater

Table 4.3: Common notation.

remarks are provided in Section 4.5. Table 4.3 summarizes common notation used throughout the text.

4.3 Lagrangian coherent structures of mantle plumes

Our discussion of LCS is subdivided into several discrete units. In Section 4.3.1, we develop the mathematics that will be utilized to compute the finite-time Lyapunov exponents and provide a conceptual overview of why Lagrangian coherent structures, or the underlying material surfaces, are such powerful tools for the analysis of mass transport. We then proceed in Section 4.3.2 to extract and characterize the relevant LCS for thermal plumes of the type we have studied experimentally. Thermal plumes have been investigated by numerous authors using a variety of techniques, so we

provide an analysis of how the important plume LCS are related to several of these different flow visualization methods in Section 4.3.3. After investigating in Section 4.3.4 how LCS can be utilized to categorize flows operating in differing regimes and constrain the possible paths for mass entrainment, we finalize our LCS discussion with a detailed analysis of plume rise height and head shape (Section 4.3.5).

4.3.1 Development

Demarcating a plume from the ambient is a definitional exercise rooted in the interests of the user. The petrologist or geochemist is ultimately concerned with the ability of a plume to undergo partial melting. Consequently, these investigators may identify a plume as that portion of a mantle upwelling with sufficient potential temperature to generate a desired volume of magma. All other mantle material in this scenario might then be designated as ambient.

The problem with such schemes from a purely fluid dynamics perspective is the ambiguity associated with the definition. That is, the inferred location of the exact same plume can be made to vary from one investigator to the next simply by changing the temperature threshold used. Clearly a completely unambiguous definition of a plume would be welcome, but such notions are quite difficult to realize. Different needs simply demand different classification schemes. Nevertheless, our work with Lagrangian coherent structures (LCS) has indicated these material surfaces do provide a relatively robust means of identifying important parts of a plume. In particular, these structures form the skeleton around which the rest of the flow is built, and they provide a great deal of insight into the pathways by which the geochemical signature of various mantle reservoirs can become imprinted on the upwelling. In this section, we develop the mathematics behind the LCS and discuss methods for computing these structures plus the underlying material surfaces they represent.

For every fluid flow, individual fluid elements are advected along trajectories under

the influence of the velocity field. Given a velocity field, we can construct a system of differential equations that governs the location $\boldsymbol{x} = \boldsymbol{x}(t)$ of each fluid element

$$\dot{\boldsymbol{x}} = \boldsymbol{f}(\boldsymbol{x}, t), \tag{4.1}$$

where $\dot{\boldsymbol{x}} = d\boldsymbol{x}/dt$, and $\boldsymbol{f}(\boldsymbol{x}, t)$ represents the time varying velocity field. The path each fluid element takes under the influence of the velocity field is then a solution to Eq. 4.1, and as mandated by the uniqueness of solution theorem, trajectories in $\boldsymbol{x}, t$-space cannot intersect [34].

It turns out that many velocity fields admit special solutions and sets of solutions that convey a great deal of information about the way in which all fluid elements can move. An instructive example is the stagnation point created by two impinging jets as illustrated in Figure 4.2 and described by the linear system

$$\begin{aligned} \dot{x} &= ax \\ \dot{y} &= -ay, \end{aligned} \tag{4.2}$$

where the constant a is the strain rate. The general solution to the system is provided by

$$\boldsymbol{x}(t) = x_0 \boldsymbol{v}_1 e^{at} + y_0 \boldsymbol{v}_2 e^{-at}, \tag{4.3}$$

with the eigenvectors $\boldsymbol{v}_1 = (1, 0)$ and $\boldsymbol{v}_2 = (0, 1)$ aligning with two special material lines – the unstable and stable manifolds of the stagnation point, respectively [76]. Neglecting chemical diffusion, the unstable manifold separates fluid originating from two jets, and an instantaneously dyed volume of fluid surrounding the stagnation point would stretch out along the manifold as the flow evolves in forward time. The stable manifold, by comparison, partitions each individual jet into fluid which flows to the right or to the left. If the flow is run in backward time, then an instantaneously

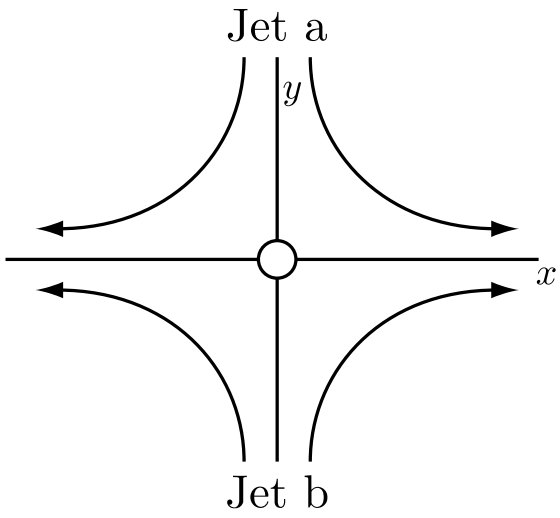

Figure 4.2: Stagnation point flow.

dyed fluid parcel will stretch out along the stable manifold. The important point in this simple example is that knowing the location of the two manifolds permits the entire flow field to be qualitatively partitioned into four quadrants with distinct behavior. Furthermore, these special material lines (*i.e.*, the manifolds) are observed to have a profound impact on the time evolution of fluid elements in their vicinity. Indeed, for the linear system of Eq. 4.2, the equation of motion (ref. Eq. 4.3) for all fluid elements anywhere in the flow field can be constructed from superposing the motion of just those elements comprising the manifolds.

For more complex velocity fields where the governing equations are non-linear, the special material lines also become more complicated. In such circumstances the manifolds become curves (or perhaps surfaces in 3D), and generally speaking the path taken by an arbitrary fluid element can no longer be represented as a linear combination of solutions along the manifolds. But our inability to construct a general closed form solution for the arbitrary fluid element's motion in no way negates the continued influence certain material lines have on the flow, which can be particularly strong for those elements in close proximity to such a structure.[3] The principal

[3]A more detailed look at the influence special material lines and surfaces can have on mass transport is provided in Appendix A.

question we now wish to consider is how the location of these material lines can be estimated. The key to the ensuing development is the recognition that fluid elements initially straddling the stable or unstable manifold in Figure 4.2 separate strongly as the flow evolves in forward or backward time, respectively.

Consider an arbitrary velocity field given by Eq. 4.1, and let $\boldsymbol{F}(\boldsymbol{x}_0, t)$ represent a function that generates valid trajectories based on initial conditions, $\boldsymbol{x}_0$. That is, $\boldsymbol{x}(t) = \boldsymbol{F}(\boldsymbol{x}_0, t)$ and $\boldsymbol{x}_0 = \boldsymbol{F}(\boldsymbol{x}_0, 0)$. The function $\boldsymbol{F}(\boldsymbol{x}_0, t)$ is known as the *flow map* or *time*-t *map* [3] and is simply the general solution of Eq. 4.1 evaluated at the arbitrary initial conditions $\boldsymbol{x}_0$. Using the flow map $\boldsymbol{F}$, a trajectory $\boldsymbol{x}_b$ that is initially close to another trajectory $\boldsymbol{x}_a$ can then be written as

$$\boldsymbol{x}_b(t) = \boldsymbol{F}(\boldsymbol{x}_b(0), t) = \boldsymbol{F}(\boldsymbol{x}_a(0), t) + \boldsymbol{\nabla}_0 \boldsymbol{F}|_{\boldsymbol{x}_a(0)} \delta \boldsymbol{x}_0 \tag{4.4}$$

where we have linearized $\boldsymbol{F}$ about $\boldsymbol{x}_a(0)$. Note that $\delta \boldsymbol{x}_0 = \boldsymbol{x}_b(0) - \boldsymbol{x}_a(0)$. Furthermore, the subscript 0 on the gradient operator is merely used to emphasize that the linearization is with respect to the dependence of $\boldsymbol{F}$ on initial conditions. Neglecting the higher order terms, setting $\delta \boldsymbol{x}(t) = \boldsymbol{x}_b(t) - \boldsymbol{x}_a(t)$, and recognizing that $\boldsymbol{x}_a(t) = \boldsymbol{F}(\boldsymbol{x}_a(0), t)$, we then have

$$\delta \boldsymbol{x}(t) = \boldsymbol{\nabla}_0 \boldsymbol{F}|_{\boldsymbol{x}_a(0)} \delta \boldsymbol{x}_0. \tag{4.5}$$

Let us now focus on how nearby trajectories move apart and not how their relative orientation varies with time. Using Eq. 4.5, we can compute the change in length of $\delta \boldsymbol{x}$ as

$$\zeta(t) = \frac{\|\delta \boldsymbol{x}(t)\|}{\|\delta \boldsymbol{x}_0\|} = \frac{\sqrt{\delta \boldsymbol{x}_0^T \left(\boldsymbol{\nabla}_0 \boldsymbol{F}\right)^T \boldsymbol{\nabla}_0 \boldsymbol{F} \delta \boldsymbol{x}_0}}{\|\delta \boldsymbol{x}_0\|} = \frac{\sqrt{\delta \boldsymbol{x}_0^T \boldsymbol{M} \delta \boldsymbol{x}_0}}{\|\delta \boldsymbol{x}_0\|} \tag{4.6}$$

where the superscript T denotes the standard transpose and

$$\boldsymbol{M} = \boldsymbol{M}(t) \equiv (\boldsymbol{\nabla}_0 \boldsymbol{F})^T \boldsymbol{\nabla}_0 \boldsymbol{F}. \tag{4.7}$$

Let $\{\lambda_i = \lambda_i(t)\}_{i\in(1,n)}$ be the n eigenvalues of $\boldsymbol{M}$ arranged in order of decreasing magnitude, and $\{\boldsymbol{v}_i = \boldsymbol{v}_i(t)\}_{i\in(1,n)}$ the corresponding normalized eigenvectors. Since $\boldsymbol{M}$ is a symmetric matrix, its eigenvectors are orthogonal. As a result, $\zeta(t)$ will be a maximum when $\delta\boldsymbol{x}_0$ is aligned with $\boldsymbol{v}_1$ and similarly a minimum when aligned with $\boldsymbol{v}_n$. Let $\delta\bar{\boldsymbol{x}}_0$ be an initial separation vector chosen parallel to an eigenvector $\boldsymbol{v}_i$ of $\boldsymbol{M}$, then for each eigendirection we have

$$\zeta_i(t) = \frac{\sqrt{\delta\bar{\boldsymbol{x}}_0^T \boldsymbol{M} \delta\bar{\boldsymbol{x}}_0}}{\|\delta\bar{\boldsymbol{x}}_0\|} = \frac{\sqrt{\delta\bar{\boldsymbol{x}}_0^T \lambda_i \delta\bar{\boldsymbol{x}}_0}}{\|\delta\bar{\boldsymbol{x}}_0\|} = \sqrt{\lambda_i}, \quad i = 1, \ldots, n. \tag{4.8}$$

Provided the dynamical system is Lipschitz continuous [34][4], $\zeta(t)$ can vary at most exponentially. For each eigendirection of $\boldsymbol{M}$, we therefore write

$$\zeta_i(t) = \sqrt{\lambda_i} = e^{K_i t}, \tag{4.9}$$

where the constant K_i is chosen to produce the correct observed separation at time t as though the distance between trajectories did indeed evolve exponentially. Solving for K_i then provides

$$K_i = \frac{1}{2t} \ln \lambda_i, \tag{4.10}$$

[4]On some open subset U of $\mathbb{R}^n$, the function $\boldsymbol{f}$ is Lipschitz continuous provided a constant K exists such that

$$|\boldsymbol{f}(\boldsymbol{x}_a) - \boldsymbol{f}(\boldsymbol{x}_b)| \leq K |\boldsymbol{x}_a - \boldsymbol{x}_b|$$

is valid for all $\boldsymbol{x}_a$ and $\boldsymbol{x}_b$ in U. The constant K is known as the *Lipschitz constant* and can be thought of in the 1D case as a sort of limiting slope that constrains how rapidly $\boldsymbol{f}$ can vary as a function of $\boldsymbol{x}$.

which in the long-time limit yields

$$\sigma_i = \lim_{t\to\infty} K_i = \lim_{t\to\infty} \frac{1}{2t} \ln \lambda_i, \quad i = 1, \ldots, n \tag{4.11}$$

Since the linearization of Eq. 4.5 was about $\boldsymbol{x}_a(0)$, the σ_i are known as the *Lyapunov exponents* of the trajectory $\boldsymbol{x}_a$, and they provide a measure of the rate at which other nearby trajectories are attracted to or repelled from $\boldsymbol{x}_a$ along the n orthogonal eigenvectors, $\boldsymbol{v}_i$, of $\boldsymbol{M}$.

Non-zero Lyapunov exponents as defined in Eq. 4.11 signify the exponential separation of nearby trajectories as $t \to \pm\infty$ [76]. Datasets of experimentally observed fluid flows are unfortunately not defined for an infinite amount of time. Therefore we drop the inifinite time limit in Eq. 4.11 and further restrict our attention to the largest eigenvalue of $\boldsymbol{M}$. The *finite-time Lyapunov exponent* (FTLE) σ_f is then defined to be

$$\sigma_f = \frac{1}{2\,|\tau|} \ln \lambda_{max,} \tag{4.12}$$

where τ is the finite time interval over which the rate of separation is computed [59].

Recall that our goal in this development has been to estimate the location of special material lines, such as the stable and unstable manifolds of the stagnation point flow from Eq. 4.2, which structurally organize the flow. All fluid elements governed by the linear system of Eq. 4.2 have the exact same set of Lyapunov exponents. As noted earlier, it is as though the behavior of elements constituting the manifolds has been imprinted on every fluid element in the flow. Because all fluid elements have the same set of Lyapunov exponents, no insight regarding the location of the manifolds can be obtained from the Lyapunov exponents in this case. Nevertheless, the image of Figure 4.2 still provides a convenient way of visualizing how Lyapunov exponents can be used to locate the material lines we seek in non-linear flows.

For the more general non-linear system, the strength of the material line's influence

typically falls off with increasing distance from the structure. That is, fluid elements sufficiently far away from the material line may not be appreciably impacted by it. Reflect on Figure 4.2 for a moment and assume that the illustration is of a non-linear system with similar characteristics. In any quadrant, we can conceptually imagine that nearby trajectories would move similarly and may not separate much if at all. Notice, however, that trajectories on either side of the y-axis will always separate strongly (*i.e.*, stretch) in forward time and therefore likely produce a ridge in the FTLE field. Provided the mass flux across an FTLE ridge is sufficiently small [59], the ridge is a proxy for a material line which clearly has an appreciable effect on the behavior of fluid elements in its vicinity. Ridges of elevated values in the forward-time FTLE field ($\tau > 0$) having negligible mass flux across them are then identified as forward-time Lagrangian coherent structures (LCS) [31, 59]. Similarly, material ridges in the backward-time FTLE field ($\tau < 0$) are backward-time LCS. These LCS approximately locate the special material lines we seek.

To compute the FTLE field we employ the technique of Shadden *et al.* [59] with fourth order Runge-Kutta time-stepping [22] and linear interpolation in both space and time.[5] Briefly, a grid of passive tracers is initialized at some particular time and then allowed to advect with the velocity field for a chosen time interval τ. By advecting the tracers, we have computed the flow map $\boldsymbol{F}$ in Eq. 4.6, and the FTLE can be determined from the above development. Note that as the integration time τ is increased, the length of the ridge visible in the FTLE field also typically increases [29].

When the LCS must be precisely determined and represented as a curve instead of simply a region of elevated values in the scalar FTLE field, then some means of extracting the ridge must be employed. One such technique is to release passive tracers near the ridge and allow them to climb by gradient ascent to the locally

[5]This procedure is used to compute all FTLE fields in the present text.

highest FTLE value [48]. In our experience, this particular approach can sometimes run into issues for a couple of reasons. The FTLE field often has many ridges, some of which may not correspond to material lines. But, even when a ridge does represent a material line, the ridge is not always continuous along that line [8].

An alternative approach we have found quite robust is to approximately locate various structures with LCS first, and then where possible grow an estimate of the underlying material line from the LCS [8]. In practice, the desired material surface is grown by seeding the LCS with passive tracers and then numerically advecting the tracers in forward or backward time using the velocity field. The technique leverages the attraction fluid elements have to the underlying material line an LCS approximately locates [7, 60]. In forward time, fluid is generally attracted to the material line of a backward-time LCS, and *vice versa*.

Before proceeding to analyze our experimental data, it should be noted that use of the FTLE field does not need to be limited solely to the extraction of LCS. By definition, the Lyapunov exponents provide a measure of the average rate at which nearby trajectories move apart. Consequently, areas of elevated FTLE values correspond to regions of high fluid stretching.

The utility of the FTLE field has been recognized in the geodynamics community for some time, both as a means of quantifying stretching and also constraining the mechanisms by which mass is transported [18, 20, 21, 40, 58]. The application of these concepts to the thermal plumes considered in the present text has been heavily influenced by the previous works of Farnetani *et al.* [17] and that of Lin and van Keken [45]. In what follows, we will utilize these tools to investigate the mass transport behavior of simple axisymmetric plumes and to characterize the evolution of the plume head. We will return to the broader topic of stretching in Section 4.4.

4.3.2 Thermal plume LCS

Figure 4.3 presents a comparison of velocity, temperature, and FTLE fields at $t = 1050$ s following heater activation for case N6 of Table 4.2 and the numerical model described above. Although the specific details for each plume vary as a function of the parameters given in Table 4.2, the characteristics depicted in Figure 4.3 are typical of all six experimental cases. We have included the numerical model of case N6 in the discussion to help the reader visualize the impact experimental noise and other errors have on the FTLE field and extracted LCS. In our experience, LCS are surprisingly robust to what can be large errors provided the errors are temporally or spatially limited [31].

Two discrepancies between the numerical model and our experimental case N6 are clearly apparent in Figure 4.3. First, note that the temperature contour shown for the experimental data in Figures 4.3 (a-c) does not extend all the way to the tank bottom ($y = 0$). This spurious artifact is caused by light which reflects off the tank bottom and washes out the colors generated by the temperature sensitive liquid crystals. The issue has no impact on the LCS, but clearly limits the capacity to determine temperatures within the thermal boundary layer.

Also apparent from a comparison of Figures 4.3 (a) and (d) is the absence of a high velocity zone immediately above the heater in the experimental data of Figure 4.3 (a). Manual inspection of our raw PIV images indicates that the maximum velocities shown in Figure 4.3 (d) are representative of actual particle displacements from the experiment. The lack of a high velocity zone in our N6 case is a consequence of our PIV scheme's difficulty handling the high velocity gradients and small spatial scale that characterize the region (ref. Chapters II and III). The spatial extent of the affected zone represents $< 1\%$ of the total fluid volume analyzed by our SPIV system, and the magnitude of the velocity discrepancy decreases as the width of the high velocity core increases (*i.e.*, as the velocity gradient decreases). Cases N1 to N3 have no discernible

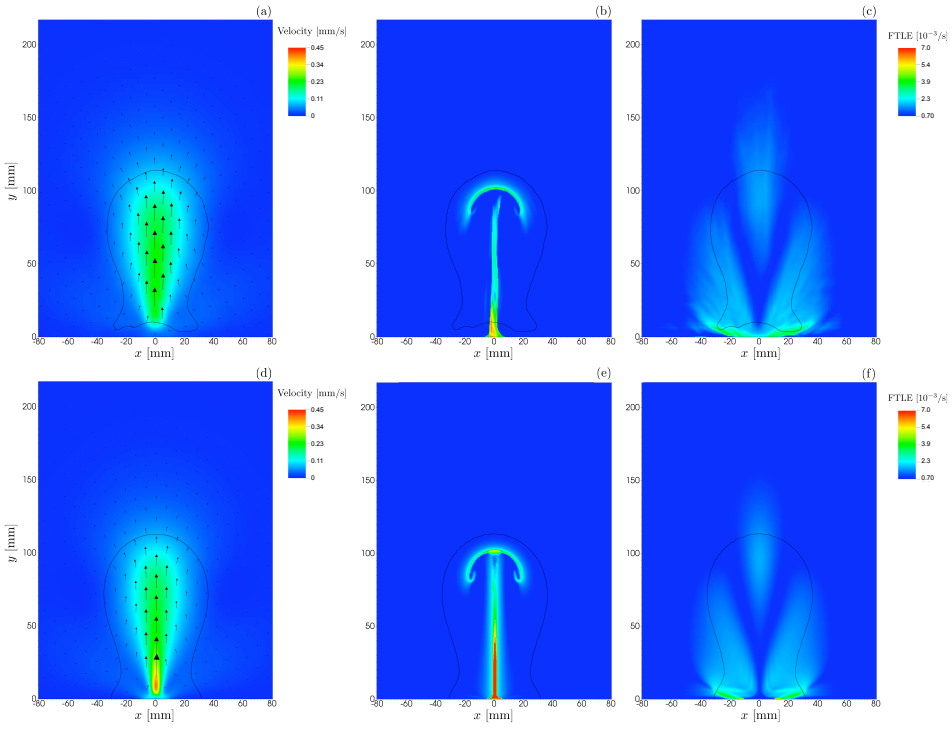

Figure 4.3: Cross-section of velocity, temperature, and FTLE fields $t = 1050$ s following heater activation for case N6 (a-c) and the corresponding numerical model (d-f). The 25.3 °C temperature contour is shown in all images as a black line for reference. The heater is centered at the origin. (a,d) Pseudo-color background is the velocity magnitude. Velocity vectors are shown as arrows. (b,e) Backward-time FTLE field with integration time $\tau = -1050$ s. (c,f) Forward-time FTLE field with integration time $\tau = 910$ s.

difference between manually measured maximum velocities and those extracted using our PIV processing scheme. The PIV-extracted maximum velocities for cases N4, N5, and N6 are 6%, 20%, and 40% lower than the corresponding velocities determined manually. The under prediction of peak conduit velocities does have a limited impact on the LCS which will be addressed later.

In discussing Lagrangian coherent structures, let us first focus on the forward-time FTLE field since its utility is rather limited for the experimental plumes under consideration. At the base of the diffuse, wing-like zone, the forward-time FTLE field of Figures 4.3(c, f) exhibits a reasonably well-defined ridge tangent to the tank bottom, however the ridge is not a material surface. Once the starting plume head has

traversed a region of the flow, the temperature and velocity distributions within the trailing conduit quickly stabilize [13]. The same is true for the fluid which wets the tank bottom. After the velocity distribution within the bottom-wetting layer stabilizes, the location of the afore mentioned FTLE ridge is a function of the integration time τ alone and moves away from the plume centerline as the integration time τ increases. As mass within this layer is radially advected toward the heater, it crosses the FTLE ridge. Therefore, the ridge is not a material surface. When a fluid element in bottom-wetting layer approaches the heater, it begins to radially elongate toward the heater. Eventually the portion of the element closest to the centerline upwells as part of the plume's conduit, but some of the element is temporarily left behind. The ridge simply marks the boundary between the portion of the element entrained into the conduit and the fraction remaining in the bottom-wetting layer. For a given element, this splitting effect cannot occur unless the element is sufficiently close to the centerline. Consequently, when the FTLE integration time τ is increased, fluid elements initially located farther away from the centerline will have ample time to advect toward it and stretch accordingly.

The diffuse region of elevated values at the apex of the temperature contour in Figures 4.3(c, f) denotes the only important material line elucidated by the forward-time FTLE field. Although this zone is not characterized by a well-defined ridge, it nonetheless marks the upper portion of the plume centerline which intersects a backward-time LCS atop the plume leading edge (discussed below). Two factors are responsible for the lack of a well-defined FTLE ridge corresponding to this material surface. First, as discussed below and in Section 4.4, fluid elements interacting with the plume head get compressed parallel to the direction of the plume's ascent and stretched into thin sheets along the head leading edge LCS. Given the 3D geometry, the volume of an incompressible fluid element compressed by a factor of $1/s$ in one dimension can be preserved by growth of $\sqrt{s}$ along both of the two perpendicular

dimensions. In other words, stretching perpendicular to the plume centerline can be substantially weaker than that parallel to the centerline. Second, the plume head has a finite diameter so the ultimate separation distance between fluid elements initially straddling the plume centerline is limited. Both of these factors serve to reduce the magnitude of the forward-time FTLE field ridge overlying the plume centerline.

In turning to the backward-time FTLE, we observe that two distinct ridges are clearly visible in Figures 4.3(b, e). The vertical structure is connected to the center of the heater where flow separation occurs and approximates the lower portion of the plume centerline. It is a continuation of the forward-time LCS discussed above, and is illuminated in the backward time FTLE field simply because tracers separate strongly as they approach the tank bottom when the flow is run in reverse. The structure is a material line and an important LCS. The FTLE values for the plume centerline are significantly higher in backward time than was observed in the forward-time FTLE field, because the width of the tank bottom is considerably larger than the plume head. That is, fluid elements initially straddling the centerline can continue to separate strongly for a much longer period of time when the flow is run in reverse. The structure's significant width and ill-defined ridge in Figures 4.3(b, e) are primarily due to insufficient spatial resolution in the velocity field near the heater, although SPIV measurement uncertainty is also a contributor (ref. Chapter II for error estimates). As a consequence of the limited spatial resolution, some passive tracers near the plume centerline advect beyond the computational domain, which corrupts the FTLE values for the affected tracers.

The second ridge visible in Figures 4.3(b, e) is the structure shaped like a mushroom cap and located in the middle of the image. The underlying material surface is actually a 3D structure as illustrated in Figure 4.4. Physically, this LCS serves as the kinematic boundary between upwelling and ambient material. In order for overlying mass to be entrained by the plume head, it must stretch around this material surface.

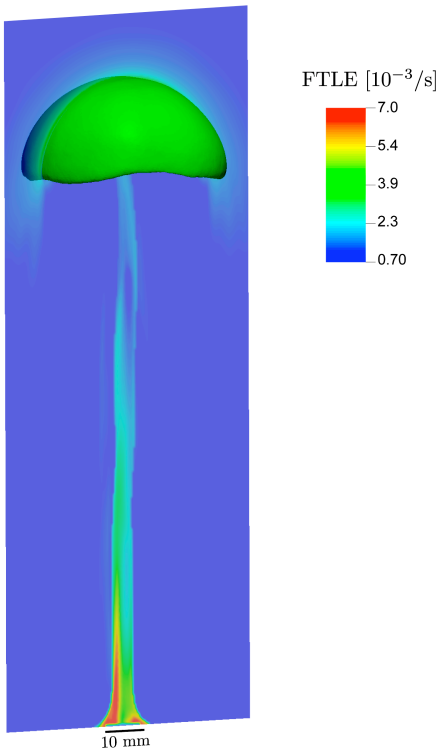

Figure 4.4: Three-dimensional backward-time LCS at the plume leading edge 1360 s following heater activation for case N6. Corresponding cross-section of the backward-time FTLE field (integration time $\tau = -1360\,\mathrm{s}$) is presented for reference.

Consequently, it represents the leading edge of the starting plume and is the most important LCS for identifying the vertical position of the plume within the flow field. This particular structure, which we will refer to as the leading edge LCS, will be the focus of much of the remaining discussion.

The leading edge LCS strongly attracts nearby fluid elements which renders it responsible for the shape elements assume as they are stretched out along the LCS during the plume's ascent. A qualitative demonstration of the manner in which fluid elements interact with the structure is provided in Figure 4.5. Note that the leading edge LCS completely dominates the evolution of the tracers shown with all but the outermost green circles getting plastered onto the LCS as the flow progresses. The overlying blue and green circles have an initial diameter of 3.3 mm, but 1170 s

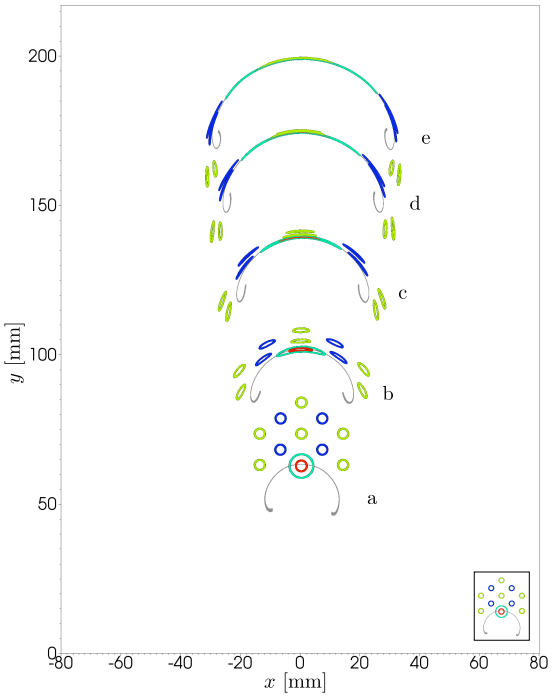

Figure 4.5: Influence of plume leading edge LCS on nearby fluid elements. Passive tracers initially configured as shown in (a) at $t = 740$ s are advected using the velocity field for case N6. The subsequent state of the tracers is presented for integration times of (b) $\tau = 310$ s, (c) $\tau = 620$ s, (d) $\tau = 930$ s, (e) $\tau = 1170$ s. Note that the initial configuration of the tracers is repeated in the inset for clarity. The leading edge LCS is depicted in gray for each snapshot.

following their release (ref. Figure 4.5(e)) the centermost green circles are compressed by a factor of ~ 40 normal to the LCS while the blue circles are compacted by a factor of ~ 10. Because the LCS is not uniformly attracting along its full length, the outer green tracers wrap around the bottom of the LCS instead of spreading out along its surface.

Whether nearby fluid elements are attracted, repelled, or predominantly sheared along the structure can be investigated by way of the instantaneous strain rate tensor [28, 67]. Let $\boldsymbol{H}(\boldsymbol{x}, t)$ represent the Hessian tensor of the FTLE field $\sigma_f(\boldsymbol{x}, t)$ for some location $\boldsymbol{x}$ and time t

$$\boldsymbol{H}(\boldsymbol{x}, t) = \boldsymbol{\nabla}^2 \sigma_f(\boldsymbol{x}, t). \tag{4.13}$$

For a particular position $\boldsymbol{x}_p$ on a ridge of the FTLE field, we take the unit normal $\hat{\boldsymbol{n}}(\boldsymbol{x}_p, t)$ to the ridge as the eigenvector of $\boldsymbol{H}(\boldsymbol{x}_p, t)$ having the most negative eigenvalue [28]. The strain rate normal to the ridge $\dot{\epsilon}_n$ is then defined as the inner product

$$\dot{\epsilon}_n(\boldsymbol{x}_p, t) = \langle \hat{\boldsymbol{n}}\left(\boldsymbol{x}_p, t\right), \boldsymbol{S}\left(\boldsymbol{x}_p, t\right) \hat{\boldsymbol{n}}\left(\boldsymbol{x}_p, t\right) \rangle, \tag{4.14}$$

where $\boldsymbol{S}(\boldsymbol{x}_p, t)$ is the instantaneous strain rate tensor evaluated at $\boldsymbol{x}_p$. The elements of $\boldsymbol{S}$ are given by

$$s_{i,j} = \frac{1}{2}\left(\frac{\partial u_i}{\partial x_j} + \frac{\partial u_j}{\partial x_i}\right). \tag{4.15}$$

The component of the strain rate tangential to the ridge $\dot{\epsilon}_t$ then becomes

$$\dot{\epsilon}_t(\boldsymbol{x}_p, t) = \left[\left\langle \hat{\boldsymbol{n}}\left(\boldsymbol{x}_p, t\right), \boldsymbol{S}^T\left(\boldsymbol{x}_p, t\right) \boldsymbol{S}\left(\boldsymbol{x}_p, t\right) \hat{\boldsymbol{n}}\left(\boldsymbol{x}_p, t\right) \right\rangle - \dot{\epsilon}_n^2\right]^{1/2}. \tag{4.16}$$

If $\dot{\epsilon}_n < 0$ for a given location $\boldsymbol{x}_p$ on an LCS, then nearby trajectories are instantaneously attracted to the ridge at $\boldsymbol{x}_p$. Similarly, trajectories close to a ridge will be instantaneously repelled if $\dot{\epsilon}_n > 0$. Fluid elements will be sheared across the ridge at $\boldsymbol{x}_p$ if $\dot{\epsilon}_n = 0$ and $\dot{\epsilon}_t \neq 0$, however in practice $\dot{\epsilon}_n$ will rarely equal zero due to numerical errors. Therefore we categorize the instantaneous behavior of trajectories near a ridge as being dominated by shear provided $\dot{\epsilon}_t > |\dot{\epsilon}_n|$.

Applying these criteria to the leading edge LCS of case N6 yields the characterization shown in Figure 4.6. In producing Figure 4.6, the positions $\boldsymbol{x}_p$ along the FTLE ridge were obtained using material lines grown from the LCS, however the ridge can also be extracted using a gradient climb technique [48, 54].

As indicated in Figure 4.6, the plume leading edge LCS is attracting over most of its length except for the trailing portion of the structure where it curls upward. This section of the LCS surrounds a nascent recirculation zone somewhat akin to a developing version of the classic scrolls observed by Griffiths and Campbell [30]. The

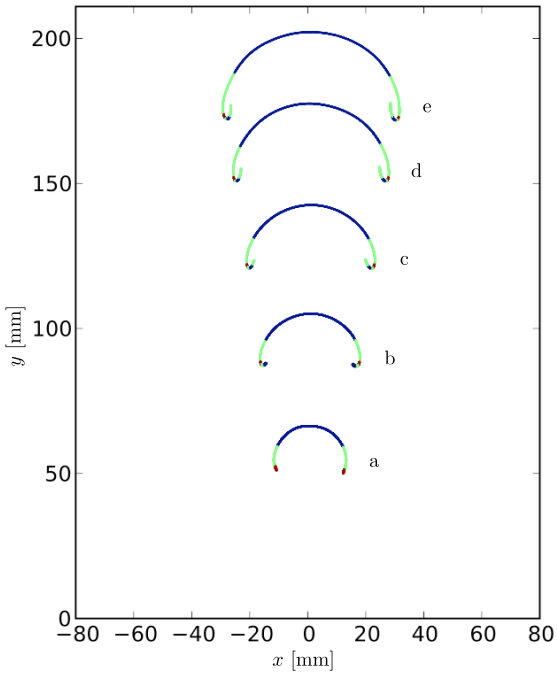

Figure 4.6: Strain rate characterization of instantaneous fluid behavior in the vicinity of the plume leading edge LCS from case N6. Fluid elements normal to the LCS are instantaneously attracted ($\dot{\epsilon}_n < 0$) at locations shown in blue and repelled ($\dot{\epsilon}_n > 0$) where red. Zones where fluid elements are predominantly sheared ($\dot{\epsilon}_t > |\dot{\epsilon}_n|$) are depicted in green. The leading edge LCS is shown at the same times as for Figure 4.5.

loss of attraction near the curls is the reason why the outermost green tracers in Figure 4.5 rotate around the bottom of the LCS instead of getting stretched out along the structure. These green tracers were launched above a section of the leading edge LCS where the attractiveness is weak and further transitioning to cycling shear-dominated, repulsive, and attractive behavior near the recirculation zone.

4.3.3 Relationship between the plume LCS and features observed with other analysis techniques

Laminar thermal plumes have been studied by numerous authors in a wide variety of fluids covering a broad range of operating regimes. Consequently, it is advantageous to have some understanding of how the LCS relate to the different analysis techniques that are frequently encountered in the literature. The following presentation will hopefully enable readers to more readily compare plume attributes extracted using LCS to those obtained by other means.

Given the thermal expansion coefficient for our syrup (ref. Table 4.1), variations in fluid temperature affect the refractive index of the fluid [10]. Optical techniques can then be constructed that are sensitive to such variation [13, 24]. One such method, the schlieren, produces an image with intensity proportional to the gradient of density (equivalently temperature) [24]. Apparent in Figure 4.7(a) is the collocation of the leading edge LCS with the maximum temperature gradient in the plume head. Note that along most of its length, the leading edge LCS is coincident with the ridge of $|\boldsymbol{\nabla} T|$. Consequently, the starting plume location determined using the leading edge LCS corresponds to a bright or dark line (depending on the knife edge orientation) of a schlieren image [24]. Furthermore, the schlieren and leading edge LCS yield equivalent measures of the plume head diameter. The plume centerline lies between the two vertical lines in a schlieren which correspond to the outer boundary of the plume conduit.

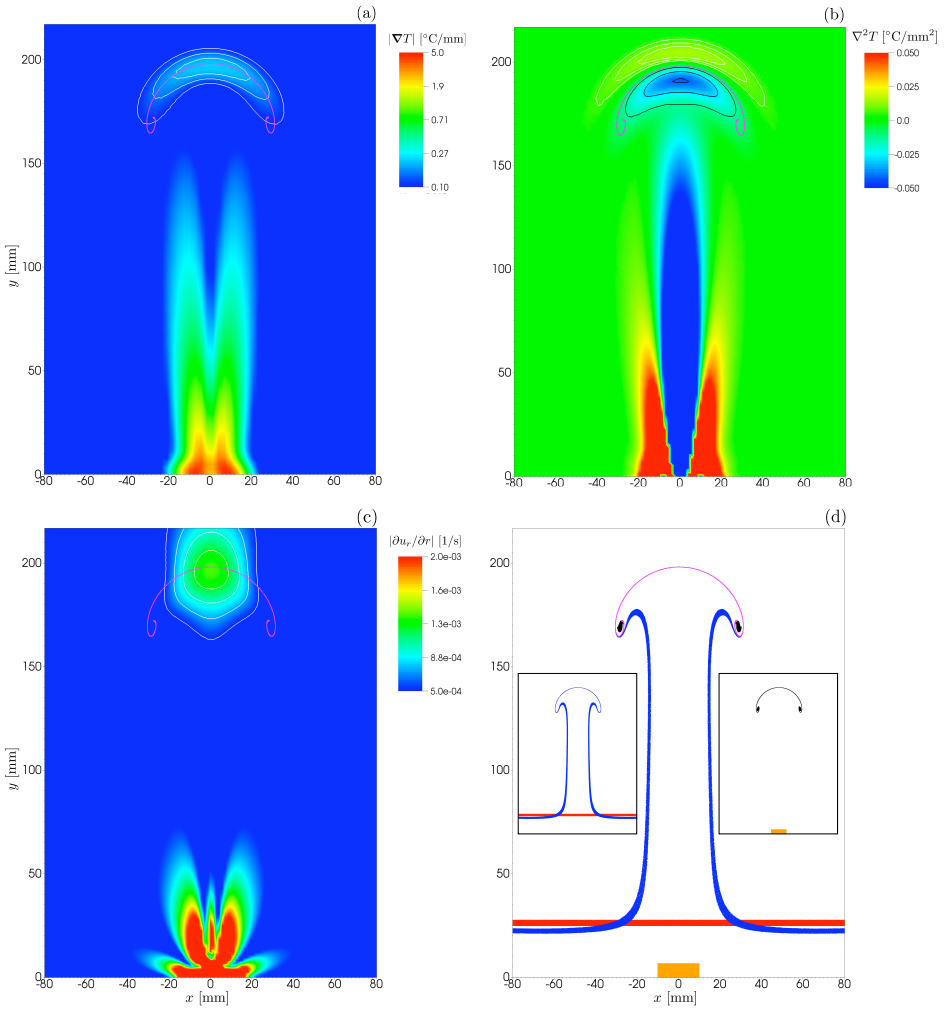

Figure 4.7: Comparison of different means of locating the leading edge of a plume. All images are generated using the numerical model (Fluidity) of case N6. The material surface grown from the leading edge LCS is shown in purple. Images (a) though (c) are presented at $t = 2000$ s following heater activation, and contours of the depicted scalar field are shown in white or black for reference. Note that the value of the scalar field for images (b) and (c) has been clipped to the ranges shown for clarity. (a) Magnitude of the temperature gradient. (b) Laplacian of temperature. (c) Magnitude $\partial u_r/\partial r$. (d) Simulated release of two dyed fluid parcels which are colored orange and red at $t = 0$ s. The orange dye is released just above but does not wet the heater surface. The final configuration of the dyed fluid at $t = 2000$ s is also shown, but using a different color. The original orange maps to black at $t = 2000$ s, while the red line similarly maps to the blue. Note that the purple material surface in the figure overlies essentially identical sections of the fluid colored black and blue at $t = 2000$ s. The two individual scenarios are repeated in the insets for clarity.

Shadowgraphs represent another common flow visualization technique sensitive to density variation [24, 53]. Bright lines in a shadowgraph map to regions in the flow where $\nabla^2\rho < 0$ (or $\nabla^2 T > 0$ in Figure 4.7(b) given our positive α), and dark lines map to zones where $\nabla^2\rho > 0$ ($\nabla^2 T < 0$). Inspection of Figure 4.7(b) indicates that the apex of the leading edge LCS resides at what would be the transition between bright and dark lines of a shadowgraph. Note that the plume head diameter can be determined using either the bright or dark shadowgraph line on opposite sides of the leading edge LCS. Consequently, unlike the schlieren technique, the plume head diameter determined from a shadowgraph will in general differ from that measured using the leading edge LCS. Nevertheless, an LCS-derived measurement of the head diameter will be most similar to one determined using the dark shadowgraph ridge. The plume centerlines extracted using LCS or shadowgraphs (dark line) are comparable.

Davaille *et al.* [13] recently introduced another method of analytically locating the apex of the plume leading edge using the maximum of $\partial u_r/\partial r$ (ref. Figure 4.7(c)), where u_r is the radial component of velocity in a cylindrical coordinate system. The coordinate system is oriented such that its longitudinal axis is parallel to the plume centerline, and the radial axis actually ends up being tangent to the leading edge LCS. The maximum of $\partial u_r/\partial r$ provides no information regarding the shape of the plume head, its diameter, or the location of the plume centerline.

And finally, the use of dyes or other passive tracers to locate the plume during an experiment is in essence a laboratory manifestation of the very methods employed above to grow the leading edge material surface from the corresponding LCS. Provided the dye is released sufficiently close to the starting plume, it will be attracted to and drawn out along the leading edge material surface in identical fashion as occurs for the numerical passive tracers used for growing. The simulated behavior of dye is illustrated in Figure 4.7(d) which was computed using the same numerical advection technique described previously. Although the figure demonstrates using dye to expose

the plume leading edge material surface, the plume centerline can also be extracted.

In some cases, using LCS to locate a starting plume can provide certain advantages not available from the above techniques. Both the schlieren and shadowgraph methods, for example, produce optical images of the integrated density (or temperature) distribution throughout the test cell. Employing either optical technique to visualize a complex flow composed of several plumes can be quite difficult [53, 78]. Computing LCS, by comparison, permits investigators to isolate any particular region of the flow field for further analysis. The metric $\partial u_r/\partial r$ is capitalizing on the behavior of fluid elements in the vicinity of the leading edge LCS. Consequently, the method is somewhat limited to axisymmetric applications wherein the underlying leading edge LCS is aligned with the coordinate system. For non-axisymmetric plumes, the character of $\partial u_r/\partial r$ being a maximum where the plume centerline intersects the leading edge LCS can only be preserved by constructing a local coordinate system based on *a priori* known LCS geometry.[6] The experimental use of dye and other types of passive tracers also has limitations. Namely, the working fluid must typically be replaced after each run, and only those plumes that originate from or interact with dyed fluid can be visualized.

The method of locating starting plumes using LCS or material surfaces grown from LCS is immune to many of the issues noted above, but the method does have its own important limitations. First and foremost, computing LCS requires access to the velocity field for numerical advection of passive tracers. While the velocity field is a natural product of computational fluid dynamics simulations, some technique must be employed to measure it in a laboratory setting. Furthermore, unlike shadowgraphs,

[6]To preserve the meaning of $\partial u_r/\partial r$, the axes of the local coordinate system must actually be tangent to the invariant material surfaces which the LCS are approximately locating. For plumes of the type under consideration, these material surfaces are known as stable and unstable manifolds in the dynamical systems literature, and they originate from the distinguished trajectory which lies at their intersection [36, 76]. The distinguished trajectory can be envisioned as a sort of moving stagnation point where the instantaneous velocity is not zero, but fluid elements comprising the manifolds asymptotically decay to the trajectory as $t \to \pm\infty$.

schlierens, or the $\partial u_r/\partial r$ metric, all of which can provide valid information from a single instantaneous snapshot, computing LCS or growing surfaces requires a time history of the flow. Noise in this time-dependent velocity field can cumulatively perturb the paths of the numerical tracers and therefore contaminate the plume position inferred from an LCS [31, 59] or a grown surface.

The need to numerically advect passive tracers through time has other implications as well. To construct the backward-time LCS, for example, the flow history must extend far enough in time to permit nearby passive tracers to separate sufficiently and thereby produce elevated FTLE values [28, 29]. Our initially quiescent fluid system undergoes a major transition when the heater is activated at $t = 0$, and no benefit is realized by advecting passive tracers backward in time beyond the point of heater activation. As a result, computing backward-time LCS for a plume as it organizes and begins to upwell immediately following heater activation is generally impossible since insufficient time has elapsed for adequate tracer separation. Of course, the very young plume would be visible in a shadowgraph or schlieren even though it cannot be reliably located using the FTLE field.

4.3.4 LCS Applications for Analysis of Plume Mass Transport

As we have seen so far, certain material surfaces located using LCS have a profound effect on how fluid parcels in their vicinity behave. They can strongly attract or repel nearby fluid elements stretching them in the process, and can also organize the flow field into separate regions having very different behavior. In a sense, then, these structures serve as a sort of framework around which the dynamics of a particular flow is built. The computation of the FTLE field and extraction of LCS as ridges provide an investigative tool to identify which material lines and surfaces may be organizing the flow and acting as barriers to transport. Two flows possessing a considerably different arrangement of LCS would rightfully be expected to exhibit

disparate behavior. In this manner, knowledge of the LCS permits a qualitative classification of a flow and illuminates certain key ways in which the flow may differ from other members of the extended family.

To provide a concrete demonstration of these concepts, we consider the LCS from our two numerical models of thermal plumes (ref. Section 4.2). The first model is of our experimental case N6, and the second simulates a Griffiths and Campbell type injection experiment [30]. In the following discussion, we will identify the numerical model of the injection-type experiment as case G6 and use R6 to refer to the numerical model of our experimental case N6. Both models simulate thermal plumes generated in corn syrup having the properties provided in Table 4.1. The maximum syrup temperature (80 °C) as well as the ambient syrup temperature (25.2 °C) are also identical for the two models. The primary differences between these two cases are the way in which buoyancy is created and the characteristic Rayleigh number achieved (ref. Table 4.3).

In the model of our experimental case N6, fluid is warmed using a heater at the base of the tank. The developing thermal boundary layer surrounding the heater grows diffusively following heater activation and eventually becomes unstable thereby producing the plume. Due to the time required for the thermal boundary layer to develop (ref. Chapter V), gradients in temperature, density, and viscosity are all continuous and somewhat broad at the time of liftoff and remain so during the plume's subsequent evolution. The steady state power delivered to the syrup in this case is 1.8 W which yields $Ra = 5.3 \times 10^5$.

In contrast, buoyancy in the second numerical model is injected directly into the fluid. As the hot, uniform temperature fluid enters the tank, gradients in flow properties surrounding the nozzle are strong. By the time these sharp gradients diffuse, the injected material has had ample time to travel a significant distance. Indeed, the rise velocity of the plume head from the injection model is roughly 10×

larger than that associated with case R6. From the rate of injection, $\dot{V} = 0.3\,\mathrm{cm}^3/\mathrm{s}$, the effective power can be computed as

$$Q = \rho \dot{V} c_p \Delta T = 54\,\mathrm{W}, \tag{4.17}$$

giving $Ra = 1.6 \times 10^7$. Hence, from a convective vigor standpoint, the G6 case is $\sim 30\times$ more energetic than the plume created via the localized heat source.

Figure 4.8 presents a comparison of several flow field variables for the two numerical models. Notice that for all three variables shown, maximal values are constrained to lie in relative close proximity of the heater for the plume of case R6. In comparison, elevated values in the flow quantities presented for the injection case G6 persist for a considerable distance up the plume centerline. The end result is that the plume head in the injection model is substantially hotter, and the vorticity within the head is $\sim 20\times$ stronger than that of case R6.

The significantly elevated values of vorticity in the plume head associated with the injection experiment leads to more efficient stirring whereby entrained mass continues to stretch as it rolls up and forms a toroidal scroll [30, 71]. The scroll within the head is clearly visible in the backward-time FTLE field presented in 4.9(c). In thermal starting plumes resembling those of case R6, however, the bulk of mass entrained into the head is transported with little or no additional stirring [17]. This characteristic is manifest in the backward-time FTLE field of Figure 4.9(a) by the presence of a small curl at the base of the LCS in lieu of a pronounced scroll.

Although the Lagrangian coherent structures of these two flows do not readily provide insight into the mechanisms by which the injection plume is able to maintain high velocities, temperatures, and vorticity in the plume head, the structures do suggest the avenues by which the different plumes interact with the ambient and entrain mass. The FTLE fields computed for both numerical models are presented in

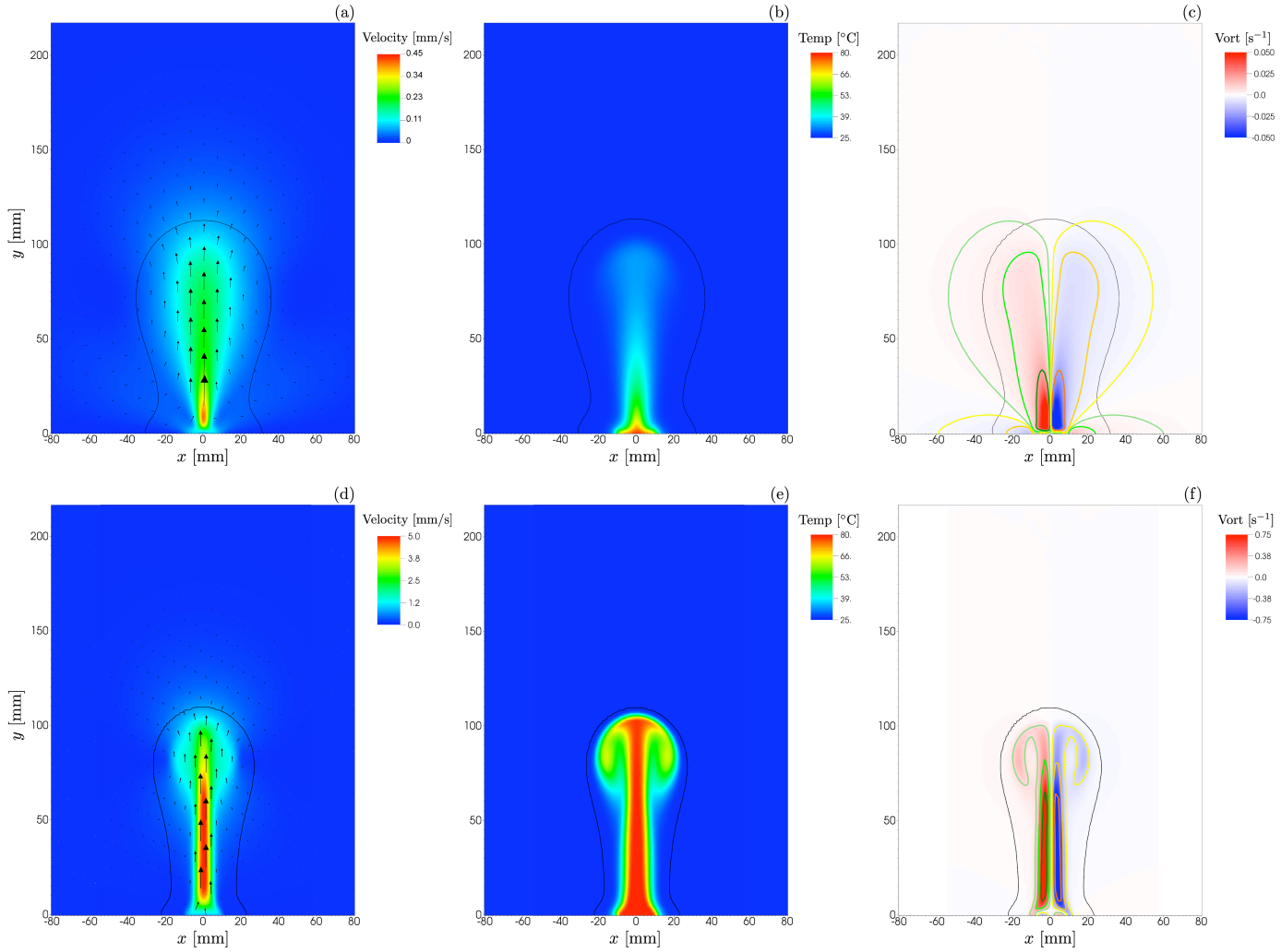

Figure 4.8: Cross-section of velocity, temperature, and vorticity fields for the two numerical models. The 25.3 °C temperature contour is shown in all figures as a solid black line. (a,b,c) Velocity, temperature, and vorticity fields for case R6 at $t = 1050$ s following heater activation. Selected vorticity contours are shown in (c) at ± 0.02, ± 0.005, and ± 0.001 s^{-1}. (d,e,f) Velocity, temperature, and vorticity fields for case G6 at $t = 130$ s following start of injection. Selected voritiy contours are shown in (f) at ± 0.75, ± 0.38, and ± 0.12 s^{-1}.

Figure 4.9. The pertinent LCS for the two cases are illustrated in Figure 4.10.

A cursory examination of Figures 4.9 and 4.10 reveals several differences in the LCS of the two cases. The backward-time FTLE field of case G6 is more complicated than that observed for the plume generated with a localized heat source. Nevertheless, the backward-time FTLE field for the injection case should look somewhat familiar in that a pronounced ridge is observed at the leading edge of the starting plume in both cases. However, the backward-time FTLE field of case G6 also shows two vertical ridges emanating from the corners of the nozzle at the base of the tank. Together these three LCS, the leading edge LCS and two segments attached to the nozzle, are pieces of a continuous material surface that surround the injected mass in an analogous fashion to the marker chain of van Keken [71].[7] Observe that no such structure enveloping source material is present in the model for a plume generated with a localized heat source (ref. Figure 4.10(a)).

The forward-time FTLE field for the two cases is also quite different. As discussed in section 4.3.2, the only LCS present in the forward-time FTLE for case R6 is the vertical segment of the plume centerline that intersects the leading edge LCS. All the other elevated FTLE values observed in Figure 4.9(b) are not LCS, as they do not correspond to material surfaces. Figure 4.9(d), however, demonstrates that the injection plume has a significant additional forward-time FTLE ridge which is not present for the R6 case. This particular ridge, shown as a dotted red line in Figure 4.10(b), also originates from the corner of the injection nozzle and sits radially just beyond the backward-time LCS which envelops the source material. What is especially interesting about this additional forward-time ridge is the manner in which it cradles the lower side of the plume head. Our testing indicates that mass flux across the ridge is small for most of its existence, and hence it approximately locates a section of an underlying material surface that is surprisingly effective at shielding

[7]The plume flows are three-dimensional. Consequently, the material surface under consideration forms a curve in the plane of cross-section.

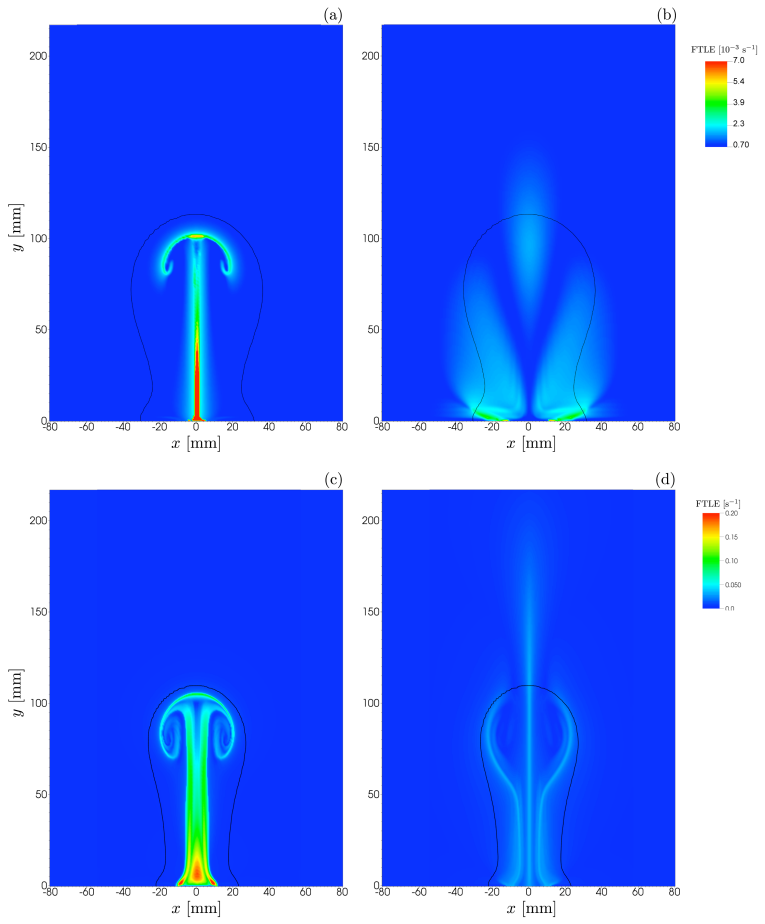

Figure 4.9: FTLE fields for the numerical models of starting plumes generated with a localized heat source (a, b) and via injection of hot syrup (c, d). (a,b) Case R6 backward and forward-time FTLE fields, respectively, at $t = 1050$ s following heater activation. (c,d). Case G6 backward and forward-time FTLE fields, respectively, at $t = 130$ s following start of injection. Integration times used to compute the FTLE fields (ref. Eq. 4.12) are (a) $\tau = -1050$ s, (b) $\tau = 910$ s, (c) $\tau = -130$ s, and (d) $\tau = 130$ s. The 25.3 °C contour is shown in all figures as a solid black line.

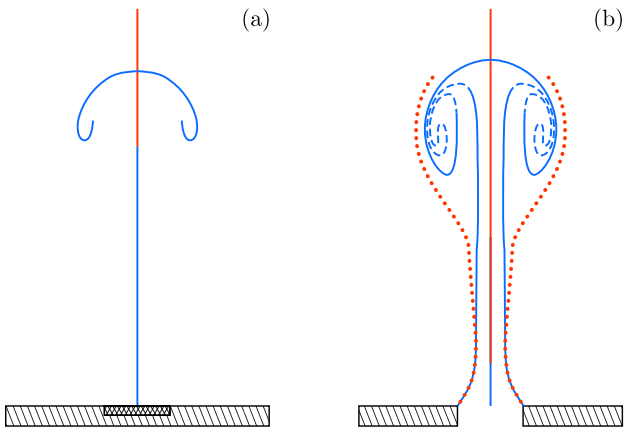

Figure 4.10: Schematic of the Lagrangian coherent structures from numerical models (a) R6 and (b) G6. The tank bottom is illustrated as a hatched volume in both figures. The heater is shown cross-hatched in (a), and the injection nozzle is depicted as a gap in the tank bottom in (b). LCS (or segments of LCS) extracted from the forward-time FTLE field are shown in red, while those extracted from the backward-time FTLE field are shown in blue. Note that the outermost forward-time LCS in (b) has been dotted for clarity. The dashed blue line in (b) connects three backward-time LCS extracted from Figure 4.9(c) to form a material line surrounding injected mass.

the plume head in case G6 from entraining mass that lies beyond its perimeter.[8] We will refer to the ridge as the outermost LCS in what follows.

The shielding effect of the outermost LCS, is illustrated in the images of Figure 4.11(a-c), which have been constructed by numerically advecting passive tracers using the velocity field. Observe that blue tracers and those non-blue tracers which lie radially beyond the outermost LCS in Figure 4.11(a) are prevented from crossing the outermost LCS (shown as a dotted black line in the figures) until the plume begins to impact the upper surface of the tank (ref. Figures 4.11(b, c)). That is, not all of the material which interacts with the plume head is entrained by the flow structure. A fraction of the fluid (and a portion of the buoyancy created by the plume head) is shed in the wake of the rising plume. Some of this mass flows between the leading edge LCS and the outermost LCS and forms a temporary reservoir that is situated below the head. The reservoir is shown seeded with green tracers surrounding the head in Figure 4.11(a). This reservoir is eventually depleted as the plume head entrains its contents. In the process of draining the reservoir, the two bounding LCS, the outermost LCS and the LCS surrounding injected mass, asymptotically become coincident along the length of the conduit. As illustrated in Figure 4.12, the fluid within the reservoir originates from overlying mass that was shed by the plume head during initial formation and shortly following liftoff.

Not all of the mass shed by the plume head ends up in the reservoir described above. The shed mass that lies radially beyond the outer LCS is prevented from entering the plume head for the duration of time in which the outer LCS acts as a barrier. Although this shed mass remains colder and less stretched than that more rapidly incorporated into the head scroll, it is nonetheless kept in close proximity to the ascending head by the plume conduit.

[8]Due to the shear-dominated nature of the LCS, precisely growing this LCS is difficult. Results from our crude techniques, not presented here, have confirmed that a material surface underlies the LCS.

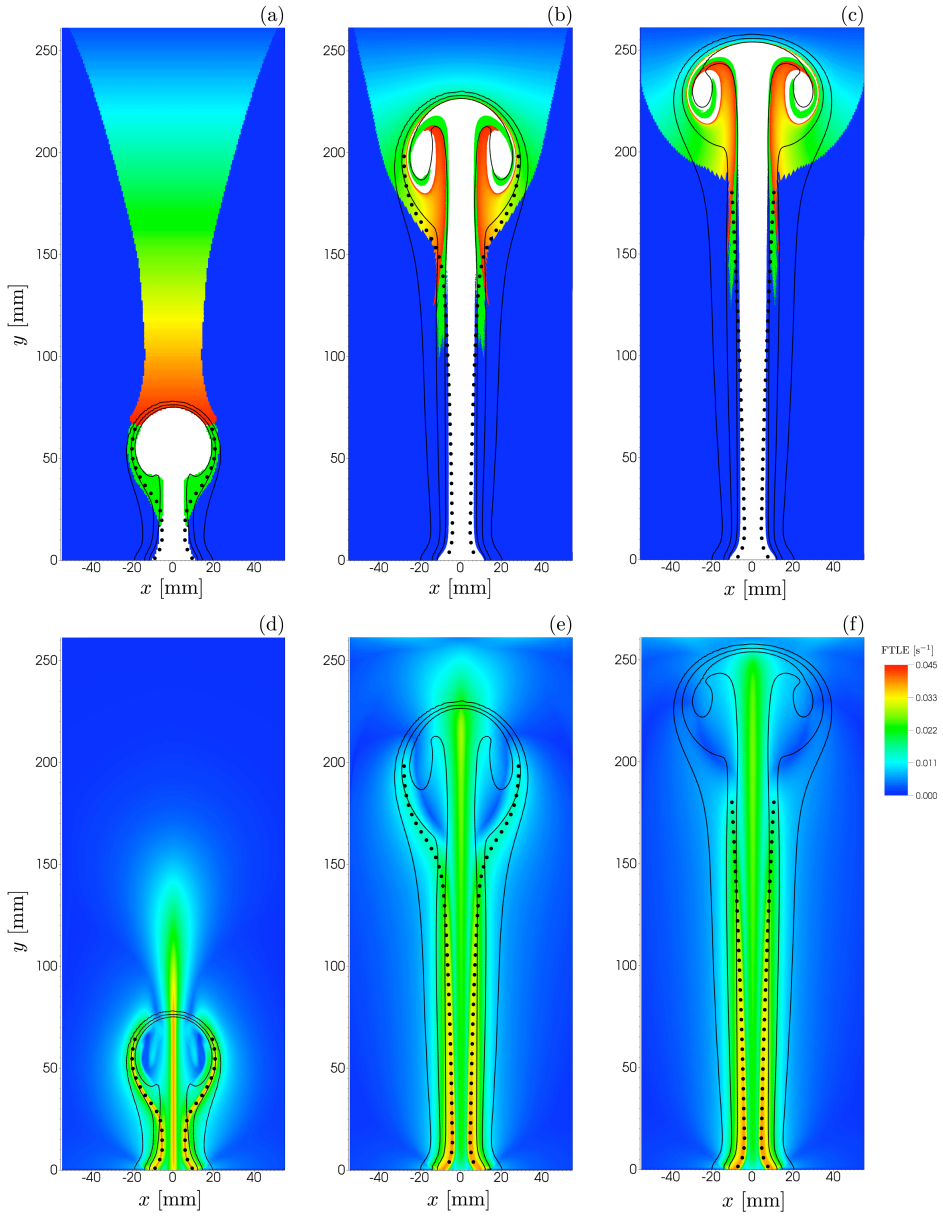

Figure 4.11: Shielding effect of the outermost LCS for the injection plume of case G6. The upper series of plots show the evolution of passive tracers launched at $t = 100$ s (a). The subsequent state of the tracers is presented at (b) $t = 250$ and (c) $t = 300$ s. The lower series of images depict the forward-time FTLE field at the same time as the figure immediately above. The solid black lines in all plots represent the 25.7, 31, and 45 °C temperature contours. The outermost LCS is illustrated in the plots as a dotted black line. Note that the FTLE fields were computed using an integration time of $\tau = 100$ s.

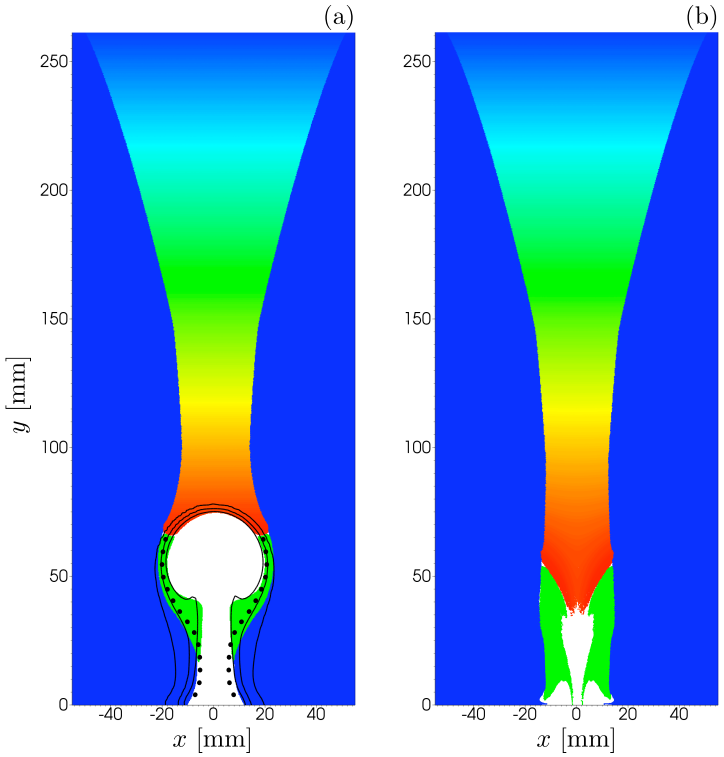

Figure 4.12: Origin of mass within the reservoir bounded between the outermost LCS and the LCS surrounding injected fluid. (a) Configuration of passive tracers from Figure 4.11(a) at $t = 100$ s, repeated for reference. (b) Tracer distribution at $t = 0$ s computed by advecting tracers in (a) backward in time. The white pockets in (b) represent mass that has already been entrained by the head at $t = 100$ s, whereas the green tracers will be temporarily shed to fill the reservoir as shown in (a).

Investigations regarding the motion of fluid elements normal to all ridges in the forward and backward-time FTLE fields for the G6 case show an alternating attraction, repulsion, shear character similar to that discussed in relation to Figure 4.6. Therefore, the structures are not uniformly hyperbolic but instead represent shear surfaces [31, 48]. As such, the structures can be expected to be somewhat fragile to perturbations [76]. After the plume traverses $\sim 85\%$ of the tank depth (ref. Figure 4.11(e)), the region of the outermost LCS which shields the lower side of the plume head from entrainment begins to weaken and disappears completely by the time the plume has risen $\sim 95\%$ of the total distance (ref. Figure 4.11(f)). Of course the material surface that once corresponded to the outermost LCS does not disappear, but the character of that surface changes with time. That is, the material surface that initially presents a strong barrier to transport weakens and does so to such a degree that a portion of the surface eventually gets entrained by the head as the plume matures.

The weakening of the outermost LCS segment beneath the head corresponds to a progressive reduction of vorticity within the portion of the head which forms the core of the scroll. The scenario is demonstrated in Figure 4.13 where the ± 0.1 s^{-1} vorticity contour which surrounds part of the head scroll in Figure 4.13(a) ceases to do so by the time of Figure 4.13(b). Over the time interval illustrated in Figure 4.13, the peak vorticity feeding the scroll has decreased by a factor of ~ 2 to 0.09 s^{-1}. Although we have not investigated the matter, the disappearance of the outermost LCS in the injection model may be sensitive to whether the upper boundary condition is a free-slip or no-slip surface.

Let us now synthesize the above concepts in an attempt to broadly characterize the overall mass transport behavior observed for cases G6 and R6. Figure 4.14 provides a series of vertical and radial contours that track the origin of mass within both plumes as they approach the upper tank surface. We define the starting plume as being

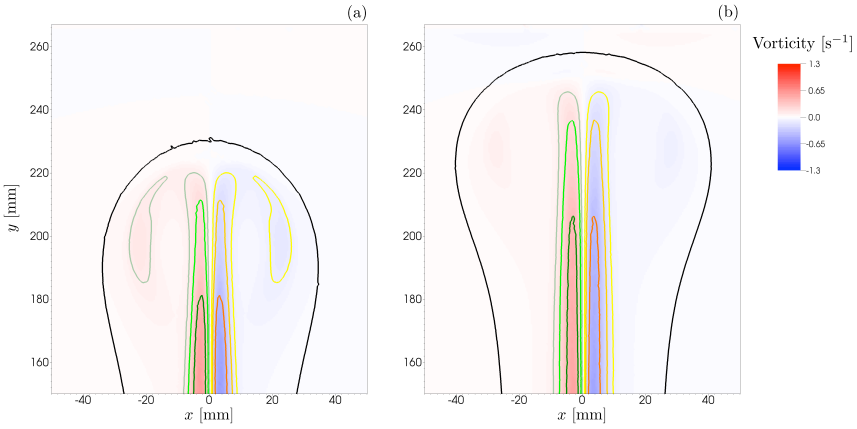

Figure 4.13: Head vorticity for the numerical model of case G6 shown at (a) $t = 250$ s and (b) $t = 300$ s following the start of injection. The outer black line is the 25.3 °C contour. Vorticity contours are provided at ± 0.4, ± 0.2, and ± 0.1 s^{-1}.

all material located within the 1% ΔT contour. The plume head will be taken as that section of the plume above $y = 200$ mm as this location represents an inflection point in the temperature contour. At the time shown in Figure 4.14(a), the R6 plume head has a volume of 560 mL. By comparison, the total volume of the G6 head at the time of Figure 4.14(b) is 210 mL, 57 mL of which is injected mass. Histograms of mass within the head for both cases are provided in Figure 4.15, and cumulative distribution functions are shown in Figure 4.16. Note that in computing the histograms and cumulative distribution functions for the injection plume, only the non-injected head mass is considered.

The R6 plume generated with a localized heat source has no backward-time LCS which surrounds the source material (ref. Figure 4.10(a)). Instead, the plume requires free access to mass near the tank bottom in order to warm the fluid and generate the buoyancy necessary to feed the plume. The R6 plume also lacks an LCS to shield the base of the plume head. Because of the lack of these additional LCS in the R6 case, the plume (both head and conduit) is markedly more efficient than the injection plume at radially sampling ambient material. These considerations are manifest in

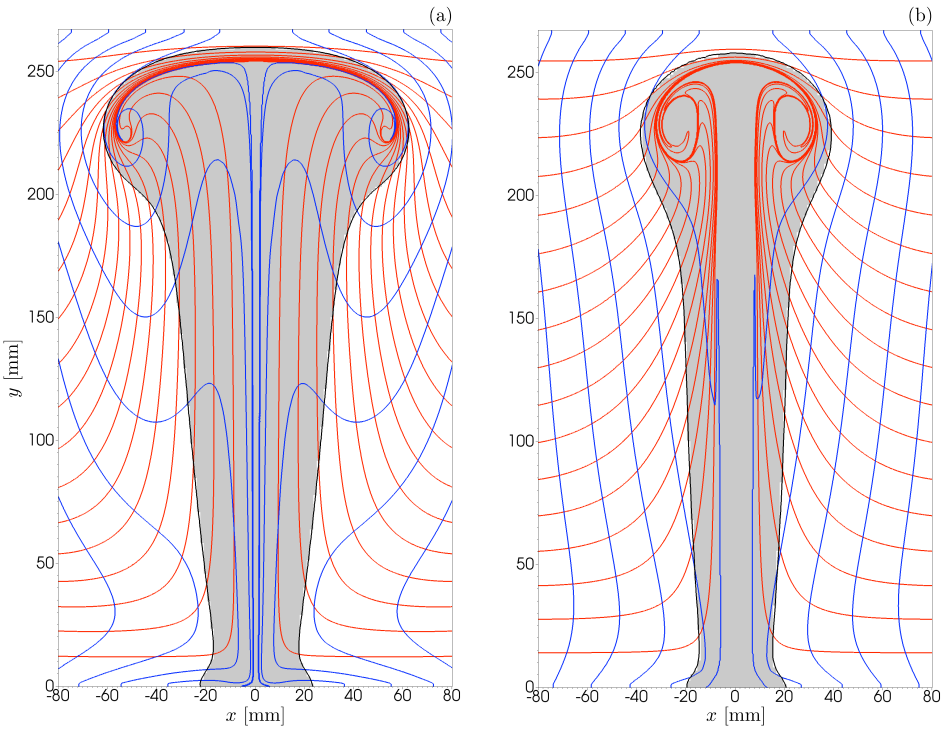

Figure 4.14: Vertical and radial origin of mass contained within (a) the plume generated via a localized heat source in case R6, and (b) the injection plume of case G6. The image of (a) is provided at $t = 3250$ s following heater activation, while the image of (b) corresponds to $t = 300$ s after the start of injection. Mass contours are shown at 15 mm intervals. Radial contours are represented as solid blue lines while the vertical contours are red. The solid black line and shaded region enclose all material that has a temperature of at least 25.7 °C.

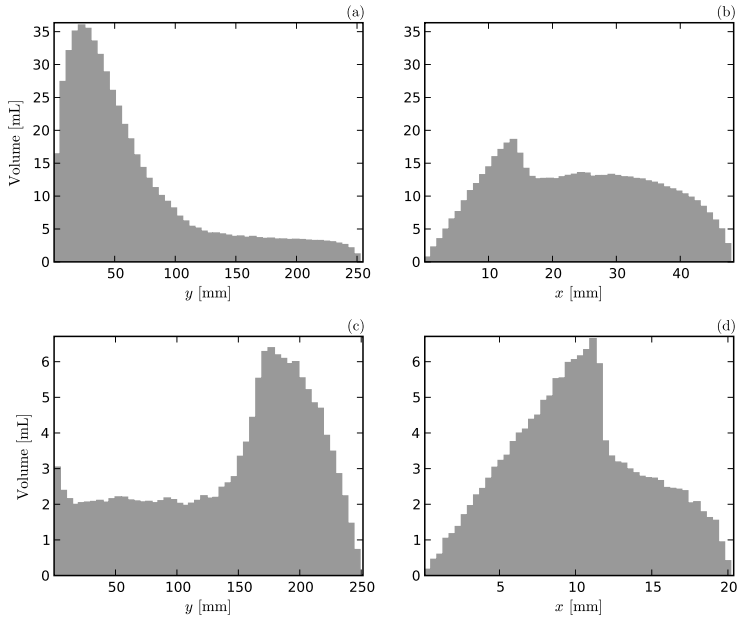

Figure 4.15: Histogram of vertical and radial origin for mass within the plume heads of cases R6 (a, b) and G6 (c, d) at the times shown in Figure 4.14. Note that only non-injected mass for the G6 case is considered.

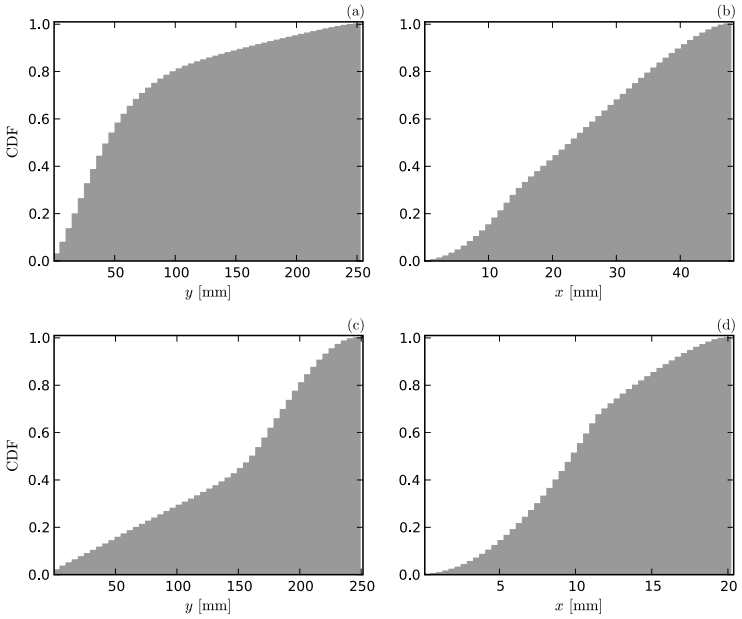

Figure 4.16: Cumulative distribution function for vertical and radial origin of mass within the plume heads of cases R6 (a, b) and G6 (c, d) at the times shown in Figure 4.14. Note that only non-injected mass for the G6 case is considered.

the mass contours of Figure 4.14(a). The siphoning of mass to feed the plume has left the radial origin contours (blue) substantially biased toward the heater along the base of the tank. As this mass enters the conduit, it begins to rapidly upwell thereby imparting the negative concavity observed for the radial origin contours within the conduit heat affected zone (gray). The velocity within the conduit is higher than the head rise velocity [13], therefore the material drawn into the conduit is eventually deposited into the head. The end result is that at the time shown in Figure 4.14(a), the R6 plume head contains mass that was originally positioned up to 48 mm from the plume centerline (ref. Figure 4.15(b)), with nearly 60% of the total head mass originiating from $|x| \geq 20$ mm (ref. Figure 4.16(b)).

However, the R6 plume does have one weakness in that the lower head vorticity results in significantly reduced vertical sampling efficiency. As the plume rises and the overlying fluid encounters the impenetrable leading edge LCS, the fluid gets squeezed radially outward. This effect displaces the radial origin contours in Figure 4.14(a) away from the plume centerline. But due to the lack of head vorticity, most of the overlying mass ends up in the wake of the rising head which imparts the positive concavity observed in the radial origin contours just outside the heat affected zone. At the time shown in Figure 4.14(a), the plume head contains mass originally located such that $0 \leq y \leq 250$ mm (ref. Figure 4.15(a)), but only 20% of the total head mass originates from $y \geq 100$ mm (ref. Figure 4.16(a)).

Inspection of Figure 4.14(b) shows that the injection plume also exhibits lateral deflection of the radial origin contours, but the effect is much less pronounced than that for case R6. The outermost LCS proves very effective at shielding the head from radial entrainment. At the time shown in Figure 4.14(b), the G6 head is composed entirely of mass originally located within 20 mm of the centerline (ref. Figure 4.15(d)), with 60% of the mass coming from $|x| \leq 11$ mm (ref. Figure 4.16(d)).

The injection plume also compresses overlying mass just as was observed for the

R6 case, but the head vorticity sweeps much of this compressed material into the head. The vertical origin contours are seen to wrap around the head scroll in Figure 4.14(b) as a consequence. As with the R6 case, the injection plume head is composed of mass originally positioned such that $0 \leq y \leq 250$ mm (ref. Figure 4.15(c)), but 70% of the G6 head mass originates from $y \geq 100$ mm (ref. Figure 4.16(c)).

4.3.5 Experimental characterization of plume head leading edge LCS

4.3.5.1 Starting plume leading edge vertical position

Let us now characterize the leading edge LCS for all six of the experimental cases in Table 4.2. In each case, the underlying material surface is grown from the LCS, and the apex of the grown structure is subsequently used to denote the location of the plume at a particular point in time. The resulting plume height data as a function of time are shown in Figure 4.17 for each of our six experimental cases. Note that the location data presented in Figure 4.17 do not capture the complete time history of each plume for two reasons.

First, as discussed previously (ref. Section 4.3.3), the flow must evolve sufficiently for a ridge in the backward-time FTLE to be visible. Consequently, the transient phase immediately following heater activation is not resolvable using our technique of locating the plume head, and the interested reader is referred to [11, 13] for examples of plume behavior during the initial transient period. The earliest plume head positions shown in Figure 4.17 are those for which the LCS could be readily identified.

Second, the PIV system is configured to analyze the lower 21.7 cm of corn syrup (ref. Figure 4.1), therefore the location of the plume head as it nears the top of the tank is also absent from Figure 4.17 for our experimental cases. In contrast, the numerical model of case N6 is computed using the full-sized fluid domain (*i.e.*, 26.5 cm per side), and consequently captures the plume behavior near the tank top.

Away from the initial and final transient periods, the plume head leading edge is

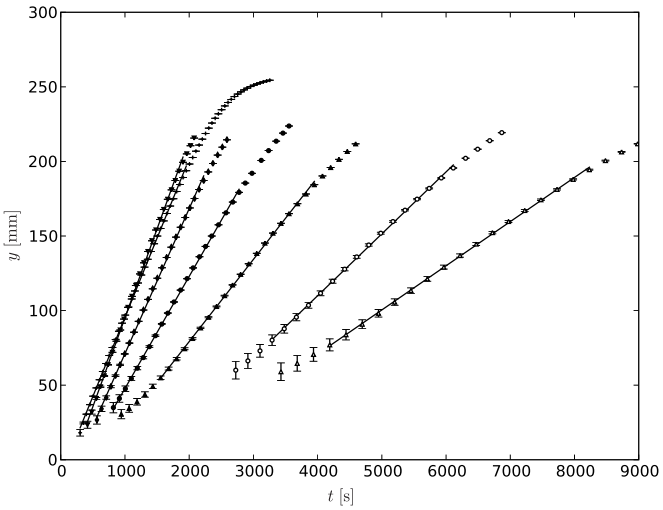

Figure 4.17: Plume head leading edge height above the tank bottom versus time for the six experimental cases. Best fit lines are shown in black for each case. (△) N1. (○) N2. (▲) N3. (●) N4. (⧫) N5. (▼) N6. (+) Numerical model of case N6.

seen to rise with a roughly constant velocity v_l in Figure 4.17, a qualitative observation which concurs with results obtained by other authors [38, 53, 11, 13, 14, 41]). A numerical estimate of the constant rise velocity for each of the cases in Table 4.2 is obtained from a least squares fit of head position versus time, and the computed values of v_l are provided in Table 4.4. The rise velocity for the numerical model of case N6, again identified as case R6, is also presented in the table for reference. Note that the best fit lines for position versus time are shown in Figure 4.17 spanning the individual data values used for the fit.

The error bars in Figure 4.17 and the velocity uncertainties of Table 4.4 were computed from a sensitivity analysis conducted for each individual case. As noted in Section 4.3, LCS are proxies for the underlying material surfaces, and hence some uncertainty is associated with the LCS and true location or shape of the corresponding material surface.

The sensitivity analysis for plume vertical position and rise velocity proceeds for each case by selecting the ridge of the LCS as the best guess for the location of the

Case	Q [W]	ΔT [°C]	Ra	m_l [s^{-1}]	v_l [mm/s]	δv_l [mm/s]	$\bar{a}$ [mm]	$v_l^{(s)}/v_l^{(\infty)}$
N1	0.44	10	1.3×10^5	5.7×10^{-4}	0.030	2.3×10^{-4}	65	0.54
N2	0.72	15	2.1×10^5	9.7×10^{-4}	0.042	3.4×10^{-4}	65	0.54
N3	0.70	25	2.0×10^5	1.5×10^{-3}	0.055	1.9×10^{-4}	51	0.63
N4	1.0	35	3.0×10^5	3.1×10^{-3}	0.075	3.3×10^{-4}	44	0.69
N5	1.4	45	4.1×10^5	5.6×10^{-3}	0.097	2.4×10^{-4}	38	0.73
N6	1.8	55	5.3×10^5	7.9×10^{-3}	0.12	1.6×10^{-4}	38	0.73
R6	1.8	55	5.3×10^5	2.1×10^{-2}	0.11	8.9×10^{-5}	38	0.73

Table 4.4: Experimental results for the six cases of Table 4.2. The numerical model of case N6 is identified as R6. Note that Q is the steady state power delivered to the syrup, and ΔT is the maximum temperature contrast achieved. The Rayleigh number provided is taken as $Ra = \alpha g Q d^2/\kappa^2 \mu c_p$, where all quantities are evaluated at ambient temperature.

underlying material surface. This guess is then offset as illustrated in Figure 4.18. The actual offsets for each case are selected loosely based on the FTLE ridge width, which can be quite large for the coldest cases (N1 to N3), but are generally on the order of $\pm 10\%$ of the plume's vertical position. The three initial estimates for the location of the material surface are then seeded with passive tracers and the tracers advected using the velocity field. Let $y^{(1)}(t)$, $y^{(0)}(t)$, and $y^{(-1)}(t)$ represent the instantaneous vertical position of the $+10\%$, baseline, and -10% scenarios, respectively for a particular case in Table 4.4. We define the uncertainty in vertical position of the baseline as

$$\delta y(\tau) = \frac{y^{(1)}(\tau) - y^{(-1)}(\tau)}{2}, \tag{4.18}$$

where τ is again the integration time.

Figure 4.19 presents two plots of the positional uncertainty for each of the cases in Table 4.4. The first provides a time history of $\delta y(\tau)$ relative to the initial uncertainty $\delta y(0)$, and the second provides the positional uncertainty relative to the leading edge location of the baseline case. Three items regarding the positional uncertainty decay are of note.

First, notice that for all cases the initial uncertainty as depicted in Figure 4.19(a)

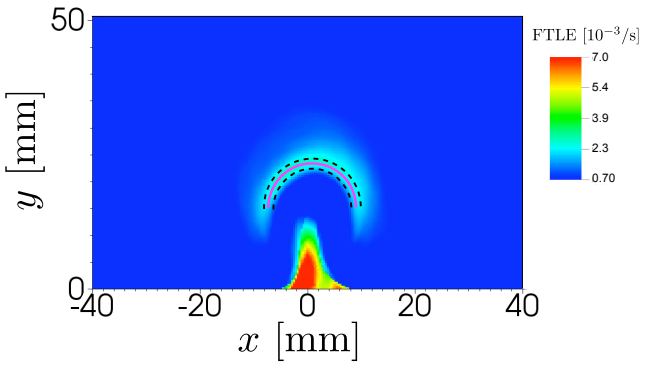

Figure 4.18: Position sensitivity analysis setup for case N6. The best estimate for the location of the leading edge material surface at $t = 420$ s following heater activation is shown as the purple line. The dashed black lines represent the best estimate shifted $\pm 10\%$ vertically. The pseudocolor background is the backward-time FTLE field.

decays by one order of magnitude in a roughly exponential fashion according to

$$\frac{\delta y(\tau)}{\delta y(0)} = e^{-m_l \tau}, \tag{4.19}$$

where m_l is the decay rate. The individual values of m_l obtained from a least-squares fit are tabulated in Table 4.4 for reference, however these values should be treated with caution, as they strongly depend on the initial time chosen for growing the material surface. Consider cases N6 and R6, for a moment. Although, case R6 is a numerical approximation of the experimental case N6, the m_l values recorded in Table 4.4 are significantly different. It turns out that a well-defined ridge in the backward-time FTLE field of the numerical model can be identified, and hence seeded to grow the leading edge material surface, 120 s earlier than for case N6.[9] During this 120 s interval, the strain rate normal to the leading edge LCS for case R6 is much larger in magnitude as shown in Figure 4.20. Consequently, the initial exponential decay rate of positional uncertainty exceeds that of case N6.

[9]The velocity field from the numerical model does not contain the experimental noise associated with case N6, and hence detecting ridges in the FTLE field is much easier.

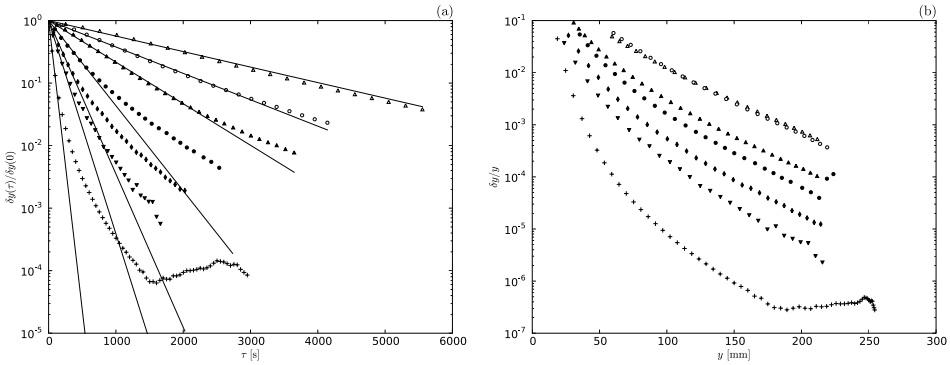

Figure 4.19: Evolution of positional uncertainty for cases of Table 4.4. (a) Time history of $\delta y(\tau)/\delta y(0)$. The best fit lines (solid) for exponential decay of uncertainty are also provided. (b) Uncertainty relative to plume leading edge vertical position y plotted as a function of plume position. (△) N1. (○) N2. (▲) N3. (●) N4. (⧫) N5. (▼) N6. (+) R6.

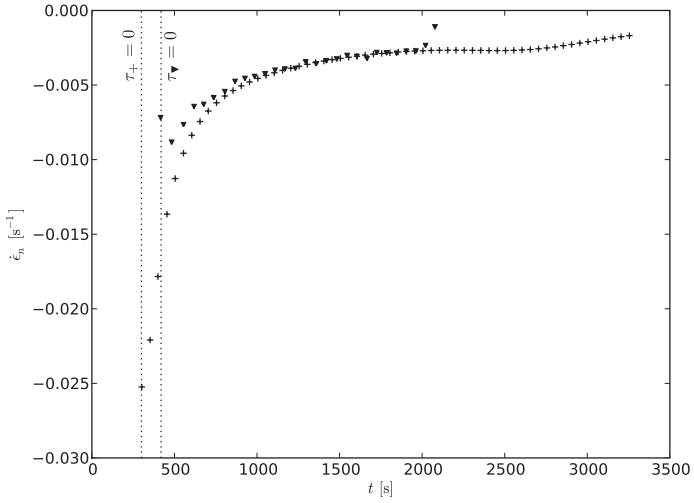

Figure 4.20: Strain rate normal to the leading edge LCS for cases N6 (▼) and R6 (+). The earliest time at which a ridge in the FTLE field can be reliably identified is depicted by a vertical dotted line for each case. These times correspond to $\tau = 0$ in Figure 4.19(a).

The second item of note regarding uncertainty in leading edge position is the observation from Figure 4.19 that once $\delta y(\tau)/\delta y(0) \approx 0.1$, the rate at which positional uncertainty decays begins to slow for the higher energy plumes. This behavior is directly linked to the time-dependence of the strain rate normal to the plume head. For illustration purposes, again consider the time profile of strain rate for case R6 presented in Figure 4.20. As demonstrated in the figure, the magnitude of the vertical velocity gradient across the plume head lessens as the plume evolves, and hence the rate at which fluid elements are attracted to the leading edge LCS decreases as well. Although more analysis is necessary, it does seem plausible that the temporally decreasing velocity gradient across the plume leading edge is a consequence of temperature dependent viscosity effects [52], particularly given that the coldest plume, case N1, exhibits exponential decay in position uncertainty for the duration of the experiment.

And finally, the decreasing decay rate for positional uncertainty suggests that higher Rayleigh number plumes are, from a stretching standpoint, more destructive immediately following heater activation than at later times. That is, a heterogeneity straddling the leading edge LCS of a high Rayleigh number plume will accumulate strain more rapidly following liftoff than it will farther away from the heat source.

With positional uncertainty available, an estimate of the uncertainty in leading edge rise velocity can also be determined using standard propagation of errors for a parameter determined from a least squares fit [69]. Let n represent the number of data points used in the fit, and the subscript i identify an individual data point. The rise velocity uncertainty δv_l then becomes

$$\delta v_l = \frac{\left[n^2 \sum_{i=1}^{n} t_i^2 \delta y_i^2 - 2n \sum_{i=1}^{n} t_i \delta y_i^2 \sum_{i=1}^{n} t_i + \sum_{i=1}^{n} \delta y_i^2 \left(\sum_{i=1}^{n} t_i \right)^2 \right]^{1/2}}{n \sum_{i=1}^{n} t_i^2 - \left(\sum_{i=1}^{n} t_i \right)^2}. \tag{4.20}$$

The computed values of uncertainty in rise velocity are presented in Table 4.4. In all cases, the assumed uncertainty in plume head leading edge position has a negligible impact on the inferred plume rise velocity. Readers should note that δv_l provided by Eq. 4.20 only captures that component of velocity uncertainty which is due to uncertainty in the location of the leading edge material surface. Errors that may be present in the underlying PIV velocity field (ref. Chapter II) are accounted for in the above analysis only insofar as they affect the decay rate of positional uncertainty.

We now quantitatively compare our rise velocities with previous work on laminar plumes. Using dimensional arguments, Batchelor [6] posited that for a steady laminar plume generated by a point source of heat, the velocity v_{cl} at a given location along the centerline should scale as

$$v_{cl} \sim \left(\frac{\alpha g Q}{\mu_c c_p} \right)^{1/2}. \tag{4.21}$$

Moses *et al.* [53] later conducted a series of experiments on laminar, thermal plumes generated with localized heat sources in essentially isoviscous fluids, and found that Batchelor's scaling also applies to the plume head rise velocity. Their data were well described by a relation of the form

$$v_l = \gamma_m \left(\frac{\alpha g Q}{\mu_c c_p} \right)^{1/2}, \tag{4.22}$$

where γ_m is a proportionality constant. Although remaining within an isoviscous regime, Kaminski and Jaupart [38] extended the work of Moses *et al.* using fluids spanning a larger range of Prandtl numbers and found that γ_m was a function of Prandtl number. Employing the infinite Prandtl number asymptotic expansion of Worster [77], Kaminski and Jaupart proposed that

$$\gamma_m = (0.57 \pm 0.02) \left(\frac{\ln \epsilon^{-2}}{2\pi} \right)^{1/2}, \tag{4.23}$$

where ϵ is a root of $\epsilon^4 \ln \epsilon^{-2} = Pr^{-1}$, and $Pr > 7$. Davaille *et al.* [13] further incorporated the effects of temperature dependent viscosity yielding

$$\gamma_m = (0.71 \pm 0.03) \left(\frac{\eta + 1}{\eta + 3/2} \right) \left(\frac{\ln \epsilon^{-2}}{2\pi} \right)^{1/2}, \tag{4.24}$$

where $\eta = \mu_c / \mu_h$ is the viscosity contrast between the ambient fluid and hottest fluid near the heater.

Our plume rise velocities are plotted against

$$[(\eta + 1)/(\eta + 3/2)] \left(\ln \epsilon^{-2} / 2\pi \right)^{1/2} \left(\alpha g Q / \mu_c c_p \right)^{1/2}$$

in Figure 4.21 below. As expected, the rise velocity of the plume head is quite well described by a scaling of the form given by Eq.'s 4.22 and 4.24. A least squares fit of the data provides the linear relationship

$$v_l = 0.57 \left(\frac{\eta + 1}{\eta + 3/2} \right) \left(\frac{\ln \epsilon^{-2}}{2\pi} \right)^{1/2} \left(\frac{\alpha g Q}{\mu_c c_p} \right)^{1/2} - 4.8 \times 10^{-5}, \tag{4.25}$$

where v_l has units of m/s. Note that Eq. 4.25 can be readily non-dimensionalized as

$$v_l^* = 0.57 \left(\frac{\eta + 1}{\eta + 3/2} \right) \left(\frac{\ln \epsilon^{-2}}{2\pi} \right)^{1/2} Ra^{1/2} \tag{4.26}$$

with $v_l^* = (v_l + 4.8 \times 10^{-5}) d / \kappa$, and $Ra = \alpha g Q d^2 / \kappa^2 \mu_c c_p$ representing a Rayleigh number based on the heater power and depth of the fluid layer d.

As with Kaminski and Jaupart [38], our best fit line in Figure 4.21 does not pass through the origin. In their analysis, Kaminski and Jaupart attribute the offset to an overestimate of the heat delivered to the fluid. The authors observe that some heat must be transferred to their experimental apparatus, and reckon that the non-zero v_l intercept is a consequence of this lost heat. Kaminski and Jaupart eliminate the

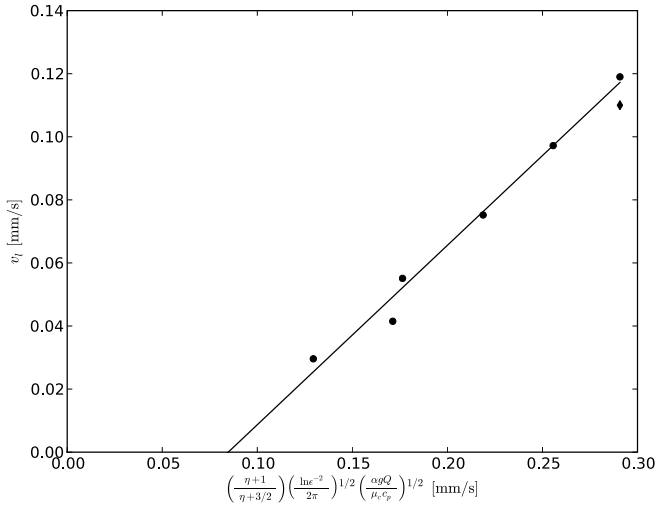

Figure 4.21: Plume head rise velocity as a function of heater power for cases of Table 4.4 (•). The black line is the best fit determined via least squares. The numerical model (case R6) is shown for reference (⧫), but is not used in the least squares fit.

offset by refitting their data to a version of Eq. 4.22 having the form

$$v_l = c_3 \xi (Q - Q_0)^{1/2}, \tag{4.27}$$

where $\xi = (\ln \epsilon^{-2}/2\pi)^{1/2} (\alpha g/\mu_c c_p)^{1/2}$, c_3 is an empirically determined constant, and Q_0 is taken as the heat lost to the apparatus. The authors find that the parameter Q_0 is essentially independent of heater power but a function of Prandtl number for their experiments.

For our plumes, the basal thermal boundary layer is wider than the heater (ref. Figure 4.3), therefore heat is certainly lost to the tank bottom. As shown in Figure 4.28, we find that our data can also be fit to Eq. 4.27 yielding the relation

$$v_l = 0.44 \left(\frac{\eta+1}{\eta+3/2}\right) \left(\frac{\ln \epsilon^{-2}}{2\pi}\right)^{1/2} \left(\frac{\alpha g (Q - 0.36)}{\mu_c c_p}\right)^{1/2}. \tag{4.28}$$

While the rise velocity data seem to be well described by Eq. 4.28, further analysis

does not support the notion that 0.36 W of heat is lost to the tank structure regardless of the heater operating power Q.

Although the results have not been detailed here, a finite volume model [37] was run for each of our experimental plumes to reconstruct the temperature field on the uniform $(\Delta x, \Delta y, \Delta z) = (2.8, 2.8, 5)$ mm grid of the PIV data (ref. Figure 4.1). The model used the PIV velocity field as an input along with the known thermal boundary conditions. Unlike the Fluidity model employed in case R6, the finite volume thermal model simulated heat flow to the acrylic tank bottom (*i.e.*, the finite volume model did not use a simplifying adiabatic boundary condition for the tank bottom). The tank bottom was also discretized using a $(\Delta x, \Delta y, \Delta z) = (2.8, 2.8, 5)$ mm grid. For cases N1 and N2, temperature contours extracted from the finite volume model match those available from liquid crystal thermometry (ref. Section 4.2) to within 0.05 °C for temperatures spanning $T = 25.2$ °C to $T = 26.5$ °C. A comparison of the finite volume thermal model and liquid crystal derived temperatures for case N1 is presented in Figure 4.23 for reference.

Although by no means an exhaustive assessment, the agreement observed over the temperature range in which liquid crystal data are available suggests the finite volume thermal model has acceptable fidelity to the measured temperature field in these two cases. When we use the full temperature field computed from the finite volume model to infer power delivered to the syrup for cases N1 and N2, we find that 0.18 W and 0.27 W, respectively, are lost to the tank bottom once the starting plumes have entered the constant rise velocity regime. Note that we have not considered the finite volume model for cases N3-N6 in our analysis due to the low velocities observed in the conduit (ref. Section 4.3.2).[10] Nevertheless, our observations regarding cases N1 and N2 suggest that the offset value $Q_0 = 0.36$ in Eq. 4.28 is capturing more than just heat lost to experimental apparatus. That is, Q_0 may be partially compensating for

[10]The conduit velocities just above the heater have an appreciable affect on heat transfer and ultimately the plume temperature.

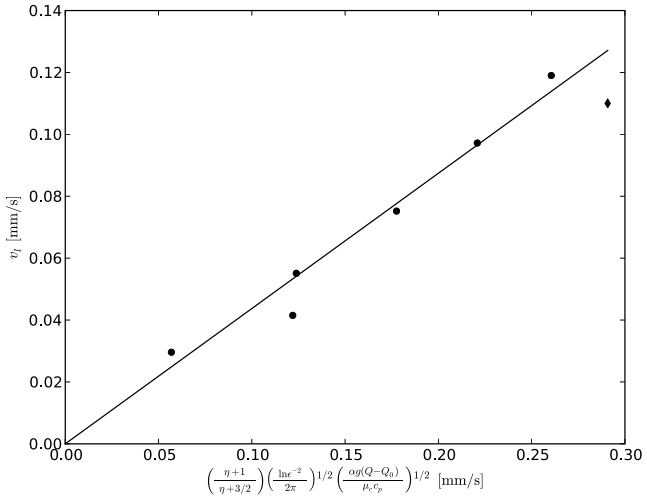

Figure 4.22: Plume head rise velocity as a function of adjusted heater power $(Q - Q_0)$ for cases of Table 4.4 (●). The black line is the best fit determined via least squares. The numerical model (case R6) is shown for reference (⧫), but is not used in the least squares fit. Note that due to the adiabatic lower boundary condition, $Q_0 = 0$ for the numerical model.

the varied influence of sidewalls on rise velocities due to head diameter (see below) as well as unmodeled effects of temperature dependent viscosity in Eq. 4.25. In particular with regard to the latter, Eq. 4.25 may need to be modified to more accurately capture the effective viscosity against which the rising plume must work instead of simply assuming μ_c [52, 4].

Regardless of how Q_0 relates to heat loss, both Eq.'s 4.25 and 4.28 make it clear that the observed rise velocity of our plumes is significantly less than that predicted by the works of Kaminski and Jaupart [38] and Davaille *et al.* [13]. A fairly significant source for the discrepancy is undoubtedly due to excessive viscous drag arising from the tank sidewalls. Happel and Bart [32] find that the rise velocity of a sphere of diameter a in fluid contained by a tall, square tube of width w is provided by

$$v_l^{(s)} \approx v_l^{(\infty)} \left(1 - 1.903\frac{a}{w}\right), \tag{4.29}$$

where $v_l^{(\infty)}$ is the Stokes' law rise velocity for the sphere in fluid having infinite lateral

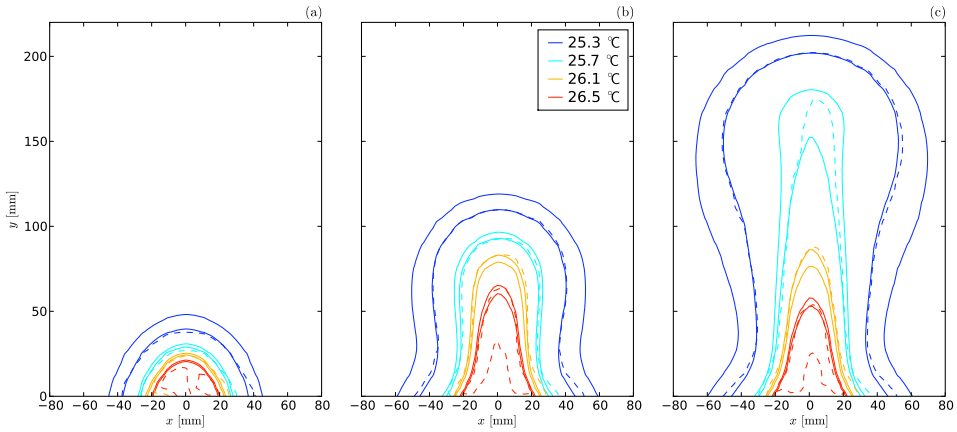

Figure 4.23: Comparison of temperature contours for case N1 obtained from the finite volume thermal model (solid lines) and determined experimentally via liquid crystal thermometry (dashed lines). For each liquid crystal derived contour, corresponding finite volume contours are shown at ±0.05 °C. Note that the isolated, lowermost dashed red line visible in figures (b) and (c) should be ignored as it is an artifact caused by the fluid temperature exceeding the color play of the liquid crystals (ref. Chapter II). Contours are shown at (a) $t = 1900$ s, (b) $t = 5200$ s, and (c) $t = 8500$ s.

extent. A crude estimate of the sidewall effects on our plume rise velocities can be computed using Eq. 4.29 and the time-averaged head diameter $\bar{a}$. We note that the time-averaged diameter $\bar{a}$ of the leading edge LCS (ref. Table 4.4) during the constant rise velocity regime for our coldest plume, case N1, is 65 mm (25% of the tank width) while that of case N6 is 38 mm (14% of the tank width). The resulting ratios of $v_l^{(s)}/v_l^{(\infty)}$, presented in Table 4.4, suggest that even our smallest diameter plume from case N6 exhibits a rise velocity deficit of nearly 30%. Therefore, the influence of sidewalls is likely significant for all of our plumes.

4.3.5.2 Starting plume leading edge diameter

Until the plume approaches the top of the tank, the shape of the leading edge LCS is well described by the upper portion of an ellipsoid having the form

$$\frac{x^2}{(a/2)^2} + \frac{(y-y_0)^2}{(b/2)^2} + \frac{z^2}{(a/2)^2} = 1 \tag{4.30}$$

as demonstrated in Figure 4.24 for case R6.[11] Note that the y-axis has been chosen to align with the plume centerline, and $y_0 = y_0(t)$ in Eq. 4.30 represents the center of the ellipsoid. In the following discussion we provide an analysis of the ellipsoidal shape for each of the experimental cases in Table 4.2 as well as the numerical model of case N6.

The time history of the ellipsoid axes for each of our experimental cases is shown in Figure 4.25. As apparent from Figure 4.25(c), the ellipsoid axes are equal in length to within $\pm 20\%$ until the plume aproaches the tank top. Hence, the ellipsoid is nearly spherical for most of the starting plume's ascent. The data of Figures 4.25(a) and (b) suggest that during part of the plume's evolution both the diameter a and the axis b of the bounding ellipse grow linearly with time. The corresponding constant growth rates $\dot{a}$ and $\dot{b}$ determined from a least squares fit are provided in Table 4.5.

However, the time period during which the ellipsoid axes grow in an approximately linear fashion does not necessarily correspond to the same interval where the plume rise velocity is constant. We have identified the difference in Figures 4.25(a, b) as follows. The start of the constant rise velocity regime for each case is illustrated by a red symbol in the figure, and the period during which the axes are taken to grow linearly is shown spanned by a solid line. The line was determined from a least squares fit of the underlying data for each case, and that portion of the line which overlaps the constant rise velocity regime is shown in red. We observe that for all cases except

[11] For an alternative description using the Rankine fairing, see [53].

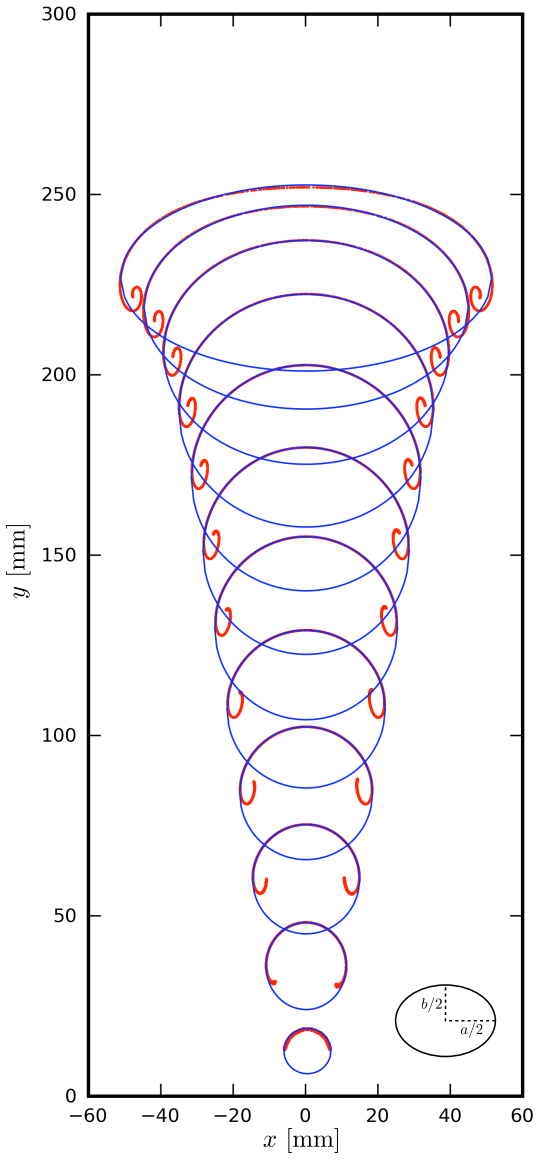

Figure 4.24: Ellipsoidal fit of plume leading edge material surface for numerical model case R6 shown at 250 s intervals starting from $t = 300$ s. The grown material surface is shown in purple, and the best fit ellipsoid determined via least squares is depicted in blue.

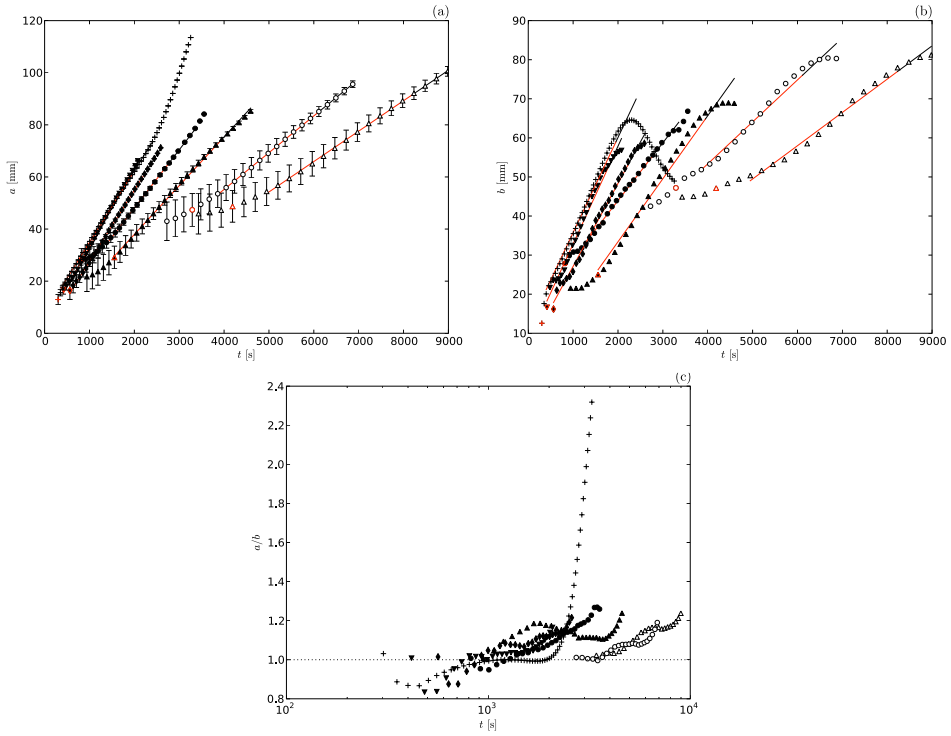

Figure 4.25: Time evolution of the ellipsoidal axes. See text for explanation of colors. (a) Ellipsoid diameter a. (b) Ellipsoid b-axis. Note that the error bars have been removed for clarity (ref. Figure 4.26). (c) Ratio of ellipsoid diameter to b. (△) N1. (○) N2. (▲) N3. (●) N4. (♦) N5. (▼) N6. (+) R6.

N1 and N2 the ellipsoid axes start growing in a linear fashion at roughly the same time the plume begins to rise with a constant velocity. Given the large uncertainty in initial head shape, it is quite possible the observed delay in onset of linear axis growth for cases N1 and N2 is not real. Nevertheless, the diameter of the leading edge LCS continues growing linearly in each case after the plume has stopped rising at the constant speed v_l. Overall, the period of constant growth rate for the ellipsoid b-axis more closely mirrors the interval of constant rise velocity than does a.

The same sensitivity analysis described in Section 4.3.5.1 has also been used to compute uncertainty in the ellipsoid axes. We define the uncertainty in diameter and

Case	Q [W]	ΔT [°C]	Ra	m_a [s^{-1}]	$\dot{a}$ [mm/s]	$\delta\dot{a}$ [mm/s]	m_b [s^{-1}]	$\dot{b}$ [mm/s]	$\delta\dot{b}$ [mm/s]
N1	0.44	10	1.3×10^5	2.3×10^{-4}	0.012	7.8×10^{-4}	9.2×10^{-5}	0.0085	1.1×10^{-3}
N2	0.72	15	2.1×10^5	3.7×10^{-4}	0.014	9.3×10^{-4}	1.9×10^{-4}	0.011	1.3×10^{-3}
N3	0.70	25	2.0×10^5	6.2×10^{-4}	0.019	5.7×10^{-4}	4.7×10^{-4}	0.016	7.5×10^{-4}
N4	1.0	35	3.0×10^5	1.3×10^{-3}	0.022	4.7×10^{-4}	8.6×10^{-4}	0.015	7.3×10^{-4}
N5	1.4	45	4.1×10^5	2.1×10^{-3}	0.028	5.2×10^{-4}	1.1×10^{-3}	0.021	6.1×10^{-4}
N6	1.8	55	5.3×10^5	3.3×10^{-3}	0.031	3.2×10^{-4}	1.8×10^{-3}	0.025	3.8×10^{-4}
R6	1.8	55	5.3×10^5	9.4×10^{-3}	0.027	6.7×10^{-5}	5.8×10^{-3}	0.024	1.1×10^{-4}

Table 4.5: Ellipsoid axis parameters. Heater power Q, temperature contrast ΔT, and characteristic Rayleigh number Ra are repeated from Table 4.4 for reference.

b-axis of the baseline ellipsoid as

$$\delta a(\tau) = \frac{a^{(1)}(\tau) - a^{(-1)}(\tau)}{2},\ \delta b(\tau) = \frac{b^{(1)}(\tau) - b^{(-1)}(\tau)}{2} \tag{4.31}$$

where τ is again the integration time. Figure 4.26 presents plots of the ellipsoid axis uncertainty for each of the experimental cases as well as the numerical model. As was found for the plume leading edge position, uncertainty in the diameter a and axis b of the ellipsoid decay exponentially at least over the initial period of the plume evolution according to

$$\frac{\delta a(\tau)}{\delta a(0)} = e^{-m_a \tau},\ \frac{\delta b(\tau)}{\delta b(0)} = e^{-m_b \tau}. \tag{4.32}$$

The individual decay rates m_a and m_b obtained from a least squares fit are listed in Table 4.5. In each case, $m_a \approx m_l/2$ and $m_b \approx m_a/2$. The slower decay in uncertainty of a and b as compared to that observed for leading edge position is due to the change in character of the leading edge LCS illustrated in Figure 4.6. Namely, as the LCS begins to curl upward around the nascent scroll, the LCS ceases to attract nearby fluid elements. Instead, as discussed in relation to Figure 4.6, fluid parcels in close proximity to the LCS curls are alternately attracted, sheared, or even repelled. The end result in terms of the ellipsoid axes is that uncertainty in these parameters decays slower than that observed for the vertical position of the plume.

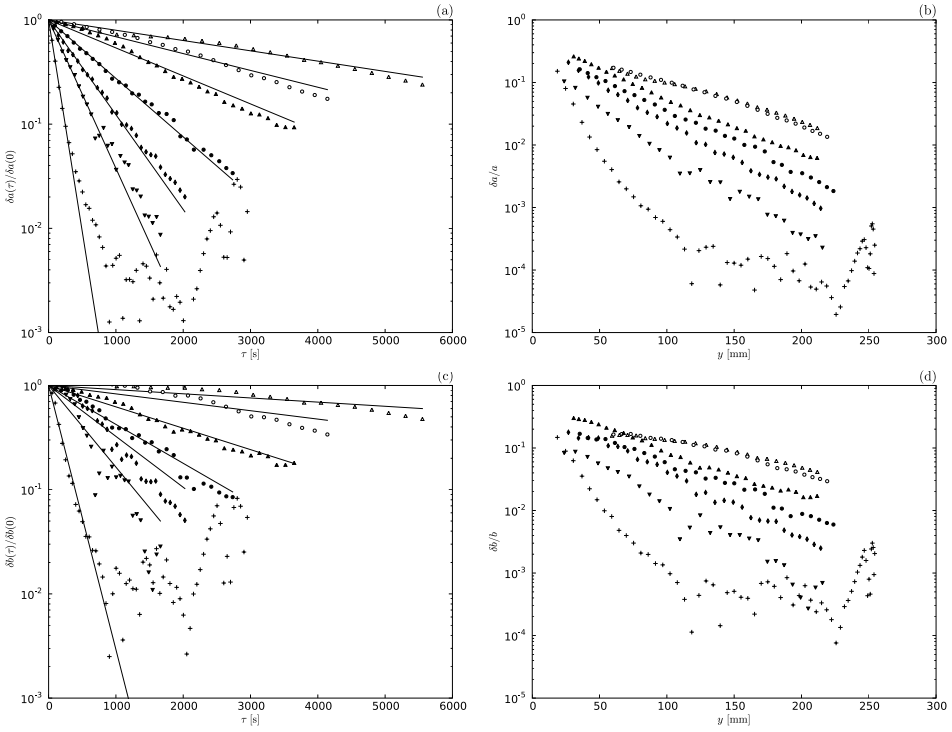

Figure 4.26: Evolution of ellipsoid axis uncertainty for cases of Table 4.5. (a, c) Time history of $\delta a(\tau)/\delta a(0)$ and $\delta b(\tau)/\delta b(0)$, respectively. The best fit lines (solid) for exponential decay of uncertainty are also provided. (b, d) Ellipsoid axis uncertainty relative to axis dimension plotted as a function of plume leading edge position. (△) N1. (○) N2. (▲) N3. (●) N4. (⧫) N5. (▼) N6. (+) R6.

Before moving on, one other item regarding Figure 4.26 deserves attention. Notice that δa and δb for case R6 seem to reach a lower limit at around $\tau = 1000$ s. This behavior is a consequence of trying to fit an ellipsoid to data that span only the upper portion of the ellipsoid (ref. Figure 4.24) and results in the location of the ellipse center, diameter, and b-axis all being somewhat poorly constrained. Thus, once the uncertainty in axis dimensions has decayed to a given level, further refinement becomes difficult.

The constant growth rates for the leading edge diameter and ellipsoid b-axis along with the associated uncertainties are presented in Table 4.5. The growth rates are plotted versus leading edge rise velocity in Figure 4.27. Note that the growth rate uncertainties, $\delta\dot{a}$ and $\delta\dot{b}$, recorded in Table 4.5 have been determined using Eq. 4.20 with y_i replaced by a_i or b_i, respectively.

As illustrated in Figure 4.27, the constant growth rates $\dot{a}$ and $\dot{b}$ are found to be linear functions of the plume rise velocity

$$\begin{aligned} \dot{a} &= 0.22 v_l + 5.8 \times 10^{-6} \\ \dot{b} &= 0.17 v_l + 3.9 \times 10^{-6}, \end{aligned} \tag{4.33}$$

where units are in m/s. The non-zero intercepts in Eq. 4.33 are most likely a consequence of sidewall effects. A retarded rise velocity would result in enhanced growth rates as the head swells to accommodate the extra mass flux from the conduit.

In terms of prior work, data regarding the head dimensions of starting plumes generated using localized heat sources are scarce. Moses *et al.* [53] measure the diameter of plumes generated in water, methanol, and oils via shadowgraphs and find that the head diameter scales as $a \sim t^{1/2}$, which clearly differs from our finding that $a \sim t$. Moses *et al.* do not report dimensions equivalent to our ellipsoid b-axis.

Shlien [61] investigates the head morphology of laminar plumes generated by

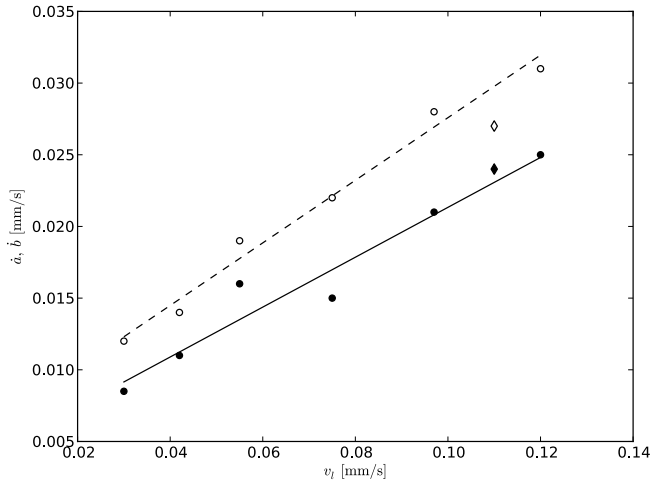

Figure 4.27: Ellipsoid axes growth rates versus leading edge rise velocity. Values of $\dot{a}$ from Table 4.5 are plotted as ($\circ$) and values of $\dot{b}$ are shown as ($\bullet$). The best fit line determined via least squares for $\dot{a} = \dot{a}(v_l)$ is shown dashed while that for $\dot{b} = \dot{b}(v_l)$ is shown solid. The numerical model, case R6, is represented as an open or solid diamond for reference, but was not used in the fits.

Ohmic heating in a water solution also using shadowgraphs and finds that the plume head diameter scales as $a \sim t$. Shlien does not fit an ellipsoid to the extracted head shapes, but measurements taken along the plume centerline from the plume leading edge to the center of the scrolls are provided. This particular measurement, definitionally similar to our ellipsoid b-axis (ref. Figure 4.24), is also reported to scale linearly with t, which again matches our findings.

Other studies (*e.g.*, [39, 13]) have used temperature contours to investigate the plume head diameter and hence are not directly comparable to the leading edge LCS. The reason why our observed ellipsoid axis growth rates differ from those of Moses *et al.* warrants further investigation.

4.4 A metric for the morphology of flow-induced deformation

In the preceding sections, we have explored the use of Lagrangian coherent structures and underlying material surfaces to characterize the position, head shape, and

mechanisms of entrainment for thermal plumes. We would like to now turn our attention to how mass deforms under the influence of the flow.

Clearly, any observed spatial structure in geochemical observations at a given volcanic feature, such as the bilateral asymmetry observed at Hawaii (*e.g.*, [1]), is not merely a reflection of the most immediate convective process that deposited the mass at the surface. Instead, the surface condition of volcanic products is a summation of the full stretching (and chemical mixing) history the mass has incurred. Nevertheless, we can still obtain important insight into the nature of mantle convection and the distribution of heterogeneities within based on how a given flow phenomenon is expected to alter the stretching history. Consider the scenario, for example, where filamentary structures are found in a specific arrangement at some volcanic feature, but the postulated flow mechanism responsible for providing the magma source is believed to be incapable of generating such an arrangement. In this scenario, either the noted surface observation is an inherent characteristic of a particular mantle reservoir, or the presumed flow phenomena responsible for producing the volcanic feature inadequately explains circumstances known to occur.

The work presented here is heavily influenced by the correlation dimension of Grassberger and Procaccia [27], the application of the correlation dimension to mantle convection by Schmalzl and Hansen [57], as well as investigations regarding deformation of fluid within the conduit of thermal plumes conducted by Farnetani and Hofmann [15, 16]. In a manner analogous to the correlation dimension [27], our goal is to develop a metric which yields a rough estimate of the characteristic dimensionality assumed by an infinitesimal sphere as it deforms under an incompressible flow. That is, we are interested in developing a tool that conveys whether the flow transforms the infinitesimal sphere into a cigar (a 1D feature) or a sheet (a 2D feature), and we would like to use that tool to predict the generic dimensionality of macroscopic inclusions (*i.e.*, whether a large spherical heterogeneity is transformed into a filament

or a sheet-like structure).

Of course, we have already discussed certain aspects of stretching within the flow. As discussed in Sections 4.3.1 and 4.3.2, fluid elements situated sufficiently close to a backward-time LCS are often attracted to and stretched out along the structure. Hence for those elements which interact strongly with an attracting LCS, the dimensionality of the LCS provides some insight into the shape assumed by affected fluid. If the LCS is a 2D surface similar to the leading edge LCS of our thermal plumes (ref. Figure 4.4), then some of the fluid encountering the structure will certainly be stretched into sheets.

However, not all fluid elements interact directly with backward-time LCS, and of those parcels which do, not all are transformed the same. So the LCS picture does not in itself provide the information we seek. But, by constructing a map of how the aggregate flow transforms all elements, we can obtain an instantaneous snapshot of the geometric state of spherical fluid elements within the flow. As will be shown for our thermal plumes, the shape fluid parcels assume is intimately linked to where such elements are situated at the instant of heater activation.

Consider the sketch of Figure 4.28 where a flow is shown to transform the unit cube into a rectangular slab. Note that the discussion equally applies to the unit sphere, but the concepts are somewhat easier to visualize using hexahedra. The lengths of the deformed rectangle's sides are taken as s_1, s_2, and s_3, arranged in order of decreasing magnitude. Conceptually, it is quite clear that if $s_1 \gg \{s_2, s_3\}$, the deformed cube will look more like a 1D line than a 2D sheet or a 3D cube. Similarly if $\{s_1, s_2\} \gg s_3$ and $s_1 \approx s_2$, the deformed shape will be very sheet-like. These simple lines of reasoning are sufficient to construct a logic test to flag whether 1D, 2D, or 3D structures are produced by a flow. A significant challenge, however, is forming a basis for evaluating the necessary thresholds (*e.g.*, how close must s_1 be to s_2 for the condition $s_1 \approx s_2$ to hold). There are countless ways the side lengths can be used

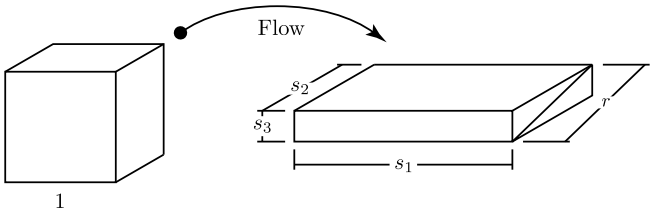

Figure 4.28: Deformation of the unit cube by an arbitrary flow.

Shape	Ψ
Sphere (3D)	2
Sheet (2D)	1
Pencil (1D)	0

Table 4.6: Characteristic dimensionality assessment provided by the metric Ψ.

to compute ratios of perimeter, area, and other geometrical measures from which the thresholds can be formed, but we have had the most success by comparing the major axis length to the resultant r, where

$$r = \sqrt{s_2^2 + s_3^2}. \tag{4.34}$$

That is we define the shape metric Ψ as

$$\Psi = \frac{r^2}{s_1^2}, \tag{4.35}$$

where $s_1 \geq s_2 \geq s_3$. As the unit cube (or sphere) is stretched into a pencil, $s_1 \to \infty$ and $\Psi \to 0$. If the deformed structure is essentially 2D, then $\Psi = 1$, while $\Psi = 2$ indicates that the original 3D shape has more or less been preserved. The limiting values of Ψ and the corresponding shapes are provided for reference in Table 4.6.

Of course, to apply Eq. 4.35, some method of computing three characteristic lengths of the deformed sphere is required. If these characteristic lengths are normalized by the starting length, then they are simply stretch factors, and obtaining a measure of the rate at which stretching occurs was the underlying motivation behind

the development of Lyapunov exponents in Section 4.3.1. Reflecting back on Eq. 4.8, the square roots of the eigenvalues of the matrix $\boldsymbol{M} = (\boldsymbol{\nabla}_0 \boldsymbol{F})^T \boldsymbol{\nabla}_0 \boldsymbol{F}$, where $\boldsymbol{M}$ is also known as the right Cauchy-Green deformation tensor [43], were shown for the linearized flow to provide the stretching incurred for vectors initially aligned with the eigenvectors of $\boldsymbol{M}$. Therefore if the axes of the unit sphere are chosen to parallel with the eigenvectors of $\boldsymbol{M}$, then the axes of the ellipsoid produced by the flow will have lengths provided by the square roots of the eigenvalues of $\boldsymbol{M}$. That is, the square roots of the eigenvalues of the matrix $\boldsymbol{M}$ provide the principal stretch factors we seek.

In practice, we actually compute the singular value decomposition (SVD) of the matrix $\boldsymbol{\nabla}_0 \boldsymbol{F}$ since the singular values are the principal stretch factors (*i.e.*, no square roots needed) [62]. As an added bonus, the SVD returns eigenvectors of the matrix $\boldsymbol{\nabla}_0 \boldsymbol{F} (\boldsymbol{\nabla}_0 \boldsymbol{F})^T$ which align with the axes of the resulting ellipsoid (*i.e.*, the eigenvectors of $\boldsymbol{\nabla}_0 \boldsymbol{F} (\boldsymbol{\nabla}_0 \boldsymbol{F})^T$ provide the orientation of the stretched ellipsoid, while the eigenvectors of $\boldsymbol{M}$ provide the initial orientation of the sphere). So by computing the finite-time Lyapunov exponent field using the SVD and keeping some additional data, all the information needed to determine Ψ is readily available.

Before proceeding to discuss application of the shape metric, we would like to point out that Subramanian *et al.* [63] have developed an alternative means of computing the principal stretches and orientations of the infinitesimal ellipse. Instead of advecting passive tracers and computing the gradient of the time-t map as described in the present text, the authors integrate a system of six, coupled ordinary differential equations at arbitrary points of interest. In certain circumstances, the method of Subramanian *et al.* can provide superior accuracy over the technique we have used. In particular, recall that Lyapunov exponents are obtained from a linearization about a fluid element trajectory as the element is advected by the velocity field (ref. Eq. 4.4). In regions of very high stretching, as would be experienced at the apex of the leading edge LCS, passive tracers can separate so strongly that the linearization breaks down.

Physically, the stretching is of sufficient strength that the computational equivalent of the infinitesimal sphere no longer deforms into an ellipse under the flow, but instead takes a more complicated shape. The issue can be readily visualized via the evolution of the red circle in Figure 4.5, which in no way resembles an ellipsoid in the deformed state. The end result is that the product of the stretch factors computed in regions with high stretching is no longer guaranteed to equal one as required for incompressible flows. While the breakdown in the linearization can be avoided by increasing the seeding density of passive tracers or by reducing the integration time τ, both approaches have significant drawbacks. For the flows we consider, however, obtaining the stretch factors from the FTLE field computations provides sufficient accuracy.

Figure 4.29 provides the shape metric Ψ evaluated for case N6 as well as the numerical model case R6. The metric is computed for the plumes at the time instant each has risen to a height of $y = 200$ mm above the tank bottom, where height is measured using the apex of the leading edge LCS as discussed in Section 4.3.5. In constructing Figure 4.29, however, we have elected to show the metric values for the location of the mass at time $t = 0$. In other words, Figure 4.29 is a predictive map depicting, at $t = 0$, the shape spheres of fluid will have assumed by the time the plume has risen 200 mm.

A couple of observations regarding Figure 4.29 are of note. Most obvious is the noise present for the experimental case N6. The fluctuations observed above $y = 125$ mm are a consequence of noise in the PIV velocity vectors which, given the relatively long period between successive scans of the tank (ref. Chapter II), cause random errors affecting a PIV vector to persist in the velocity field for an artificially long time. These velocity vector errors then cumulatively perturb the path taken by individual passive tracers, and for regions with relatively weak stretching overall, can moderate the rate at which the unit sphere deforms. Below $y = 125$ mm and close to the plume

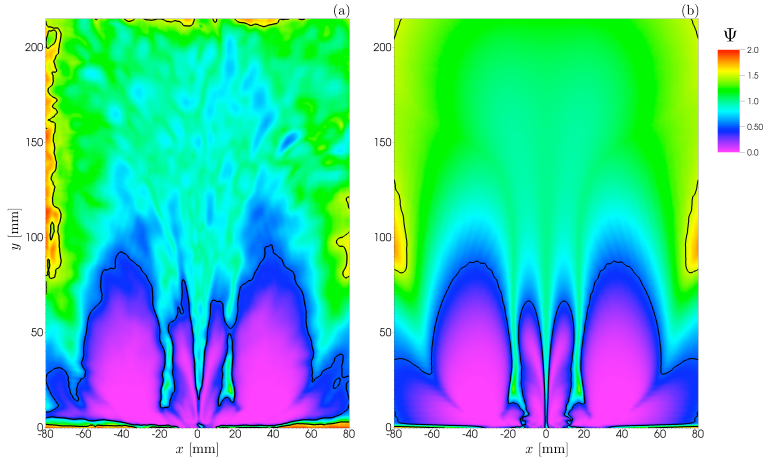

Figure 4.29: Shape metric for cases (a) N6 and (b) R6. Metric is computed using an integration time $\tau = 2000$ s, at which point the plume has risen 200 mm as measured using the leading edge LCS. The images presented, however, show the configuration of mass at $t = 0$. Two contours for $\Psi = 0.5, 1.5$ are shown as solid black lines.

centerline, the fluctuations in Figure 4.29(a) arise from PIV velocity errors caused by strong velocity gradients near the plume centerline (ref. Chapter III).

Second, the shape metric is directly computing the shape of the transformed infinitesimal sphere. However as we noted earlier, the tool can be used to infer the dimensionality of larger inclusions. Take for instance the large purple region just beyond $|x| = 20$ mm in Figure 4.29(b). A macroscopic sphere launched in the region will be drawn into a shape with one dominating dimension just as the metric predicts for the infinitesimal sphere. It is important to recognize, however, that the metric provides insight into the shape that initially spherical (or cubic) volumes of fluid will assume as the flow evolves. Given the cylindrical symmetry of the plume, the large purple region under consideration comprises a toroid in 3D when the cross-sectional view of Figure 4.29(b) is revolved about the plume centerline ($x = 0$). The metric is not suggesting that this entire toroidal structure is turned into a single linear filament. Instead, the metric indicates that a spherical inclusion located somewhere within the toroid will become a 1D structure as the flow progresses. The deformation of four

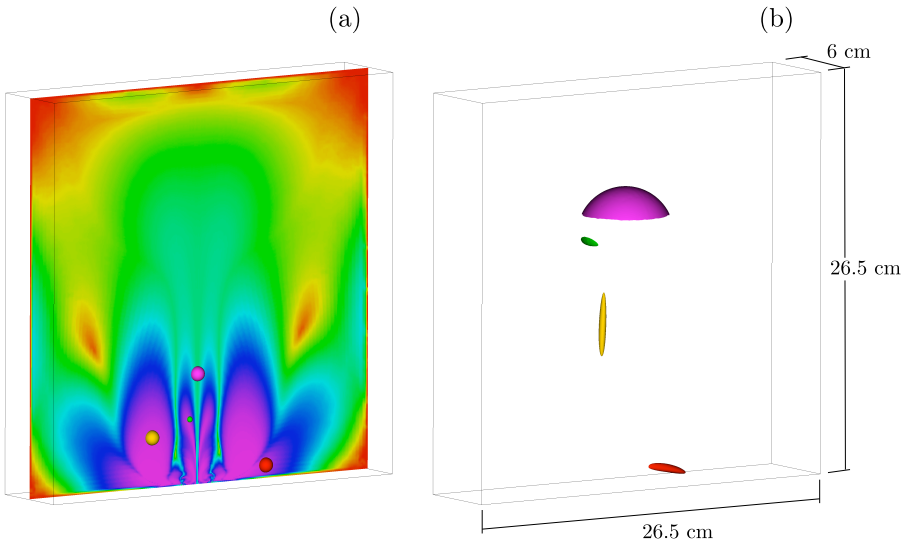

Figure 4.30: Deformation induced by the flow of case R6 for four macroscopic, initially spherical inclusions. (a) Location of the spherical fluid parcels at $t = 0$. The shape metric pseudocolor plot is provided for reference. (b) The deformed state of the identically colored parcels at $t = 2000$ s.

macroscopic, but nonetheless spherical inclusions, is illustrated in Figure 4.30. In each case, the large sphere is seen to transform just as the metric predicts.

The salient features visible for the numerical model in Figure 4.29(b) are also clearly captured for case N6. In particular are the regions where 1D structures are produced by the flow. Notice that the purple zones in Figure 4.29 form several, somewhat distinct pockets of material with the clearest separation between pockets being a vertical line situated at $|x| \approx 20$ mm. Tracking the evolution of material in the pockets from $t = 0$ to $t = 2000$ s proves to be quite interesting, particularly when also considering the orientation of the dominant dimension of the deformed mass. Figure 4.31 provides three images showing the transformation of various pockets of material extracted from Figure 4.29(b).

Notice that except for the orange tracers on the plume centerline in Figure 4.31(b), the material initially located such that $|x| < 20$ mm has come into plume head

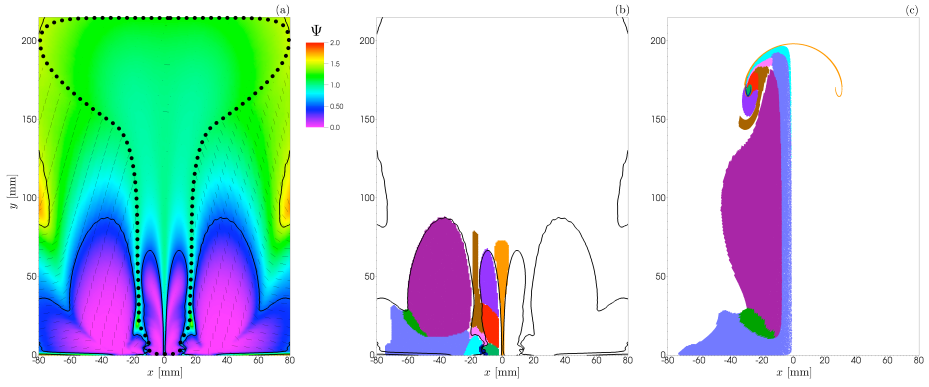

Figure 4.31: Orientation of maximum stretch and evolution of material pockets for case R6. (a) Stretch metric with eventual orientation of maximum principal stretch shown in the position the fluid elements have at the time of heater activation ($t = 0$ s). The maximum principal stretch axis orientation is illustrated using black line segments. Fluid enclosed by the the dotted black line has a maximum stretch orientation perpendicular to the cross-section shown (hence the line segments are invisible). Two contours for Ψ =0 .5, 1.5 are shown as solid black lines. (b) Blocks of passive tracers at $t = 0$ colored to illustrate various pockets of fluid in (a) where fluid in each pocket deforms similarly. (c) Position of the tracers in (b) at $t = 2000$ s.

shown in Figure 4.31(c) from above. That this is so can be seen from the evolution of the previously noted vertical dividing material line positioned at $|x| \approx 20$ mm (colored brown in Figures 4.31(b, c)). Material initially positioned inside this brown vertical line (*i.e.*, closer to the plume centerline) is brought into the plume head very early during the plume's evolution and is seen in Figure 4.31(c) to have collected in the developing scrolls situated at the bottom of the plume's leading edge LCS (orange). Because this fluid spends a limited amount of time interacting with the leading edge LCS before being deposited in the head scrolls, it is not drawn into sheet-like structures by the LCS, but is instead stretched into a toroid which constitutes the mass of the nascent scroll. The direction of maximum stretch for this fluid is shown to point normal to the plane of Figure 4.31(a), which is precisely the behavior expected for a toroid with an expanding major diameter. An example of the deformation a spherical inclusion located in this region would undergo is illustrated by the green ball in Figure 4.30.

Fluid initially located such that $|x| > 20$ mm is seen at $t = 2000$ s in Figure 4.31(c) to primarily comprise the conduit connecting the plume head to the heat source. Given that the vertical dimension of the conduit exceeds the diameter, one would reasonably expect the direction of maximal stretch to lie in the plane of cross-section as depicted in Figure 4.31(a).

Overall, the shape metric indicates that spherical fluid elements comprising the vast majority of mass below the plume leading edge LCS, whether part of the plume head or the trailing conduit, is transformed by the flow into essentially 1D ellipsoids. This observation is in agreement with the work of Farnetani and Hofmann [15]. In contrast, the transformation of spherical inclusions to sheet-like structures is limited to those fluid elements located above an ascending starting plume. Once the starting plume has reached the surface and enters a conduit-dominated mass transport regime, the production of 2D geometries from initially spherical heterogeneities is limited.

4.5 Conclusions

Laminar plumes show a surprising degree of complexity in the manner by which mass is transported and stirred, yet these flow features remain simple enough that fundamental processes can be readily investigated. Our tools of choice in the present study have been Lagrangian coherent structures (LCS) and stretching. As discussed in Section 4.3, LCS and underlying material surfaces furnish a practical means of characterizing the location and extent of a starting plume. These structures also organize mass transport within a given flow and hence provide valuable insight into how plumes interact with the ambient.

In particular, the leading edge LCS extracted from the backward-time FTLE field separated upwelling from ambient fluid. The structure was shown to attract nearby fluid elements over most of its length. And as the attracted elements interacted with the LCS during a plume's ascent, they were observed to stretch out along the structure. Similar observations have been made for plumes using numerical models accommodating much more Earth-like conditions [17, 45]. We found the leading edge LCS to be intimately related to shadowgraphs and other flow visualization techniques. In terms of determining the rise height of starting plumes, this particular LCS provided the most utility.

But it was the LCS extracted from the forward-time FTLE field that were found to furnish the most insight into permissible avenues for entrainment of ambient mass. In particular, we observed that for a plume generated via injection of hot syrup, a certain forward-time LCS formed an effective barrier that curtailed the plume's ability to entrain mass radially located beyond a certain distance from the plume centerline. The protective character of this outermost LCS eventually ceased as the injection plume reached the upper surface. Nevertheless, its absence in plumes generated via a localized heat source enabled such plumes to more efficiently incorporate radially distant mass.

Other differences were found between the studied injection plume and one produced using a local heater. The injection plume's outermost LCS and an LCS surrounding injected material were observed to form a temporary reservoir of mass shed by the plume head shortly following the start of injection. As the reservoir was depleted by entraining the mass into the plume head, the outermost LCS became coincident with the LCS surrounding injected mass.

Furthermore, by comparing the vertical origin of mass within the plume head, a strong link was observed between head vorticity and the efficiency by which overlying mass was entrained. The injection plume's higher vorticity head was composed primarily of mass originally located more than 100 mm off the tank bottom, while the exact opposite was observed for the localized heat source plume which had much lower head vorticity. The injection plume's elevated head vorticity also permitted substantially increased stretching of mass as the entrained material wrapped around toroidal scrolls.

As has been observed by other investigators, thermal plumes generated using a localized heat source were found to rise at an approximately constant speed following an initial transient period. In addition, the shape of the leading edge LCS for these plumes was well-described by an ellipsoid for most of the plume's ascent. The growth rate in the axes of the ellipsoid was observed to be constant and proportional to the rise velocity for a period of time following the initial transient interval.

A metric describing the generic dimensionality of deformed spherical inclusions was also developed. When applied to thermal plumes generated via a localized heat source, we found that the production of sheet-like structures was predominantly limited to spherical volumes of fluid initially located above the starting plume. However, some fluid above the heat source interacted with the plume shortly after liftoff and was quickly drawn into the head without being stretched into a sheet by the leading edge LCS. This initial material was shown to constitute the developing scrolls within

the head, and was composed of 1D structures oriented such that the direction of maximum stretching was tangent to the azimuthal axis of the cylindrical coordinate system. The conduit and bulk of the starting plume head were also observed to produce mainly 1D structures, however the maximum stretch axis of this material was perpendicular to that which formed the scroll core. One additional region producing sheet-like structures was observed to differentiate the mass which would eventually constitute the conduit from that which would be entrained into the head from above.

Given the simplistic nature of our laminar plumes when compared to those of more Earth-like conditions [12, 19, 41, 42, 44, 56], one clearly has to be careful when drawing direct geophysical comparisons. Nevertheless, several of the above observations have ramifications for mantle geodynamics. The Lagrangian coherent structures we have observed in our laboratory plumes are generic in the sense that similar structures exist in more complex flows, although the quantity and shape of the LCS may be quite different from one flow to the next. As mentioned above, ridges in the FTLE field have been used to investigate zones of high stretching in more Earth-like plumes [17, 45]. As with our work, these other studies find that the leading edge LCS and plume centerline have potentially high destructive capability in terms of homogenizing mantle heterogeneities. However, the cited works also show that as the leading edge LCS begins to deform under more complex flow scenarios (*e.g.*, viscosity variations at the 670 km discontinuity), the structure can become a source for producing long tendril-like heterogeneities that are shed by the plume as it upwells.

Although similar structures are observed in bio-inspired flows [46], the precise conditions necessary to produce a forward-time LCS akin to the outermost LCS of the injection plume (ref. Section 4.3.4) are not fully understood. Nevertheless, should an operating regime exist which generates analogous structures for mantle plumes, these forward-time LCS would likely be very effective at shielding the starting plume

from lateral entrainment of mass. As noted in Section 4.3.4 for the injection plume considered, the shielding effect of the outermost LCS degrades as the starting plume head approaches the upper surface. Therefore, even if a strong forward-time LCS barrier is produced for a starting mantle plume, the structure likely has no impact on the mass transport characteristics of a mature conduit. Forward-time LCS may, however, be critical to the transport behavior of isolated thermals throughout their lifetimes.

Should flood basalt provinces be produced by plume heads [55, 74] having similar characteristics to the thermal plumes studied here, the analysis of Section 4.3.4 suggests the composition would be dominated by material originating from the lowermost 600 km of the mantle. As the vigor of the plume increases, the plume head will become more efficient at incorporating overlying mass, but the head should still be composed primarily of mass originating near the core-mantle boundary. On the other hand, if mantle plumes operate in a regime similar to the injection plume which had a high vorticity head, then flood basalts would be expected to have a very pronounced component derived from the upper mantle. For the injection plume considered, $\sim 40\%$ of the total plume head mass would originate from a depth of less than 1300 km.

The shape metric developed in Section 4.4 is completely generic and certainly applicable to mantle plumes. The specific arrangement of shape producing regions observed for our laboratory plumes will likely differ from those simulated using more Earth-like conditions. Nevertheless, the complexity captured in Figure 4.31(a) was unexpected and suggests that even simple flows transform the dimensionality of fluid elements in an intricate manner. In comparison to the plume head, the conduit of an axisymmetric plume, like the ones studied here, is unremarkable in that spheres are transformed to 1D structures with little variation across the conduit [15]. However, such simplicity may not be representative of mantle plumes. Even a mature mantle plume which lost the plume head long ago must still operate in an environment

characterized by time-dependent flow, and that time dependence will undoubtedly alter how fluid elements are deformed in the conduit.

The shape metric itself provides the ability to investigate the dimensional transformations of an entire flow without relying on a small number of discrete spheres. As discussed in relation to Figure 4.31(b), the vertical line at $|x| \approx 20$ mm which separates two 1D-producing areas of the flow (shown seeded with brown tracers) is actually differentiating mass that will be brought into the plume head from above versus below. The presence of that particular transition in deformation behavior would have been very difficult to detect by launching a small number of spheres. Indeed, many of the boundaries or minor variations visible in Figure 4.31(a) may be overlooked by such techniques. The metric, on the other hand, provides a predictive map of the entire flow that permits a deeper analysis of how shapes are transformed. Even the Lagrangian coherent structures we have discussed do not completely foretell how the flow deforms an arbitrary element.

4.6 References

[1] W. Abouchami, A. W. Hofmann, S. J. G. Galer, F. A. Frey, J. Eisele, and M. Feigenson. Lead isotopes reveal bilateral asymmetry and vertical continuity in the Hawaiian mantle plume. *Nature*, 434(7035):851–856, 2005.

[2] C. J. Allègre, G. Manhès, and C. Göpel. The age of the Earth. *Geochimica et Cosmochimica Acta*, 59(8):1445–1456, 1995.

[3] K. T. Alligood, T. D. Sauer, and J. A. Yorke. *Chaos: An Introduction to Dynamical Systems*. Springer, 1996.

[4] A. Ansari and S. Morris. The effects of a strongly temperature-dependent viscosity on Stokes's drag law: experiments and theory. *Journal of Fluid Mechanics*, 159:459–476, 1985.

[5] Applied Modelling and Computation Group. *Fluidity Manual*. Department of Earth Science and Engineering, Imperial College London, 2010.

[6] G. K. Batchelor. Heat convection and buoyancy effects in fluids. *Quarterly Journal of the Royal Meteorological Society*, 80(345):339–358, 1954.

[7] D. Beigie, A. Leonard, and S. Wiggins. Invariant manifold templates for chaotic advection. *Chaos Solitons and Fractals*, 4(6):749–868, 1994.

[8] M. Branicki and S. Wiggins. Finite-time Lagrangian transport analysis: stable and unstable manifolds of hyperbolic trajectories and finite-time Lyapunov exponents. *Nonlinear Processes in Geophysics*, 17(1):1–36, 2010.

[9] H. P. Bunge, M. A. Richards, C. Lithgow-Bertelloni, J. R. Baumgardner, S. P. Grand, and B. A. Romanowicz. Time scales and heterogeneous structure in geodynamic Earth models. *Science*, 280(5360):91–95, 1998.

[10] J. R. Christman. *Fundamentals of Solid State Physics*. John Wiley and Sons, 1988.

[11] D. L. Coulliette and D. E. Loper. Experimental, numerical and analytical models of mantle starting plumes. *Physics of the Earth and Planetary Interiors*, 92(3-4):143–167, 1995.

[12] A. Davaille, M. Le Bars, and C. Carbonne. Thermal convection in a heterogeneous mantle. *Comptes Rendus Geoscience*, 335:141–156, 2003.

[13] A. Davaille, A. Limare, F. Touitou, I. Kumagai, and J. Vatteville. Anatomy of a laminar starting thermal plume at high Prandtl number. *Experiments in Fluids*, pages 1–16, 2010.

[14] A. Davaille and J. Vatteville. On the transient nature of mantle plumes. *Geophysical Research Letters*, 32(14), 2005.

[15] C. G. Farnetani and A. W. Hofmann. Dynamics and internal structure of a lower mantle plume conduit. *Earth and Planetary Science Letters*, 282(1-4):314–322, 2009.

[16] C. G. Farnetani and A. W. Hofmann. Dynamics and internal structure of the Hawaiian plume. *Earth and Planetary Science Letters*, 295(1-2):231–240, 2010.

[17] C. G. Farnetani, B. Legras, and P. J. Tackley. Mixing and deformations in mantle plumes. *Earth and Planetary Science Letters*, 196:1–15, 2002.

[18] C. G. Farnetani and H. Samuel. Lagrangian structures and stirring in the Earth's mantle. *Earth and Planetary Science Letters*, 206(3-4):335–348, 2003.

[19] C. G. Farnetani and H. Samuel. Beyond the thermal plume paradigm. *Geophysical Research Letters*, 32(7), 2005.

[20] S. Ferrachat and Y. Ricard. Regular vs. chaotic mantle mixing. *Earth and Planetary Science Letters*, 155(1-2):75–86, 1998.

[21] S. Ferrachat and Y. Ricard. Mixing properties in the Earth's mantle: Effects of the viscosity stratification and of oceanic crust segregation. *Geochemistry, Geophysics, Geosystems*, 2:2000GC000092, 2001.

[22] J. H. Ferziger. *Numerical Methods for Engineering Application*. John Wiley and Sons, 2nd edition, 1998.

[23] Y. Fukao, S. Widiyantoro, and M. Obayashi. Stagnant slabs in the upper and lower mantle transition region. *Reviews of Geophysics*, 39(3):291–323, 2001.

[24] R. J. Goldstein. Optical systems for flow measurement: Shadowgraph, schlieren, and interferometric techniques. In R. J. Goldstein, editor, *Fluid Mechanics Measurements*, pages 377–422. Hemisphere, 1983.

[25] R. Gomes, H. F. Levison, K. Tsiganis, and A. Morbidelli. Origin of the cataclysmic Late Heavy Bombardment period of the terrestrial planets. *Nature*, 436:466–469, 2005.

[26] S. P. Grand. Mantle shear structure beneath the Americas and surrounding oceans. *Journal of Geophysical Research*, 99(B6):11591–11621, 1994.

[27] P. Grassberger and I. Procaccia. Measuring the strangeness of strange attractors. *Physica D*, 9(1-2):189–208, 1983.

[28] M. A. Green, C. W. Rowley, and G. Haller. Detection of Lagrangian coherent structures in three-dimensional turbulence. *Journal of Fluid Mechanics*, 572:111–120, 2007.

[29] M. A. Green, C. W. Rowley, and A. J. Smits. Using hyperbolic Lagrangian coherent structures to investigate vortices in bioinspired fluid flows. *Chaos*, 20:017510, 2010.

[30] R. W. Griffiths and I. H. Campbell. Stirring and structure in mantle starting plumes. *Earth and Planetary Science Letters*, 99:66–78, 1990.

[31] G. Haller. Lagrangian coherent structures from approximate velocity data. *Physics of Fluids*, 14(6):1851–1861, 2002.

[32] J. Happel and E. Bart. The settling of a sphere along the axis of a long square duct at low Reynolds number. *Applied Scientific Research*, 29:241–258, 1974.

[33] S. R. Hart, E. H. Hauri, L. A. Oschmann, and J. A. Whitehead. Mantle plumes and entrainment: Isotopic evidence. *Science*, 256(5056):517–520, 1992.

[34] M. Hirsch, S. Smale, and R. Devaney. *Differential Equations, Dynamical Systems, and an Introduction to Chaos*. Academic Press, 2nd edition, 2003.

[35] A. W. Hofmann. Mantle geochemistry: The message from oceanic volcanism. *Nature*, 385(6613):219–229, 1997.

[36] K. Ide, D. Small, and S. Wiggins. Distinguished hyperbolic trajectories in time-dependent fluid flows: analytical and computational approach for velocity fields defined as data sets. *Nonlinear Processes in Geophysics*, 9(3-4):237–263, 2002.

[37] A. Jameson, W. Schmidt, and E. Turkel. Numerical solutions of the Euler equations by finite volume methods using Runge-Kutta time-stepping schemes. In *AIAA 14th Fluid and Plasma Dynamic Conference*, 1981.

[38] E. Kaminski and C. Jaupart. Laminar starting plumes in high-Prandtl-number fluids. *Journal of Fluid Mechanics*, 478:287–298, 2003.

[39] L. H. Kellogg and S. D. King. The effect of temperature dependent viscosity on the structure of new plumes in the mantle: Results of a finite element model in a spherical, axisymmetric shell. *Earth and Planetary Science Letters*, 148:13–26, 1997.

[40] L. H. Kellogg and D. L. Turcotte. Mixing and the distribution of heterogeneities in a chaotically convecting mantle. *Journal of Geophysical Research - Solid Earth*, 95(B1):421–432, 1990.

[41] R. C. Kerr and C. Mériaux. Structure and dynamics of sheared mantle plumes. *Geochemistry, Geophysics, Geosystems*, 5, 2004.

[42] I. Kumagai, A. Davaille, and K. Kurita. On the fate of thermally buoyant mantle plumes at density interfaces. *Earth and Planetary Science Letters*, 254:180–193, 2007.

[43] W. M. Lai, D. Rubin, and E. Krempl. *Introduction to Continuum Mechanics*. Butterworth-Heinemann, 1993.

[44] M. Le Bars and A. Davaille. Whole layer convection in a heterogeneous planetary mantle. *Journal of Geophysical Research*, 109(B3), 2004.

[45] S. C. Lin and P. E. van Keken. Deformation, stirring and material transport in thermochemical plumes. *Geophysical Research Letters*, 33(20):L20306, 2006.

[46] D. Lipinski and K. Mohseni. A ridge tracking algorithm and error estimate for efficient computation of lagrangian coherent structures. *Chaos*, (20):017504, 2010.

[47] J. E. Lupton. Terrestrial inert gases: Isotope tracer studies and clues to primordial components in the mantle. *Annual Review of Earth and Planetary Sciences*, 11:371–414, 1983.

[48] M. Mathur, G. Haller, T. Peacock, J. E. Ruppert-Felsot, and H. L. Swinney. Uncovering the lagrangian skeleton of turbulence. *Physical Review Letters*, 98(14):144502, 2007.

[49] H. J. Melosh. A new model Moon. *Nature*, 412:694–695, 2001.

[50] R. Montelli, G. Nolet, F. A. Dahlen, and G. Masters. A catalogue of deep mantle plumes: New results from finite-frequency tomography. *Geochemistry, Geophysics, Geosystems*, 7, 2006.

[51] R. Montelli, G. Nolet, F. A. Dahlen, G. Masters, E. R. Engdahl, and S. H. Hung. Finite-frequency tomography reveals a variety of plumes in the mantle. *Science*, 303:338–343, 2004.

[52] S. Morris. The effects of a strongly temperature-dependent viscosity on slow flow past a hot sphere. *Journal of Fluid Mechanics*, 124:1–26, 1982.

[53] E. Moses, G. Zocchi, and A. Libchaber. An experimental study of laminar plumes. *Journal of Fluid Mechanics*, 251:581–601, 1993.

[54] C. O'Farrell and J. O. Dabiri. A lagrangian approach to identifying vortex pinch-off. *Chaos*, 20:017513, 2010.

[55] M. A. Richards, R. A. Duncan, and V. Courtillot. Flood basalts and hot-spot tracks: Plume heads and tails. *Science*, 246(4926):103–107, 1989.

[56] M. A. Richards and R. W. Griffiths. Thermal entrainment by deflected mantle plumes. *Nature*, 342(6252):900–902, 1989.

[57] J. Schmalzl and U. Hansen. Mixing the earths mantle by thermal convection: A scale dependent phenomenon. *Geophysical Research Letters*, 21(11):987–990, 1994.

[58] J. Schneider, J. Schmalzl, and T. Tel. Lagrangian avenues of transport in the Earth's mantle. *Chaos*, 17(3):033115, 2007.

[59] S. C. Shadden, F. Lekien, and J. E. Marsden. Definition and properties of Lagrangian coherent structures from finite-time Lyapunov exponents in two-dimensional aperiodic flows. *Physica D*, 212(3-4):271–304, 2005.

[60] K. Shariff, A. Leonard, and J. H. Ferziger. Dynamical systems analysis of fluid transport in time-periodic vortex ring flows. *Physics of Fluids*, 18(4):047104, 2006.

[61] D. J. Shlien. Some laminar thermal and plume experiments. *Physics of Fluids*, 19(8):1089–1098, 1976.

[62] G. Strang. *Introduction to Linear Algebra*. Wellesley-Cambridge Press, 1993.

[63] N. Subramanian, L. H. Kellogg, and D. L. Turcotte. Statistics of advective stretching in three-dimensional incompressible flows. *Journal of Statistical Physics*, 136(5):926–944, 2009.

[64] P. J. Tackley. Mantle convection and plate tectonics: toward an integrated physical and chemical theory. *Science*, 288:2002–2007, 2000.

[65] P. J. Tackley, D. J. Stevenson, G. A. Glatzmaier, and G. Schubert. Effects of an endothermic phase transition at 670 km depth in a spherical model of convection in the Earth's mantle. *Nature*, 361(6414):699–704, 1993.

[66] P. J. Tackley, D. J. Stevenson, G. A. Glatzmaier, and G. Schubert. Effects of multiple phase transitions in a three-dimensional spherical model of convection in Earth's mantle. *Journal of Geophysical Research*, 99(B8):15877–15901, 1994.

[67] W. Tang, M. Mathur, G. Haller, D. C. Hahn, and F. H. Ruggiero. Lagrangian coherent structures near a subtropical jet stream. *Journal of the Atmospheric Sciences*, 67:2307–2319, 2010.

[68] J. C. Tannehill, D. A. Anderson, and R. H. Pletcher. *Computational Fluid Mechanics and Heat Transfer*. Taylor and Francis, 2nd edition, 1997.

[69] J. R. Taylor. *An Introduction to Error Analysis: The Study of Uncertainties in Physical Measurements*. University Science Books, 2nd edition, 1997.

[70] R. D. van der Hilst, S. Widiyantoro, and E. R. Engdahl. Evidence for deep mantle circulation from global tomography. *Nature*, 386:578–584, 1997.

[71] P. van Keken. Evolution of starting mantle plumes: A comparison between numerical and laboratory models. *Earth and Planetary Science Letters*, 148:1–11, 1997.

[72] P. E. van Keken and C. J. Ballentine. Dynamical models of mantle volatile evolution and the role of phase transitions and temperature-dependent rheology. *Journal of Geophysical Research - Solid Earth*, 104(B4):7137–7151, 1999.

[73] J. Vatteville, P. E. van Keken, A. Limare, and A. Davaille. Starting laminar plumes: comparison of laboratory and numerical modeling. *Geochemistry Geophysics Geosystems*, 10(12):1–9, 2009.

[74] R. S. White and D. McKenzie. Mantle plumes and flood basalts. *Journal of Geophysical Research*, 100(B9):17543–17585, 1995.

[75] S. Widiyantoro, B. L. N. Kennett, and R. D. van der Hilst. Seismic tomography with P and S data reveals lateral variations in the rigidity of deep slabs. *Earth and Planetary Science Letters*, 173:91–100, 1999.

[76] S. Wiggins. *Introduction to Applied Nonlinear Dynamical Systems and Chaos*. Springer, 2nd edition, 2000.

[77] M. G. Worster. The axisymmetric laminar plume: asymptotic solution for large Prandl number. *Studies in Applied Mathematics*, 75:139–152, 1986.

[78] H. D. Xi, S. Lam, and K. Q. Xia. From laminar plumes to organized flows: the onset of large-scale circulation in turbulent thermal convection. *Journal of Fluid Mechanics*, 503:47–56, 2004.

[79] S. J. Zhong, M. T. Zuber, L. Moresi, and M. Gurnis. Role of temperature-dependent viscosity and surface plates in spherical shell models of mantle convection. *Journal of Geophysical Research - Solid Earth*, 105(B5):11063–11082, 2000.

[80] A. Zindler and S. Hart. Chemical geodynamics. *Annual Review of Earth and Planetary Sciences*, 14:493–571, 1986.

CHAPTER V

Time scale analysis for onset of convection in laminar plumes

5.1 Introduction

Linear stability analyses and numerous experiments on Rayleigh-Bénard convection have shown that as a fluid layer is uniformly heated from below or cooled from above, the fluid will remain quiescent provided the Rayleigh number (ref. Table V).

$$Ra = \frac{\rho g \alpha \Delta T d^3}{\kappa \mu} \tag{5.1}$$

remains below some critical Rayleigh number value, Ra_c [3, 8, 9, 10, 14, 18]. Once Ra_c is exceeded, the system will transition from a purely conductive heat transfer regime to one in which convective motion of the fluid becomes progressively more important with increasing Rayleigh number. The exact Rayleigh number value corresponding to the onset of convection depends on boundary conditions (*e.g.,* whether the upper and lower surfaces bounding the convecting layer are free-slip or no-slip) and fluid properties (*e.g.*, temperature dependent viscosity). Experiments with localized heat sources constructed from fine wires [17, 21, 1] and larger diameter cylinders [18] have suggested that Rayleigh-Bénard results are also directly applicable to the onset of convection in such cases. Here the fluid surrounding the heat source initially warms

Symbol	Description	Units
α	Expansion coefficient	$^\circ\mathrm{C}^{-1}$
δ	Thermal boundary layer thickness	m
$\kappa = k/\rho c_p$	Thermal diffusivity	$\mathrm{m}^2\,\mathrm{s}^{-1}$
μ	Dynamic viscosity	Pa s
$\overline{\mu} = \mu(T_c + \Delta T/2)$	Dynamic viscosity at $T_c + \Delta T/2$	Pa s
ρ	Density	$\mathrm{kg\,m}^{-3}$
$\bar{a}$	Time-averaged plume head diameter	m
c_p	Specific heat capacity	$\mathrm{J\,kg}^{-1}\,\mathrm{K}^{-1}$
d	Depth of fluid layer	m
g	Gravitational acceleration	$\mathrm{m\,s}^{-2}$
R	Heater radius	m
t	Time	s
t_0	Convection onset time scale from Moses *et al.* [16]	s
t_{0f}	Plume liftoff time scale	s
T	Temperature	$^\circ$C
T_c	Ambient temperature	$^\circ$C
T_f	Temperature 5 mm radially away from heater	$^\circ$C
T_h	Heater temperature	$^\circ$C
$\Delta T = T_h - T_c$	Maximum temperature contrast	$^\circ$C
u_0	Plume head velocity	$\mathrm{m\,s}^{-1}$
y_0	Plume head virtual origin	m
$c = \ln(\mu(T_c)/\mu(T_h))$	Viscous contrast	-
Ra	Rayleigh number	-
Ra_δ	Raleigh number based on thermal boundary layer thickness	-
Ra_c	Rayleigh critical	-

Table 5.1: Notation.

by thermal conduction until the incipient thermal boundary layer becomes unstable and erupts.

Unlike simply detecting the presence of convection, defining criteria for the precise time at which a system transitions from the conductive heat transfer regime to one dominated by convection is quite difficult. While the transition and onset of convection may be rapid, particularly for isoviscous fluids [5], it is nonetheless a continuous process. Consequently, one generally must define a threshold against which some characteristic flow parameter can be compared and define onset as the crossing

of this threshold. Examples of such criteria are a departure in the rate of change of fluid temperature from that of a purely conductive profile [5] or destruction of the concentric symmetry of isotherms within the thermal boundary layer surrounding a heated wire [17, 21].

In contrast to these techniques, Moses *et al.* [16] construct an alternative definition for the onset of convection that requires no arbitrary threshold and can be computed to an accuracy that is limited only by experimental uncertainty. The authors conduct a series of experiments on laminar, thermal plumes generated with small resistive heaters in essentially isoviscous fluids. The plumes are characterized by a bulbous head connected to the heat source via a thin trailing conduit. As have many others (ref. Chapter IV and [13, 16, 4, 6, 7, 15]), Moses *et al.* observe that after an initial transient period, the plume head reaches a constant velocity u_0. This velocity along with a virtual origin y_0 extracted from curves of plume leading edge position versus time is then used to construct the characteristic time $t_0 = y_0/u_0$ which is then taken to mark the onset of convection. The definition of onset using the time scale t_0 lends itself to experimental simplicity since one only needs to track the height of a plume head versus time which can easily be accomplished by a variety of techniques (ref. Chapter IV and [6, 16, 4]). While the time scale t_0 has some important virtues, it is not clear why t_0 should be a reliable marker for termination of the purely conductive regime.

The objective of the following development is to explore the relationship between the time scale t_0 and the onset of convection for laminar plumes generated in a fluid with temperature dependent viscosity. Our experimental results indicate that t_0 is indeed a proxy for the end of the purely conductive regime, but the time scale can be corrupted by factors affecting the advection-dominated phase. The remainder of the presentation is structured as follows. In Section 5.2, a brief overview of the experimental setup is presented followed by an analysis of the results in Section 5.3.

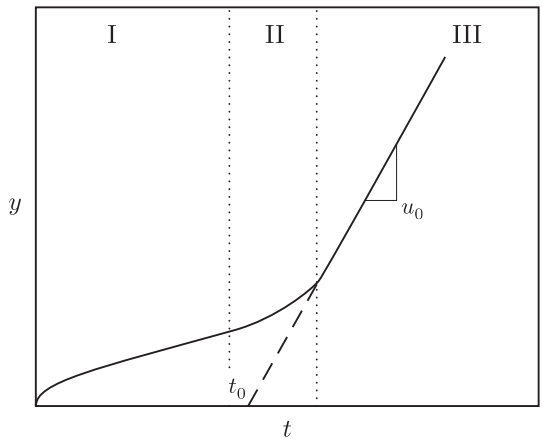

Figure 5.1: Schematic of the time scale t_0 for onset of convection. Thermal boundary layer (solid line) grows by conduction in Phase I then becomes unstable in Phase II. The resulting plume head reaches a steady rise velocity in Phase III.

And finally, some concluding remarks are presented in Section 5.4.

5.2 Experimental setup

A full description of our experimental setup can be found in Chapter 2. Briefly, laminar plumes are generated in an acrylic, cubic tank of dimension 26.5 cm per side. The tank containing the working fluid is sealed and surrounded by a water bath to provide a well-controlled initial temperature of $25.2 \pm 0.1\,^{\circ}\mathrm{C}$. The heat source is a 2 cm diameter heater located in the center of the tank bottom. Plumes are created under two operating regimes with the heater operating at constant power or constant temperature. In the constant power cases, the heater power is fixed and its temperature is found to increase slowly over time as dictated by the flow dynamics. Actual power delivered to the fluid in the constant power cases, monitored with a thin-film heat flux gauge (Omega HFS-3) cemented to the heater, is always less than the total heater power because of parasitic losses to the tank structure. For the constant temperature cases, the heater power is digitally controlled and allowed to fluctuate such that the heater temperature ramps up to the desired steady state

Property	Value or formulation	Units
Density at 25 °C (ρ)	1441	kg m^{-3}
Thermal expansion coefficient (α)	3.1×10^{-4}	K^{-1}
Dynamic viscosity (μ)	$\mu = 1080e^{-0.156T+6.25\times10^{-4}T^2}$	Pa s
Specific heat capacity (c_p)	2280	J kg^{-1} °C^{-1}
Thermal conductivity (k)	0.34	W m^{-1} °C^{-1}

Table 5.2: Corn syrup fluid properties. The thermal expansion coefficient and temperature dependence of viscosity were measured in the laboratory. Specific heat capacity and thermal conductivity values were provided by the manufacturer (LSI Specialty Products).

surface temperature in 90 s or less.[1] Once the constant temperature set point is reached, the temperature is maintained to ±0.1 °C.

In all experiments, Liquidose 436 corn syrup is utilized. The syrup is seeded with two types of neutrally buoyant passive tracers – a white powdered plastic and thermochromic liquid crystals that preferentially scatter light of a particular wavelength based on the temperature of the liquid crystals. The encapsulated liquid crystals utilized, Hallcrest NSL33R25C15W100, are active in the visible spectrum for temperatures spanning $25 \lesssim T \lesssim 27\,^{\circ}$C. Properties of the syrup are provided in Table 5.2 and a summary of experimental operating conditions can be found in Table 5.3.

Following heater activation, the full 3D flow is imaged at discrete time intervals using the stereoscopic PIV (SPIV) system described in Chapter 2. The raw SPIV images captured during each experiment are then processed to extract the time-dependent velocity field and fluid temperature. At least 48 hours is allowed between runs for the syrup to re-equilibrate with the bath temperature.

5.3 Experimental results and analysis

Prior to discussing our experimental results, two important modifications to the Rayleigh number formulation provided in the Introduction must be made. First as

[1]The heat flux gauge was also utilized in these experiments, however the high heat flux during the initial temperature ramp up caused the flux sensor to fail.

	Heater		
Case	Power [W]	Flux power [W]	Temperature [°C]
N1	0.62	0.44	-
N2	0.96	0.72	-
N3	-	-	50
N4	-	-	60
N5	-	-	70
N6	-	-	80

Table 5.3: Experimental parameters. Flux power values represent the steady state power delivered directly to the syrup as measured with a heat flux gauge. These values are lower than the total heater power due to parasitic heat losses to the acrylic tank.

noted in the Introduction, a thermal boundary layer develops over the heat source following activation of the heater and grows by conduction until the buoyancy generated is sufficient for the layer to become unstable. During this purely conductive heat transfer phase, the depth of the fluid d has little impact, and the thickness of the boundary layer is the pertinent length scale in Eq. 5.1 [1, 17, 18, 21]. The modified Rayleigh number is then

$$Ra_\delta = \frac{\rho g \alpha \Delta T \delta^3}{\kappa \mu}, \tag{5.2}$$

and we will take the value of Ra_δ at the onset of convection as the critical Rayleigh number Ra_c.

Second our corn syrup has a temperature dependent viscosity, and hence we must also choose a characteristic value of μ for Eq. 5.2. Here we follow Stengel *et al.* [20] and White [22] and set $\mu = \overline{\mu}$, the viscosity corresponding to the mean temperature anomaly $\Delta T/2$. The referenced authors found that for Rayleigh-Bénard convection in fluids with exponential or super-exponential dependence of viscosity on temperature, Ra_c based on $\overline{\mu}$ initially increases with the viscosity contrast $c = \ln(\mu(T_c)/\mu(T_h))$ before plateauing at $c \approx 8$ and then decreasing for $c \gtrsim 8$.

Once the plume has developed, hot buoyant material constituting the plume head eventually comes in contact with the cold overlying ambient. Separating upwelling

and ambient material of the starting plume is a material surface at the plume leading edge which strongly attracts nearby fluid elements. As discussed in Chapter IV, the material surface is a robust characteristic of laminar plumes and is intimately related to other means of identifying plume position (*e.g.*, shadowgraphs, schlierens, and the use of fluid dye). To determine the location of this material surface for our datasets, we compute the backward, finite-time Lyapunov exponent (FTLE) field from the velocity data using the technique of [19] (ref. Chapter IV). The FTLE field provides a measure of the average rate at which nearby fluid elements separate [2]. The strong attraction of fluid parcels to the leading edge material surface will be manifest as strong separation in backward time. Hence, the surface will produce a ridge of elevated values in the backward-time FTLE field. The FTLE ridge is known as a Lagrangian coherent structure (LCS) [19], and we take the apex of the leading-edge LCS as identifying the vertical position of the starting plume. The backward-time FTLE field and leading edge LCS are illustrated for one of our plumes in Figure 5.2).

A partial history of the plume height as a function of time for each of our six experimental cases is shown in Figure 5.3. At the earliest times following heater activation, the flow has not developed enough for fluid elements on either side of the unstable leading edge LCS to separate sufficiently. Therefore a well-defined peak in the backward time FTLE field cannot be extracted [11, 12], and the precise location of the plume's leading edge is unclear. Consequently the earliest head positions shown in Figure 5.3 are those for which the LCS could be unambiguously identified. Also not depicted in the figure is the location of the head once the head velocity starts decreasing as the plume approaches the top of the tank [13].

A least squares fit of the plume head position versus time during the constant head velocity regime provides the velocities and virtual origins summarized in Table 5.4. With u_0 and y_0 available, the characteristic time $t_0 = y_0/u_0$ [16] can be computed and used to construct an estimate of the thermal boundary layer thickness δ just

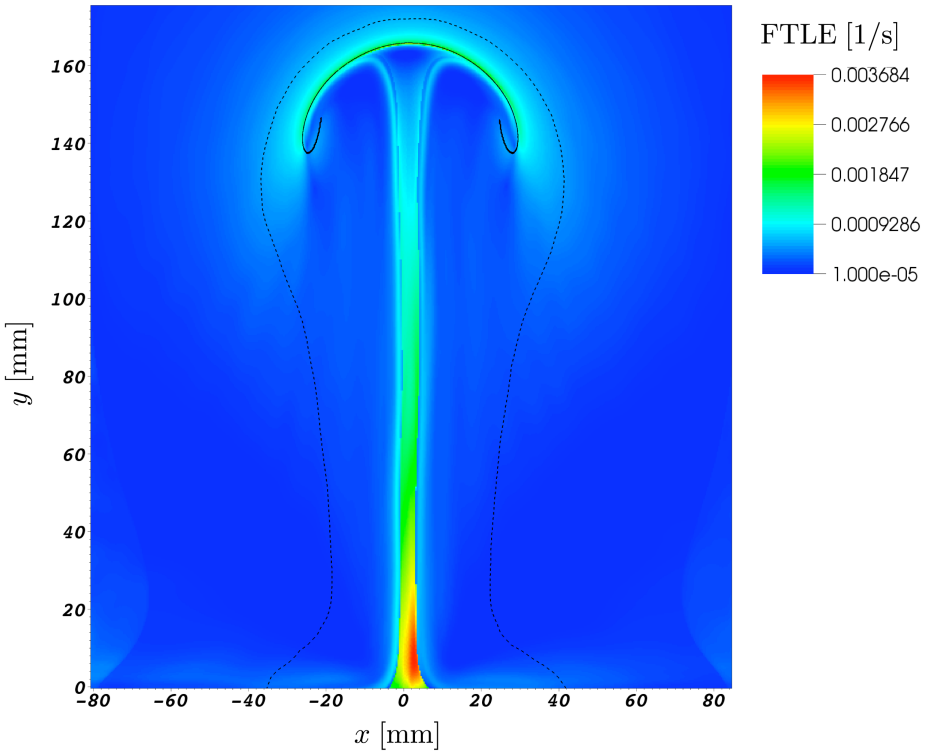

Figure 5.2: Head structure for a laminar plume generated with a constant heater power of 1.8 W. The view is a vertical cross section through the plume with the heater centered at the origin. Steady state heater temperature is 80 °C. The pseudocolor background is the backward-time FTLE field with larger values representing higher rates of separation between initially nearby fluid elements. The outer black contour (dashed) represents a temperature of 0.3 °C above ambient. The umbrella-shaped solid black line is the leading edge LCS.

Case	u_0 [mm/s]	y_0 [mm]	t_0 [s]	δ [mm]	ΔT [°C]	$\overline{\mu}$ [Pa-s]	c	Ra_c
N1	0.030	-48	1600	25	10	18	1.1	350
N2	0.042	-56	1350	23	15	14	1.5	500
N3	0.055	-31	560	15	25	7.5	2.7	490
N4	0.075	-27	360	12	35	4.5	3.6	600
N5	0.097	-26	270	10	45	2.7	4.3	800
N6	0.12	-24	200	9.0	55	1.7	4.9	1020

Table 5.4: Experimental results for the six cases of Table 5.3.

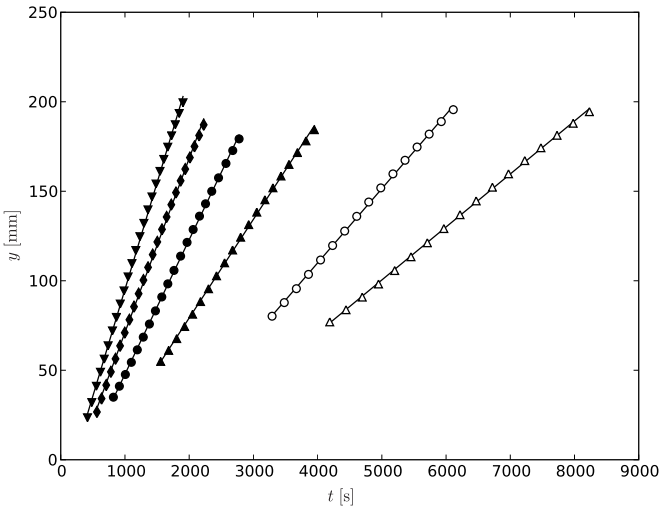

Figure 5.3: Plume head leading edge height above the tank bottom versus time for the six experimental cases. Best fit lines are shown in black for each case. (△) N1. (○) N2. (▲) N3. (●) N4. (⧫) N5. (▼) N6.

prior to the onset of convection. We will assume the thermal boundary layer atop the heater has a thickness of $\delta = 2\sqrt{\kappa t_0}$. Substituting δ, $\overline{\mu}$, and the remaining parameters into Eq. 5.2 yields the Rayleigh critical values shown in Table 5.4 and plotted as a function of viscosity contrast c in Figure 5.4.

Figure 5.4 captures quite well the qualitative nature of Ra_c dependence on c as reported by Stengel *et al.* [20] and White [22] for the onset of Rayleigh-Bénard convection. Also of note is the ratio of maximum to minimum Ra_c values in Table 5.4 which is $O(3)$. For roughly the same range of viscosity contrast, the ratio varies from 1.3 to 2.6 in the referenced works of Stengel *et al.* and White depending on the boundary conditions considered and the assumed temperature dependence of viscosity. Provided that onset of Rayleigh-Bénard convection is directly applicable to our localized heater in much the same way as it is for wires and cylinders [1, 17, 18, 21], then the observations from our data certainly do not exclude use of t_0 as a marker for onset.

We can obtain further insight into the relationship between t_0 and the onset of

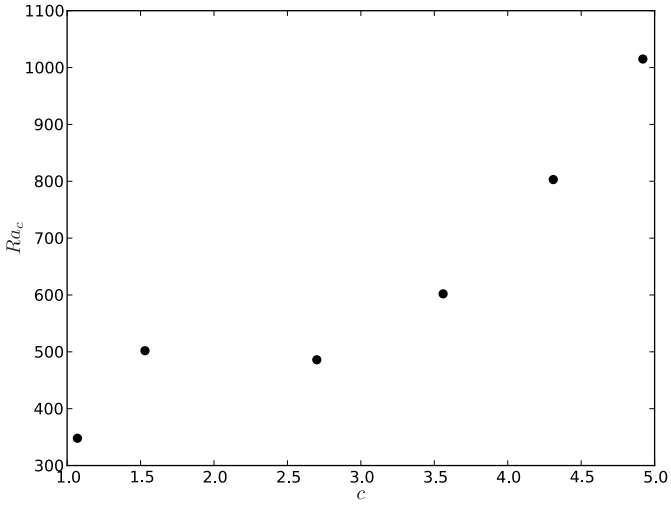

Figure 5.4: Ra_c versus viscosity contrast for the data of Table 5.4.

convection by inspecting time traces for a thermocouple located in close proximity to the heater. In all our experiments, the heat flux gauge was equipped with a thermocouple located roughly 5 mm radially beyond the periphery of the heater. Consequently, the thermocouple could detect changes in the thermal boundary layer temperature as the layer became unstable and colder fluid was subsequently drawn in. This effect was quite pronounced for the constant temperature cases N3-N6 as shown in Figure 5.5, but no discernable signal was visible in cases N1 or N2. The time t_{0f} corresponding to the peak temperature reached prior to the illustrated decrease provides another time scale related to the onset of convection. Although not presented here, it should be noted that in all four cases, maximum fluid velocity in the vicinity of the heater had reached 60-110% of the constant head velocities recorded in Table 5.4 by the time t_{0f} has elapsed. Consequently this new measure, t_{0f}, is more of a proxy for liftoff time than for the onset of convection. Nevertheless, a comparison of this time scale to that of Moses *et al.* is presented in Table 5.5 along with the time averaged radius of the plume head $\overline{a}$ during the constant head velocity regime.

There is, however, one particular issue with the interpretation of t_0 that is apparent. The constant power cases N1 and N2 from Table 5.4 present a low viscosity

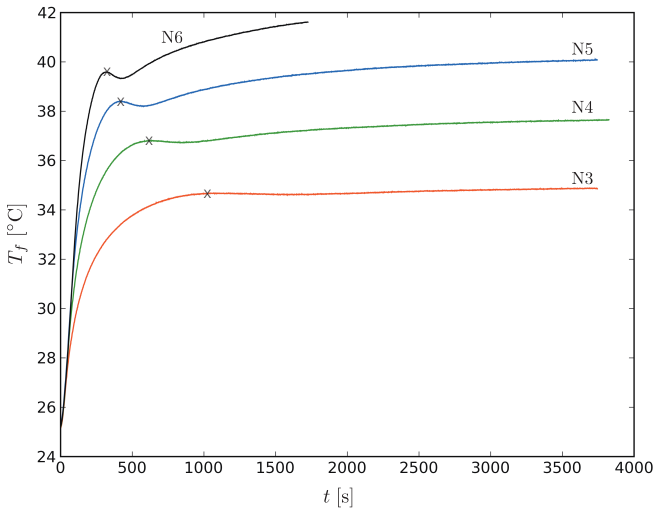

Figure 5.5: Fluid temperature 5 mm away from heater perimeter as a function of time. Curve labels correspond to case numbers. The time t_{0f} of peak temperature prior to plume liftoff is marked with an X.

contrast and are hence nearly isoviscous. Unfortunately, the Rayleigh critical values computed using t_0 for these two cases are significantly lower than the limiting critical values obtained from the stability analysis of Stengel *et al.* [20]. If the onset of convection in our isolated plumes is adequately modeled by Rayleigh-Bénard convection, then in the isoviscous limit Ra_c should land in between the two theoretical values of $Ra_c \approx 1100$ and $Ra_c \approx 1700$, with Ra_c being biased toward 1700 as the fluid directly over the thermal boundary layer better approximates a rigid lid. Note that if the boundary layer thickness is computed using t_{0f} instead of t_0, then as the viscosity contrast decreases Rayleigh critical values appear to approach those predicted by Rayleigh-Bénard theory (ref. Table 5.5).

Several sources could be responsible for the reduced Rayleigh critical magnitudes obtained with t_0, particularly in the low viscosity limit. It is conceivable that the time scale t_0 is systematically smaller than the actual time required for onset of convection, which would serve to uniformly lower the estimated Ra_c. Of course, as noted in the Introduction, measuring the onset of convection is to a large degree predicated on

Case	t_0 [s]	$\overline{a}$ [mm]	t_{0f} [s]	t_{0f}/t_0	$Ra_c(t_{0f})$
N3	560	51	1070	1.9	1300
N4	360	44	630	1.8	1400
N5	270	38	420	1.6	1600
N6	200	38	320	1.6	2050

Table 5.5: Comparison of liftoff time scale t_{0f} to t_0 for cases N3-N6. Time-averaged plume head diameters, $\overline{a}$, and Rayleigh critical values computed using t_{0f} are also included.

the definition one chooses to mark onset. Therefore a systematic under prediction of onset time is not a large concern and could easily be corrected with a simple scale factor. Our data cannot rule out the presence of a systematic bias.

An additional factor that may skew Ra_c results computed using t_0 derives directly from the construction of the time scale. Given that t_0 is determined from the plume head velocity, experimental conditions pertinent to the advection dominated phase could contaminate the extracted t_0 even though these factors have little or no influence on the growth and initial instability of the thermal boundary layer. Such effects could be significant for the slow N1 and N2 cases which produced plumes with large heads that likely rose at lower than expected velocities due to the presence of tank side walls. If we take the plume diameter as the maximum width of the leading edge LCS and time average over the constant velocity phase of plume ascent, we obtain an average diameter of ~ 65 mm in both these two cases. An estimate of the wall effects (ref. Chapter IV) suggests the constant velocity of the N1 and N2 plume heads may be 50% lower than would be observed in a wider tank.

One might envisage that an increasing u_0 will decrease t_0, however this is not necessarily the case. Consider the plot of thermal boundary layer thickness versus time shown in Figure 5.6. An order of magnitude estimate of the time required for a thermal perturbation at the center of the tank to reach the sidewalls is given by

$$\tau \sim d^2/4\kappa, \tag{5.3}$$

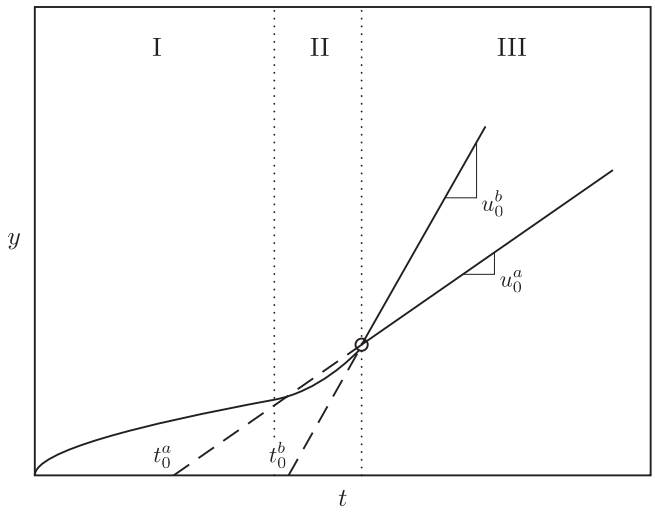

Figure 5.6: Effect of u_0 on the time scale t_0. Thermal boundary layer (solid line) grows by conduction in Phase I then becomes unstable in Phase II. The resulting plume head reaches a steady velocity in Phase III. Provided development of two plumes, a and b, are identical in Phases I and II, an increase in the head velocity for case b equates to an increase in t_0. The pivot is identified with an open circle.

where d is the tank width and κ is the thermal diffusivity. Based on our tank dimensions and syrup properties, $\tau \sim 48$ hours. Therefore, tank sidewalls have a negligible effect on the thermal boundary layer growth immediately following heater activation. The solid curve in Phase I of Figure 5.6 then depends on heater operating conditions and fluid properties alone. Once the flow has transitioned to the advection-dominated regime, an increase in plume head velocity will serve to steepen the curve in Phase III as though it were pivoting at some point in positive ty-space. The end result is that the time scale t_0 will increase with head velocity as illustrated in Figure 5.6. A careful examination of the data in Table 5.5 suggests such contamination of t_0 is indeed an issue. As the time-averaged plume head radius decreases, so too does the ratio t_{0f}/t_0. In other words, as the plume head diameter increases and the rise velocity slows due to wall effects, t_0 is seen to decrease.

5.4 Conclusions

Moses *et al.* [16] construct a time scale t_0 based on the constant velocity of a plume head and a virtual origin y_0 determined from a least squares fit of the plume head elevation versus time. The time scale was found to provide Rayleigh critical estimates for the onset of convection that captured the qualitative dependence of Ra_c on the viscosity contrast observed by Stengel *et al.* [20] and White [22] for Rayleigh-Bénard convection in fluids with temperature-dependent viscosity. However in the limit of small viscosity contrast, the Rayleigh critical values constructed from t_0 were significantly lower than those predicted from linear stability theory. Furthermore t_0 was found to be susceptible to contamination from conditions, namely the influence of tank side walls, that have little relevance to the initial conductive growth of the thermal boundary layer prior to liftoff. Overall, the time scale t_0 is not without merit, however caution is warranted when using the measure to confine the duration of the purely conductive heat transfer regime.

5.5 References

[1] D. Ambrosini, D. Paoletti, and G. S. Spagnolo. Study of free-convective onset on a horizontal wire using speckle pattern interferometry. *International Journal of Heat and Mass Transfer*, 46(22):4145–4155, 2003.

[2] M. Branicki and S. Wiggins. Finite-time Lagrangian transport analysis: stable and unstable manifolds of hyperbolic trajectories and finite-time Lyapunov exponents. *Nonlinear Processes in Geophysics*, 17(1):1–36, 2010.

[3] S. Chandrasekhar. *Hydrodynamic and Hydromagnetic Stability*. Dover, 1981.

[4] D. L. Coulliette and D. E. Loper. Experimental, numerical and analytical models of mantle starting plumes. *Physics of the Earth and Planetary Interiors*, 92(3-4):143–167, 1995.

[5] A. Davaille and C. Jaupart. Transient high-Rayleigh-number thermal convection with large viscosity variations. *Journal of Fluid Mechanics*, 253:141–166, 1993.

[6] A. Davaille, A. Limare, F. Touitou, I. Kumagai, and J. Vatteville. Anatomy of a laminar starting thermal plume at high Prandtl number. *Experiments in Fluids*, pages 1–16, 2010.

[7] A. Davaille and J. Vatteville. On the transient nature of mantle plumes. *Geophysical Research Letters*, 32(14), 2005.

[8] T. D. Foster. Onset of convection in a layer of fluid cooled from above. *Physics of Fluids*, 8(10):1770–1774, 1965.

[9] T. D. Foster. Effect of boundary conditions on onset of convection. *Physics of Fluids*, 11(6):1257–1262, 1968.

[10] R. J. Goldstein and R. J. Volino. Onset and development of natural convection above a suddenly heated horizontal surface. *Journal of Heat Transfer*, 117(4):808–821, 1995.

[11] M. A. Green, C. W. Rowley, and G. Haller. Detection of Lagrangian coherent structures in three-dimensional turbulence. *Journal of Fluid Mechanics*, 572:111–120, 2007.

[12] M. A. Green, C. W. Rowley, and A. J. Smits. Using hyperbolic Lagrangian coherent structures to investigate vortices in bioinspired fluid flows. *Chaos*, 20:017510, 2010.

[13] E. Kaminski and C. Jaupart. Laminar starting plumes in high-Prandtl-number fluids. *Journal of Fluid Mechanics*, 478:287–298, 2003.

[14] Y. Katto and T. Masuoka. Criterion for onset of convective flow in a fluid in a porous medium. *International Journal of Heat and Mass Transfer*, 10(3):297–309, 1967.

[15] R. C. Kerr and C. Mériaux. Structure and dynamics of sheared mantle plumes. *Geochemistry, Geophysics, Geosystems*, 5, 2004.

[16] E. Moses, G. Zocchi, and A. Libchaber. An experimental study of laminar plumes. *Journal of Fluid Mechanics*, 251:581–601, 1993.

[17] J. R. Parsons and J. C. Mulligan. Transient free convection from a suddenly heated horizontal wire. *Journal of Heat Transfer*, 100(3):423–428, 1978.

[18] J. R. Parsons and J. C. Mulligan. Onset of natural convection from a suddenly heated horizontal cylinder. *Journal of Heat Transfer*, 102(4):636–639, 1980.

[19] S. C. Shadden, F. Lekien, and J. E. Marsden. Definition and properties of Lagrangian coherent structures from finite-time Lyapunov exponents in two-dimensional aperiodic flows. *Physica D*, 212(3-4):271–304, 2005.

[20] K. C. Stengel, D. S. Oliver, and J. R. Booker. Onset of convection in a variable-viscosity fluid. *Journal of Fluid Mechanics*, 120(JUL):411–431, 1982.